A MODEL FOR BACKSCATTERING ANGULAR RESPONSE OF GASSY SEDIMENTS: APPLICATIONS TO PETROLEUM EXPLORATION AND DEVELOPMENT PROGRAMS

BY

LUCIANO EMIDIO NEVES DA FONSECA

B.Sc. Electrical Engineering, Universidade de Brasília, 1986

M.Sc. Electrical Engineering, Universidade Estadual de Campinas, 1990

DISSERTATION

Submitted to the University of New Hampshire

In Partial Fulfillment of

The Requirements for the Degree of

Doctor of Philosophy

In

Ocean Engineering

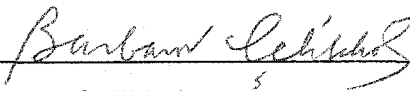December 2001

UMI Number: 3030603

UMI®

PH.D. DISSERTATION

This dissertation has been examined and approved.

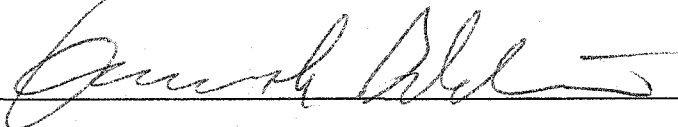Dissertation Director, Larry A. Mayer

Professor of Earth Sciences and Ocean Engineering

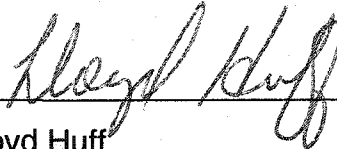Barbaros Celikkol

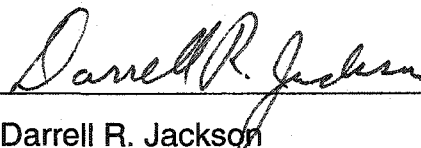Professor of Mechanical Engineering and Ocean Engineering

Kenneth Baldwin

Professor of Mechanical Engineering and Ocean Engineering

Lloyd Huff

Adjunct Professor in Ocean Engineering

Darrell R. Jackson

Research Professor of Electrical Engineering

University of Washington

08/24/01

Date

ii

ACKNOWLEDGMENTS

TABLE OF CONTENTS

v

vi

LIST OF TABLES

LIST OF FIGURES

ABSTRACT

A MODEL FOR BACKSCATTERING ANGULAR RESPONSE OF GASSY SEDIMENTS: APPLICATIONS TO PETROLEUM EXPLORATION AND DEVELOPMENT PROGRAMS

by

Luciano Emidio Neves da Fonseca

University of New Hampshire, December 2001

The location and distribution of near-surface gas in continental margins is of particular interest for oil exploration and development programs. The presence of gas seepages can be evidence of the possible existence of subsurface hydrocarbon reservoirs. Gas is also a potential hazard for offshore facilities, as it decreases the strength of unconsolidated sediments increasing the risk of seafloor failures and slumps.

Acoustic remote sensing systems such as multibeam and sidescan sonars can be used for mapping and detection of near-surface gas in marine sediments. These systems provide a realistic depiction of the seafloor by means of the simultaneous acquisition of co-registered high-resolution bathymetry and calibrated seafloor backscatter. The

recognition of gas signatures in acoustic remote sensing data depends on the proper modeling of the acoustic backscatter response. In this thesis, a high frequency backscatter model that takes into account the amount of free gas in the sediments is proposed. Inversion of this model is used to estimate the distribution of near-surface gas in the sedimentary basin. Additionally, analysis of backscatter images and detailed bathymetry reveals anomalous seafloor features, which are associated with gas expulsion.

The acoustic remote sensing data is analyzed in conjunction with other layers of information available in the exploration region, including a core database, structural maps, location of wells, geochemical data and geophysical data. This analysis attempts to link anomalous acoustic backscatter on the seafloor to sub-surface structures, a necessary step toward the understanding of the stratigraphic or tectonic control of seafloor seepages. New visualization techniques, which take advantage of 3D tools and GIS integration, are used to help analyze and understand these complex relationships in a natural and intuitive manner.

INTRODUCTION

Terrestrial hydrocarbon exploration and production has benefited greatly from aerial photography and electromagnetic remote sensing. In the offshore, however, where optical and electromagnetic sensors are of limited value, we must turn to acoustic techniques to provide detailed information on the nature of the seafloor and the subsurface. The application of "acoustic remote sensing techniques" to problems of hydrocarbon exploration and production is in its naissance. This thesis explores the potential of this approach and in particular the use of high-resolution multibeam sonar data, in combination with newly developed analytical and visualization techniques for better understanding both the hydrocarbon and geohazard potential of offshore regions.

The thesis begins with a brief review of the application of traditional remote sensing techniques to terrestrial hydrocarbon problem and then a review of the acoustic techniques used in the offshore (in this introduction). In Chapter 1 a new model is developed for the high-frequency backscatter angular response of gassy sediments. This model can be used to better interpret the acoustic response of seafloor sediments and potentially for the direct extraction of the gas-content of near-surface sediments from acoustic data. Chapter 2 describes the development of an approach for using both a 2-D GIS and an innovative

interactive 3-D GIS system for analyzing the complex inter-relationships amongst multiple geological and geophysical data sets. Finally, in Chapter 3, both the model and the interactive GIS are used to explain the cause of acoustic backscatter anomalies in the near-surface sediments of a hydrocarbon rich-area off the coast of northern California.

Remote Sensing Applied to Hydrocarbon Exploration

Electromagnetic remote sensing and aerial photographs have been used for decades as an aid for locating geologic structures that may contain oil and natural gas. These techniques are incorporated early in exploration programs as a reconnaissance-mapping tool for a large region, and then used for the selection of smaller areas with lower exploration risk. Subsequently, the selected areas are examined in detail by applying more expensive subsurface geophysical techniques such as seismic reflection and refraction. The central idea is to focus the more expensive exploration techniques in regions of higher petroleum potential.

The analysis of remote sensing data in support of petroleum exploration is based on the spatial and spectral signatures of targets in the images (Berry and Prost, 1999). The spatial signatures include the geomorphology, structural arrangements, regional structural trends as well as distribution of faults and folds. The spatial signature also includes the texture imprinted by different surface materials on the

2

image. On the other hand, the spectral signature reveals variations in electromagnetic energy reflected or emitted by different materials exposed on the land surface.

The spatial signature of a remotely sensed image shows important elements of the geologic structural framework based on what is observed on the surface. As exploration continues, this surface expression can be related to subsurface structures, using additional information from known wells or seismic lines. This analysis is essential for the identification of structural highs such as anticlines and domes, which are primary exploration targets. Examples of structural information that are typically derived from remote sensing data are the dip angle of rock layers and the surface expressions of folds. Folded structures are recognized by the opposing dips of rock layers and by their topographic expression. Other techniques for recognizing these structures include the identification of atypical drainage or vegetation, irregular joint patterns, and anomalous mineral distributions. Additionally, fracture structures are identified as linear features on remote sensing images. This approach has been one of the most common applications of remote sensing data, allowing for the mapping of joints, faults and their offsets, thrusts, rollovers, slides and other linear expressions on the surface. Besides the structural information, remote sensing can be used to delineate sedimentary basins and directly locate outcrops. Remote sensing images

3

also serve as base maps for installations and other logistical aspects of the hydrocarbon production process.

The proper processing and interpretation of remotely sensed images permit the classification of surface materials and their properties. In many cases, it is possible to discriminate lithologies and to differentiate the surface distribution of multiple formations or rock units. This discrimination is based on both spectral and spatial signatures. Classification techniques based on the spectral signature of surface materials are normally applied to multispectral remote sensing data. In a multispectral image, each pixel is a multidimensional vector containing the reflectance of surface materials in various spectral windows. For the classification, each pixel is treated as a multivariate variable that is assigned to a clustered class based on some statistical distance. For single band remote sensing, the classification is normally based on the spatial signature observed on the image. Different spatial signatures are related to the distribution, to the erosional characteristics and to the variation of the exposed material (Chavez & Gardner, 1994). These anomalous distributions are observed as a texture pattern of a particular target on the image. A typical example is the classification of radar images, which rely mainly on textural differences (Miranda et al., 1997).

Remote sensing analysis is also used in the direct detection of hydrocarbons. The detection is done though the identification of surface

4

expressions and surface indicators of the possible presence of a subsurface hydrocarbon reservoir (Mello et al., 1990). In accordance with the principle of vertical migration, hydrocarbons escape from a subsurface reservoir, leaking through an imperfect cap rock or by reservoir spill, and then migrate upward where they may be trapped in sediments and soil (Rice, 1985). Applying this principle, the location of hydrocarbon seepages was one of the most successful of the early prospecting techniques. Most of the world's major petroleum producing areas were first explored because of a visible seepage of oil or gas (Link, 1952).

Hydrocarbon seepages can be located in remote sensing images though the analysis of the spectral behavior of surface targets. The mapping is done through the identification of stressed vegetation or through the detection of alterations on surface rocks (Oliveira and Crósta, 1996). Some plants absorb traces of hydrocarbons present in the soil, and consequently display abnormal spectral signatures and variation in density. In some cases, variations in the distribution of plant species were reported due to the presence of hydrocarbons in the soil. Additionally, hydrocarbon seepages induce diagenetic reactions on surface rocks. These altered rocks show different spectral behavior in a multispectral image set (Matthew,1985).

Remotely sensed images are also used to help understand the tectonic control of seafloor seepages, since zones of faults and fractures often delineate areas of higher fluid escape (Mello et al., 1990). With these images, it is possible to define regional structural trends and thus determine where the application of surface geochemical techniques would be most successful in evaluating the regional hydrocarbon potential. The combining of remote sensing and surface geochemistry can be applied to exploration of large areas at a fraction of the cost compared to conventional techniques.

Moving Towards Deep-Water Exploration

In recent years, hydrocarbon exploration has moved offshore to deep-water targets where there is still a great potential for finding new oil reserves. In these marine regions, a detailed depiction of the offshore seabed morphology and geology is essential for oil exploration and mining. The same level of detail is required for underwater engineering applications such pipeline laying, cable routing, platform siting, etc. In addition, with the U.N. Law of the Sea Act, which confers sovereign rights in the exclusive economic zones, (and potentially beyond) this detailed depiction of the seafloor will become extremely important for the economy of the majority of coastal nations.

An approach similar to terrestrial remote sensing exploration is essential for the study of the new vast and unknown offshore prospecting

6

areas. Unfortunately, the conventional electromagnetic remote sensing approaches discussed above are inadequate for underwater exploration (Joseph et al., 1997). Water absorbs electromagnetic energy very rapidly due to its strong conductivity and dissipative characteristics, limiting the use of electromagnetic remote sensing to very shallow water. These problems are amplified as the water becomes more saline.

Acoustic waves, which propagate as mechanical vibrations, however, are more pertinent to underwater exploration. Acoustic methods in the form of conventional single beam echo sounders and seismic profilers have been used for some time. These two methods were the principal source for earlier seafloor mapping data (Tyce, 1986). Single beam echo sounders use an acoustic transmitter and receiver (transducer) to measure the two-way travel time of a sonar signal to the seafloor; the depth can be derived from the two-way travel time if the sound speed profile of the area is known. In addition to basic measurements of two-way travel time, the intensity of the echo that returns to the transducer (backscatter) and sometimes the complete waveform of the returning signal are also recorded. The shape of the waveform, the backscatter and the two-way travel time can be used to determine some of the physical characteristics of the seafloor (Djikstra, 1990).
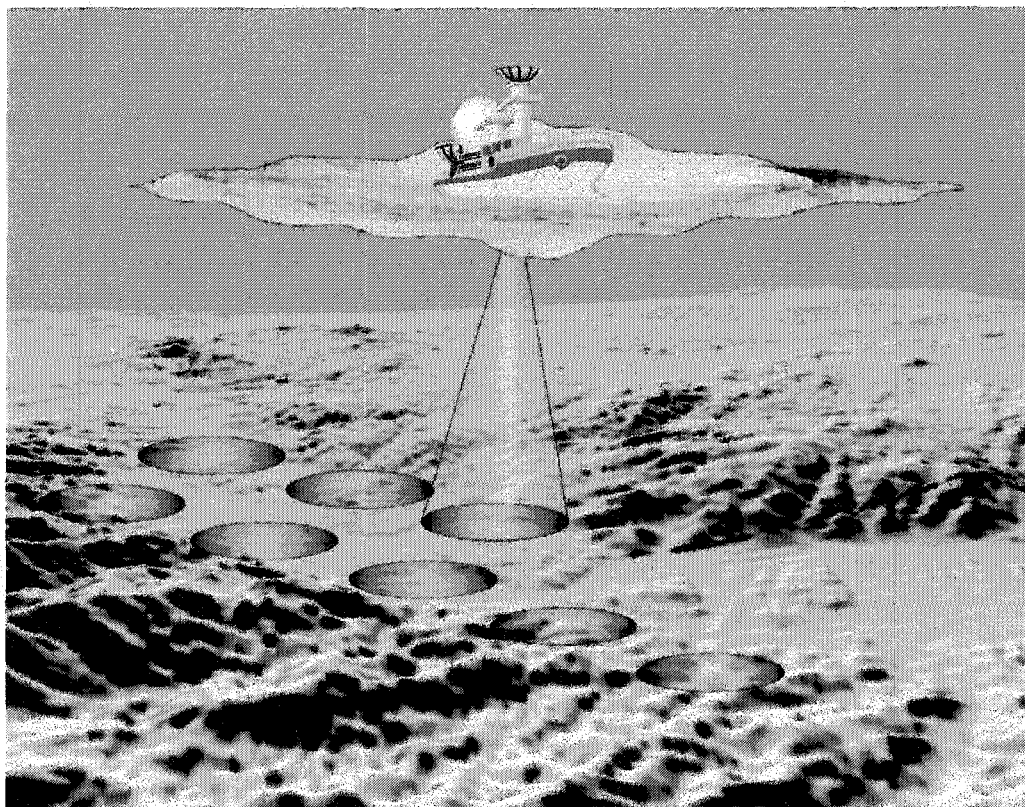
Figure I.1 – Single-beam echo sounder and its sparse sampling of the seafloor.

Single beam echo sounders are not able to provide a detailed morphological characterization of the seafloor comparable to what is possible with remote sensing techniques on land (Laughton, 1981). This limitation is due to the relative sparse sampling of the seafloor normally achieved by single beam echo sounders (Fig. I.1). These systems do not provide lateral angular coverage, as they operate with only one vertical acoustic beam. An unrealistic amount of survey time is necessary to achieve detailed seafloor coverage with single beam echo sounders.

8
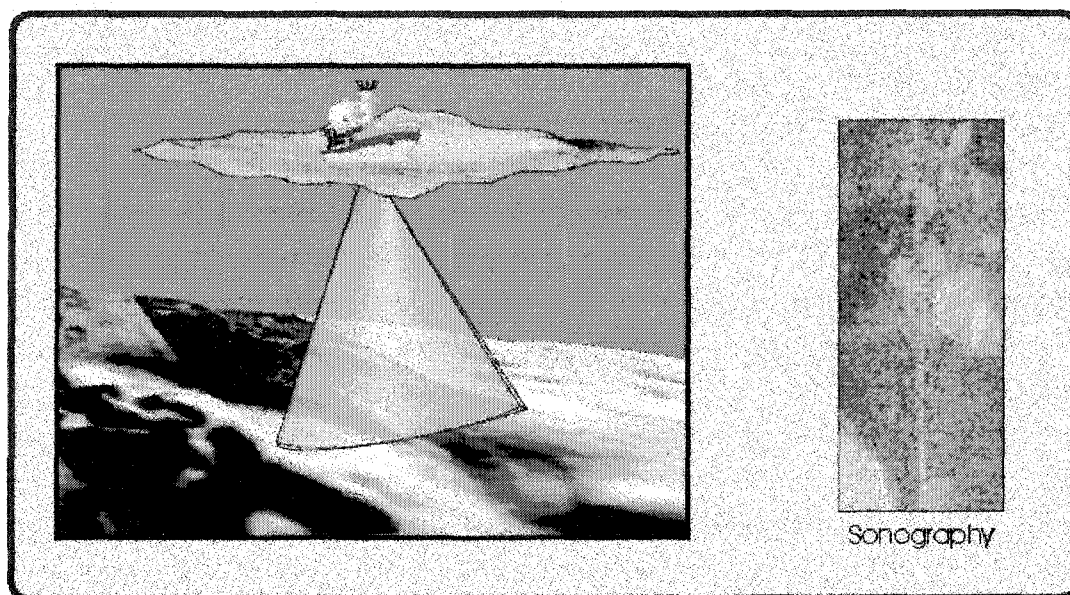
Figure I.2 – Sidescan sonar mapping to produce a sonograph.

In recent years acoustic systems have been designed to provide complete seabed coverage, which was the major limitation of single beam echo sounders. The first attempt was the sidescan sonar, a system that uses an array of transducers to generate a fan-shaped beam of sound narrow in the along-track direction (navigation direction) and broad in the across-track direction (Fig. I.2). The basic measurement of the sidescan sonar is the acoustic backscatter, although some systems achieve depth estimates by means of interferometric properties (Kolouch, 1984). A seafloor acoustic image (sonography) can be assembled by properly co-registering the backscatter measurements. The main limitation of sidescan sonar is its inability to provide reliable bathymetric measurements.

9
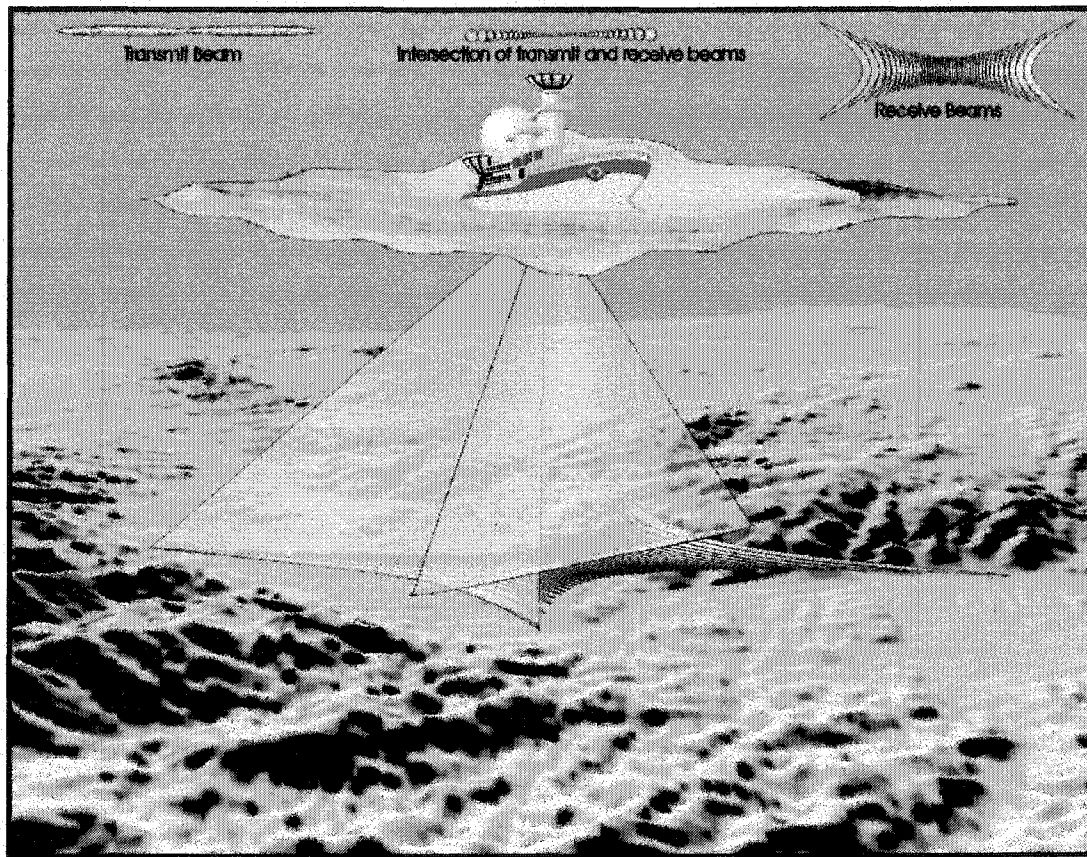
Figure I.3 – Multibeam acquisition geometry.

The next advance came with the development of the multibeam sonar, a system that measures depths simultaneously from a series of beams pointing at discrete angles of incidence in the across-track direction (de Moustier, 1988). Most multibeam sonars also collect acoustic backscatter information simultaneously with depth measurements, providing backscatter imagery spatially co-registered with the depth information. These systems combine the qualities of both single beam echo sounders and sidescan sonar. Instead of the sparse sampling associated with single-beam echo sounders, multibeam sonars

10

provide reliable bathymetric measurements over a wide angular sector beneath the vessel (Fig. I.3). With proper survey design, complete seafloor coverage is achievable.

Accessibility of Acoustic Remote Sensing Data

Following the extraordinary development of swath mapping systems such as multibeam and sidescan sonars, accurate bathymetric and backscatter data is now available for underwater areas. This development was a consequence not only of advances in sonar technology, but also in marine positioning (Mayer et al., 1999). With the Differential Global Positioning System (DGPS) precise navigation fixes are possible. This is essential for acoustic remote sensing mapping in deep water. In addition, inertial systems can now provide reliable vessel orientation measurements, solving problems associated with vessel attitude. Another important development was in computer processing capability. Multibeam swath systems produce enormous amounts of data, which makes processing and managing this information difficult. Advances in real time computing and data storage have permitted better data management and near time processing during the survey (Hughes-Clarke et al., 1997). It is the developments in sonar technology along with advances in positioning, motion sensors and processing technology that can now provide the critical knowledge needed to determine accurate seafloor depth information.

11

Acoustic remote sensing data from swath systems are now being collected continuously in hydrographic and bathymetric operations. At the moment, worldwide seafloor coverage is not yet accessible, but the necessary data is slowly being acquired. After the declaration of the Exclusive Economic Zone (EEZ), which extends the coastline to 200 miles offshore, many countries have begun systematic mapping of their newly extended territory. In 1984, the US Geological Survey launched a program using a long-range sidescan sonar system (GLORIA) to study the entire American Exclusive Economic Zone, encompassing more than 13 million square kilometers (Groome et al., 1997). Similar plans to map the complete Brazilian Atlantic coast with precise swath sonars are in development. The main objective of this project (project REMPLAC) is to evaluate the potential of the Brazilian legal Continental Self for mineral exploration. In April 1999, the New Zealand government announced its intention to claim Continental Shelf rights for seabed resources by 2006. This area extends the maritime boundaries of New Zealand to far beyond the Exclusive Economical zone. In order to justify this claim, The Royal New Zealand Navy will conduct a detailed seafloor mapping of its coast in order to better delineate its continental shelf. Starting in 2000, the Geological Survey of Ireland will begin a complete seabed survey of the Irish offshore territory. This survey will cover more than 900,000 square kilometers, which is ten times the Irish land territory.

12

In addition to EEZ spawned surveys, legacy data from many swath bathymetry surveys have already covered various ocean basins, and in some cases can be accessed. The 'ETOPO-5' data set, from the U. S. National Geophysical Data Center (NGDC), was generated from a compilation of numerous elevation charts from land and from the seafloor, on a 5-minute latitude/longitude grid. Satellite altimetry from The U.S. Navy GEOdetic SATellite (GEOSAT), from the European Remote-Sensing Satellites (ERS-2 and ERS-2), and from the TOPEX/Poseidon satellite provide measurements of the mean sea surface and gravity anomaly maps from all the oceans in a 1.5km grid. A program that systematically covers the entire seafloor, similar to the Landsat program on land, is already being discussed in the U.S. (Vogt et al., 2000).

Multibeam Sonar and Underwater Oil Exploration

Multibeam sonar data can be used in the geological interpretation of oil exploration areas in the marine environment, playing the same role as electromagnetic remote sensing images play in land exploration. This sort of data provides the interpreter with the ability to extract quantitative information about the shape and character of the seafloor. Almost all exploration techniques discussed for single band remote sensing exploration are valid for seafloor backscatter images.

The spatial signature can be extracted from the single band backscatter image and from the precise swath bathymetry. Techniques

13

similar to those used for single-band remote sensing data can then be applied to the characterization and to the classification of backscatter. In this way, geological analysis is done based on surface expressions of structures that are exposed in backscatter images (Davis et al., 1986). The spectral signature is not depicted in the acoustic remote image, as these images are normally acquired at one acoustic frequency. Some attempts have been made to survey with dual-frequencies, providing a better potential to characterize underwater terrains (Ryan, 1995). Although there is a potential in this approach, this kind of data is not widely available.

In some cases the lack of a spectral signature in acoustic remote sensing data can be compensated by the analysis of angular dependence of the backscatter data. Hull-mounted multibeam systems map the seabed through a wide variation in grazing angles (Fig. I.3). The variation of backscatter strength as a function of the grazing angle represents, for a certain frequency, an inherent property of the seafloor (Hughes Clark et al., 1997). This angular variation or angular signature reveals subtle differences in the backscatter response of different materials on the seafloor.

An acoustic backscatter model is an essential tool to link angular signatures measured by a multibeam sonar to seafloor properties. In this thesis we propose a model that predicts the backscatter angular

14

response of marine sediments as a function of sediment properties, water depth and gas content. When applied to multibeam sonar data, this model can be used to predict and recognize distinctive backscatter signatures caused by the presence of gas.

This model is important because the location and distribution of near-surface gas in continental margins is of particular interest for offshore oil exploration and development programs. Gas seepages can be the result of upward migration from deep-seated reservoirs and thus a potential indicator of hydrocarbons. The identification of near-surface gas by acoustic remote sensing techniques could thus provide a first evaluation of the hydrocarbon potential of an offshore area and reduce considerably the exploration risk. Gas is also a potential hazard for offshore engineering facilities, as it reduces the strength of unconsolidated sediments increasing the risk of seafloor failures and slumps.

Using the model developed, acoustic remote sensing data is analyzed in conjunction with other geological, geophysical and geochemical data from the exploration area. The analysis attempts to link anomalous acoustic backscatter on the seafloor to sub-surface structures, a necessary step toward the understanding of the stratigraphic or tectonic control of seafloor seepages. Such analysis is done with the aid of a Geographical Information System (GIS). A GIS

15

system acts as a vast data repository, where the acoustic remote sensing data will be analyzed in conjunction with other layers of information available in the exploration region. New visualization techniques, which take advantage of 3D tools and GIS integration, are used to help analyze and understand the complex relationships among layers in a natural and intuitive manner.

CHAPTER I

THE HIGH-FREQUENCY BACKSCATTERING ANGULAR RESPONSE OF GASSY SEDIMENTS

1.1 Abstract

A model for the high-frequency backscatter angular response of gassy sediments is proposed. For the interface backscatter contribution we adopted the model developed by Jackson et al. (1986), but added modifications to accommodate gas bubbles. The model parameters that are affected by gas content are the density ratio, the sound speed ratio and the loss parameter. To a first approximation, the model roughness parameters are not influenced by the presence of gas. For the volume backscatter contribution we developed a model based on the presence and distribution of gas in the sediment. We treat the bubbles as individual discrete scatterers that sum to the total bubble contribution. This total bubble contribution is then added to the volume contribution of other scatters. The presence of gas affects both the interface and the volume contribution of the backscatter angular response in a complex way that is dependent on both grain size and water depth. The backscatter response of fine-grained gassy sediments is dominated by the volume contribution while that of coarser-grained gassy sediments is affected by both. In deep water (>400m) the interface backscatter is only

slightly affected by the presence of gas while the volume scattering is strongly affected. In shallow water the interface backscatter is severely reduced in the presence of gas while the volume backscatter is only slightly increased. Two different sets of multibeam data acquired offshore Northern California at 30kHz and 95kHz provide raw measurements for the backscatter as a function of grazing angle. These raw backscatter measurements are then reduced to scattering strength for comparison with the results of the proposed model. The analysis of core samples at various locations provides local measurements of physical properties and gas content in the sediments that, when compared to the model, show general agreement.

1.2 Introduction

Fine-grained sediments from continental margins are frequently rich in bubbles of free gas (Richardson and Davis, 1998). These gas bubbles, even in very small quantities, can dominate and change the geoacoustic characteristics of seafloor sediment and have a significant effect on the propagation of acoustic waves (Lyons et al. 1996, Anderson et al., 1998, Wilkens and Richardson, 1998). Anderson et al., (1998) describe three types of bubbles in sediments, in order of increasing size and disturbance: 1-interstitial bubbles which are very small bubbles within the undistorted interstitial pore spaces of the sediment; 2-reservoir bubbles which are a reservoir of gas occupying a region of

18

undistorted sediment solid framework larger than the normal pore space; and 3- sediment displacing bubbles which are bubble cavities that are larger than the normal interstitial space and that are surrounded by either undisturbed or slightly distorted sediments. While the nature of the effect on acoustic propagation will differ with the type of bubbles, in general, if gas bubbles are trapped in the sediment structure, their scattering contribution will be stronger than the contribution of other scatterers and will control the total backscattering response. In this paper, we propose a high frequency (to 100 kHz) acoustic backscatter model for the seafloor that takes into account the contribution of gas bubbles and then we test the model against both multibeam sonar backscatter data and core data collected in regions known to have gassy sediments.

Traditionally, high frequency backscatter cross-section models consider two different processes: interface scattering and volume scattering (Ivakin, 1998). The interface scattering occurs at the water-sediment interface, where the seafloor acts as a reflector and scatterer of the incident acoustic energy. A portion of the incident acoustic energy will be transmitted into the seafloor. This transmitted energy will be scattered by heterogeneities in the sediment structure, which are the source of the volume scatter (Novarini and Caruthers, 1998). In the approach developed in this paper we explore how that these two contributions are affected by the presence of gas.

For the interface backscatter contribution we have adopted the model developed by Jackson et al. (1986), but added modifications to accommodate gas bubbles. Interface backscatter is normally dependent on the acoustic impedance as well as the acoustic attenuation in sediments, both of which are affected by the presence of gas. The results of Anderson and Hampton (1980a, 1980b), who modeled the influence of gas bubbles on sediment properties, will be used to estimate the changes in interface backscatter.

Models for volume scattering include refraction at the water-sediment interface and attenuation in the sediment, both of which are altered when gas is present. For the volume backscatter contribution we have developed a model based on the presence and distribution of gas in the sediment. We treat bubbles as individual discrete scatterers that integrate to create the total bubble contribution. The integration is based on the statistical distribution of bubble sizes, derived from measured histograms in muddy sediments (Anderson et al., 1998). This total bubble contribution is then added to the volume contribution of other discrete scatterers.

To test the ideas outlined above we use data collected on the highly sedimented Eel River margin offshore northern California. The Eel River basin was extensively investigated as part of the *STRATAFORM* (STRATA FORmation on the Margins) project, a multi-year, multi-investigator

20

program funded by the U.S. Office of Naval Research (Nittrouer, 1998). During this project, an immense database of marine information was collected (Mayer et al. 1999), including two different sets of multibeam sonar backscatter data collected at 30kHz and 95kHz and numerous core sampling sites with measurements of sediment physical properties and free gas content. Multibeam sonar systems map the seabed through a wide range of grazing angles, revealing subtle differences in the backscatter response for different materials on the seafloor (de Moustier and Alexandrou, 1991). In this study, multibeam-sonar raw backscatter measurements will be reduced to scattering strength for comparison with the results of the proposed model. The analysis of core data provides local measurements of physical properties and gas content that are used as input parameters for the model. The model results at the core locations are then compared to the multibeam sonar measurement.

1.3 Interface Backscatter

The composite roughness model developed by Jackson et al. (1986) estimates the interface backscattering cross section (σ_r) for a particular seafloor type as a function of frequency and grazing angle. It is based on a hybrid method that takes into account the Rayleigh-Rice small perturbation solution, with the local grazing angle dependent on the slope of the large-scale surface. This model defines the seafloor type based on five parameters that reflect sediment physical properties and

21

seafloor roughness (Eq. (1)): a) two parameters for impedance: sound velocity ratio (*v*) and density ratio (*ρ*); b) one parameter for attenuation: loss parameter (*δ*), and; c) two parameters for roughness: the spectral strength (*ω₂*) and the spectral exponent of bottom relief (*λ*). The acoustic frequency (*f*) and the grazing angle (*θ*) of the wave front with the seafloor are treated as given parameters. The modeling function for σ_r is calculated as a combination of the Kirchhoff solution for grazing angles near vertical incidence and the composite roughness solution for other angles. The actual expression and solution for Eq. (1) can be found in Mourad and Jackson (1989).

$$\sigma_r(\theta, f) = F(\theta, f; \quad \rho, v, \delta, \omega_2, \lambda) \tag{1}$$

σ_r Interface backscattering cross-section per unit solid angle per unit area.

θ Grazing angle.

f Frequency.

ρ Ratio of sediment mass density to water mass density.

v Ratio of sediment sound speed to water sound speed.

δ Loss parameter: ratio of imaginary to real wave number for the sediment.

22

ω_2 Spectral strength of bottom relief spectrum (cm^4) at wavenumber 1 cm^{-1}

λ Spectral exponent of bottom relief spectrum

In our approach we assume that this interface backscattering will be affected by the presence of gas bubbles in the sediment through their impact on seafloor geoacoustic properties. An extra parameter ξ, which is the volume fraction of free gas in the sediment, is added to the model. The model parameters most affected by the gas content are the density ratio, the sound speed ratio and the loss parameter. While there may be large-scale features such as pockmarks or mud volcanoes (with length scales of 10's to 100's of meters) associated with gas expulsion, these features will have little influence on the small footprints of the 95 kHz multibeam echo sounder. Thus, to a first approximation, we assume that the model roughness parameters will not be influenced by the presence of gas.

The interface backscattering cross-section per unit solid angle per unit area σ_r, modified to take into account the gas content of sediments, is now dependent on six parameters:

$$\sigma_r(\theta, f) = F(\theta, f; \quad \xi, \rho(\xi), \nu(\xi), \delta(\xi), \omega_2, \lambda) \tag{2}$$

ξ Free gas = gas volume/ total sediment volume.

23

The influence of gas bubbles on sediments was modeled by Anderson and Hampton (1980a, 1980b). We apply this approach to derive expressions for $\rho(\xi)$, $v(\xi)$ and $\delta(\xi)$. One simplification used in this work is to consider marine sediments as water-saturated aggregates of particles with no rigid skeletal frame. In doing this, we follow the approach of Jackson and Ivakin (1998), who assume that the shear modulus of elasticity for the marine sediments is zero. This is a reasonable assumption for the upper few decimeters of unconsolidated sediments (the probable limit of penetration of a 95kHz multibeam sonar), especially for silt and clays (Mourad and Jackson, 1989). Another assumption is that the sediment volume does not change when gas is added, i.e., gas just replaces the water in the sediment body. With these assumptions, the density ratio of gassy sediment, with a volume fraction ξ of free gas, will be:

$$\rho(\xi) = \frac{\rho_s - \xi(\rho_w - \rho_g)}{\rho_w} \tag{3}$$

Where:

ρ_g Density of the gas.

ρ_w Density of interstitial water.

ρ_s Density of the gas-free water/sediment aggregate.

24

The sound speed in gassy sediments is highly dependent on the resonance frequency of gas bubbles. The resonance frequency for a gas bubble of radius a, inside a water/sediment aggregate is inversely proportional to the bubble size (Eq. (4)).

$$f_0 = \frac{1}{2\pi a}\left(\frac{3\gamma P_o}{A\rho_s}\right)^{\frac{1}{2}}$$ (4)

Where,

f_o Resonance frequency for a gas bubble of radius a.

a Bubble radius.

γP_0 Bubble stiffness.

γ Ratio of specific heat of the gas.

P_0 Ambient hydrostatic pressure.

A Polytropic coefficient

The polytropic coefficient characterizes the thermodynamic process involved during bubble pulsation and the relationship between bubble volume and pressure (Anderson and Hampton, 1980a). In the range of frequencies of multibeam sonar, the full expression for the polytropic

25

coefficient A should be used (Eq. 5a). The auxiliary variable B of Eq. 5b is the thermal damping constant.

$$A = (1 + B^2)\left(1 + \frac{3(\gamma - 1)}{x}\left(\frac{\sinh x - \sin x}{\cosh x - \cos x}\right)\right)$$

(5a)

$$B = 3(\gamma - 1)\left(\frac{x(\sinh x + \sin x) - 2(\cosh x - \cos x)}{x^2(\cosh x - \cos x) + 3(\gamma - 1)(\sinh x - \sin x)}\right)$$

(5b)

Where,

$$x = a\sqrt{\frac{2\pi f \rho_g s_p}{C_g}}$$

s_p Specific heat at constant pressure of the gas.

C_g Thermal conductivity of the gas.

One of the most difficult quantities to model is the distribution of gas bubble sizes. Gas bubbles in fine-grained sediments exist in a range of sizes, but have rarely been directly measured. Anderson et al. (1998) used an X-ray CT scanner to produce both a qualitative and quantitative characterization of bubble size population from cores collected in muddy sediments from Eckernforde Bay, on the Baltic coast. Their technique has a resolution limit of 0.42 mm and thus their size distribution histograms appear to be the larger bubble segment of a peaked size distribution similar to that seen for populations of bubbles in seawater

26

near the ocean surface (Farmer and Vagle, 1989). The number of bubbles Anderson et al. (1998) observed in their sediment samples increased monotonically as bubble size decreased. While they were unable to measure bubbles smaller than 0.42 mm, Anderson et al., (1998) speculate that the peak in their size distribution may be near this resolution limit, but they also present circumstantial evidence (the increase in normally incident energy between 15 and 30 kHz, returned from the sediment-water interface) for the existence of very small bubble in the upper few cm of the seafloor. The histograms of bubble size in muddy sediments depict slightly smaller bubble sizes than those found in water due to the higher viscosity of the mud. Boyle and Chotiros (1995) used a similar histogram for bubble sizes in soft sediments. The histogram used in our examples is based on these three previous works and is normalized for a water depth of 20m. It follows the distribution measured by Anderson et al. for the larger bubble fraction and allows the probability of small size bubbles as discussed by Boyle and Chotiros. The minimum bubble radius used in the modeling is 180μm, which is the resonance radius at 95kHz for the deepest part of the survey area. For bubbles larger than the minimum size, the histogram decreases monotonically with a constant slope on a log-log graph (Fig. 1.1). The dashed part of the histogram was not actually used in the calculations, and shows only a probable theoretical shape for the bubble size

27

distribution. Based on this histogram, we can define a probability density function z(a) of bubble sizes.

$$z(a) = \frac{\partial Z_a(a)}{\partial a}$$

(6)

Where,

z   Probability density function of bubble sizes

Z_a bubble distribution: bubbles per unit volume with radius less than a.
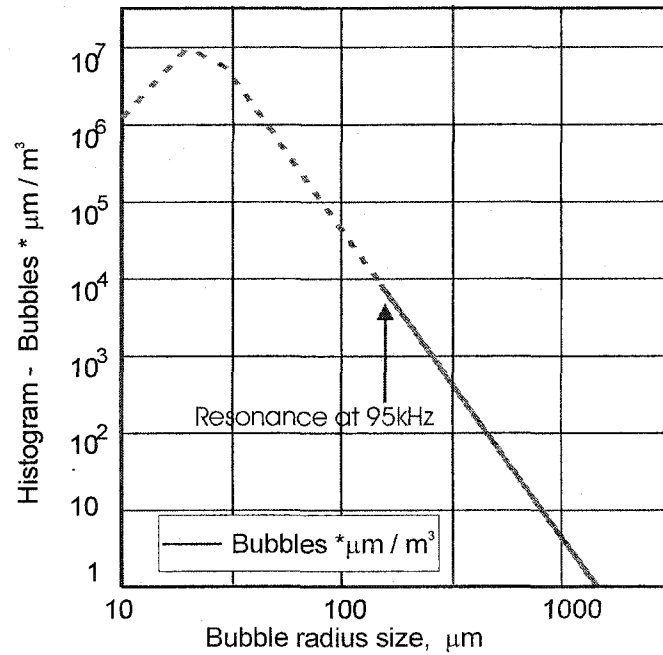
Figure 1.1- Bubble size histogram. Number of bubbles per unit of volume (m³) over a bubble radius bin of 1μm.

28

For the sound-speed ratio, we used the expression for gassy water formulated by Silberman (1957), but adapted for the case of fine-grained sediments. The bulk modulus of elasticity of the water, present in the original expression, is substituted with the bulk modulus of the gas-free water/sediment aggregate.

$$v(\xi) = \cfrac{c_s}{c_w \sqrt{\cfrac{1}{2}\left(1 + \cfrac{\rho_s c_s^2 X_1}{\gamma P_o}\right)\left[1 \pm \sqrt{1 + \left(\cfrac{\rho_s c_s^2 Y_1}{\gamma P_o + \rho_s c_s^2 X_1}\right)^2}\right]}}$$

(7)

Where,

c_s Sound speed for the gas-free water/sediment aggregate.

c_w Sound speed in water.

The expressions for X_1 and Y_1 are the same used by Anderson and Hampton (1980a), modified to take into account the proposed bubble distribution.

$$X_1 = \int_{a_{min}}^{a_{max}} \cfrac{\xi\left(1 - \cfrac{f^2}{f_0^2(a)}\right)}{\left(1 - \cfrac{f^2}{f_0^2(a)}\right) + d_c^2(a)\cfrac{f^4}{f_0^4(a)}} z(a)da$$

(8a)

29

$$Y_1 = \int\limits_{a_{min}}^{a_{max}} \frac{d_c(a)\dfrac{f^2}{f_0^{\,2}(a)}}{\left(1-\dfrac{f^2}{f_0^{\,2}(a)}\right)+d_c^{\,2}(a)\dfrac{f^4}{f_0^{\,4}(a)}} z(a)da$$

(8b)

Where:

$$d_c(a) = B + \frac{\rho_s a^3 w^3 A}{3\gamma P_0 c_s} + \frac{8\pi f \mu A}{3\gamma P_0}$$ Bubble damping constant.

μ Viscosity of the gas-free water/sediment aggregate.

The attenuation of sound in the aggregate is also a function of the bubble distribution (Anderson and Hampton, 1980a), and can be expressed as:

$$\alpha(\xi) = \frac{\pi f v(\xi) c_w \rho_s}{\gamma P_o} Y_1$$

(9)

Where,

$\alpha(\xi)$ – Attenuation coefficient in dB/m for a gassy sediment

Finally, the loss parameter is defined as the ratio of the imaginary part to the real part of the complex sediment acoustic wavenumber. It is related to the attenuation coefficient, the frequency and the sound-speed in the gassy sediment (Mourad and Jackson, 1989).

30

$$\delta(\xi) = \frac{\alpha(\xi)v(\xi)c_w \ln(10)}{40\pi f}$$

<div align="right">(10)</div>

1.4 Volume Backscatter

In areas predominantly covered with sediments, the volume scattering from sub-bottom sediment layers or from discrete scatterers within the upper sediment layers can contribute extensively to the total backscattering cross section intensity. The model for volume scattering should include refraction at the sediment interface and attenuation in the sediment itself. On a rough seafloor, the penetration of the acoustic field in the sediment is very small for grazing angles smaller than the critical angle. This is an important issue because this reduces drastically the volume backscattering contribution for shallow grazing angles. The refracted energy will be attenuated as it travels through the sediment structure, making the attenuation coefficient a key parameter for the estimation of volume scattering.

In their approach for determining volume scatter, Jackson and Briggs (1992) consider the sediment a statistically homogeneous semi-infinite propagation medium delimited by a rough surface. With this simplification they define a volume backscattering cross section equivalent to the interface, using a similar solution to the one proposed by Stockhausen (1963). The total volume contribution is dependent on a free parameter σ_2, which is calculated based on the ratio of the sediment

<div align="center">31</div>

volume scattering cross section to sediment attenuation coefficient. In our proposed model, we regard the parameter σ_2 as a measurement of the volume contribution of general heterogeneities. Its equivalent volume scattering cross section will be added to the calculated volume scattering cross section from gas bubbles.

The scattering mechanism of bubbles in a lossy fluid was studied by Anderson and Hampton (1980b). In their formulation, the total scattering cross section of sound though a bubble screen is highly dependent on the resonance frequency of the bubbles. The actual acoustic cross-section at resonance can be hundreds of times the bubble physical cross-section. If we have a distribution of bubble sizes in the sediment body, we can calculate the sediment volume backscattering cross-section per unit of volume, as the sum of the contribution of all individual bubbles within that volume (Boyle and Chotiros 1995). The following expression extends the formulation of Anderson and Hampton (1980b) for the probability density function of bubble sizes of Eq. (6).

$$\Sigma_b = \int_{a_{min}}^{a_{max}} \frac{a^2}{\left[\left(\frac{f_0(a)}{f} \right)^2 - 1 \right]^2 + \left(\frac{f_0(a)}{f} \right)^4 d_c(a)^2} z(a)da \qquad (11)$$

Where,

Σ_b – backscattering cross section for a bubble distribution.

32

The volume backscattering cross section of bubbles Σ_b is calculated per unit of volume, as the bubble distribution accounts for number of bubbles per unit of volume. Consequently, Σ_b should be scaled to reflect the volume fraction of free gas ξ. This scaled contribution is then added to the volume scattering cross section of other heterogeneities (other than gas bubbles), as described by the parameter σ_2. The total volume scattering cross section will be:

$$\sigma_v(\theta) = \frac{5\left(\xi\Sigma_b + \sigma_2\alpha(\xi)\right)c_w\left|1 - R^2(\theta)\right|^2 \sin^2(\theta)}{40\pi f \left|P(\theta)\right|^2 \operatorname{Im}\left|P(\theta)\right|} \tag{12}$$

Where,

σ_v Volume backscattering cross-section equivalent to the interface.

σ_2 Volume scattering parameter.

$R(\theta)$ Complex reflection coefficient.

$P(\theta)$ Complex function for the forward loss model, as defined in Mourad and Jackson (1989)

The small scale backscattering cross-section of Eq. (2), as well as the equivalent volume cross-section of Eq. (12), should be averaged over the bottom slope to account for the effects of local slope and shadowing (Jackson et al. 1986). The numerical solution for Eq. (2) and Eq. (12)

33

reveals a complex relationship involving grain-size, depth and gas fraction. In Fig. 1.2, the model response is calculated for various gas fractions using two different grain sizes (left and right columns of Fig. 1.2 respectively). The same computation is repeated for 3 different depths: 50, 350 and 800m (rows of Fig. 1.2). The result of this modeling shows that the backscatter response of fine-grained, gassy sediments is basically controlled by the volume contribution, while coarser grain size sediments present both volume and interface backscatter contributions due to existence of gas.

In deeper waters, the interface backscatter is only slightly reduced by the presence of gas, as a consequence of the higher bubble stiffness at higher ambient pressure (Eq. 7).). Bubble stiffness is defined as the product of the specific heat of the gas and the ambient pressure (γ P_0). On the other hand, even small amounts of gas can cause a large increase in the volume contribution in deep water, i.e. increased scattering cross-section (Eq. 12). In shallow waters, there is a severe reduction in interface backscatter with an increase in gas content. This is due to the decrease of sediment sound speed in the presence of gas below resonance (Anderson et al., 1998, Wilkens and Richardson, 1998). The volume backscatter contribution in shallow water increases with increased gas content but much less than the increases found in deep water, a result of the higher attenuation from the bubbles at lower

34

ambient pressure (Fig. 1.2, bottom row). Thus, in shallow water, the gain in volume contribution is sometimes not enough to compensate for the loss in interface backscatter, yielding a net decrease in the total backscatter response.

An exercise similar to the one shown in Fig. 1.2 can be done to verify the frequency dependence of the total backscatter from gassy sediments. In general, scattering at lower frequencies has higher volume contributions in gassy sediments, mainly due to lower attenuation. The interface contribution to scattering from gassy sediments is relatively low at lower frequencies.

Another interesting exercise is to calculate the model response for the range of seafloor roughness expected to be found in sediments of the Eel River Margin, that is ω_2 from 0.00050 cm^4 to 0.00200 cm^4, and λ equal to 3.25 (Anonymous, 1994). The result of this modeling shows that the backscatter response for grazing angles from 30^0 to 60^0 of gassy sediments has a maximum increase of 1.2dB when the seafloor roughness is changed from the minimum to the maximum value. On the other hand, the roughness parameters show a strong influence in the backscatter response in the angular sector next to nadir, i.e. grazing angles from 60^0 to 90^0. Thus, the backscatter angular response of gassy sediments in the angular sector from 30^0 to 60^0 is less affected by seafloor roughness, and appears to be controlled by volume contribution.

35
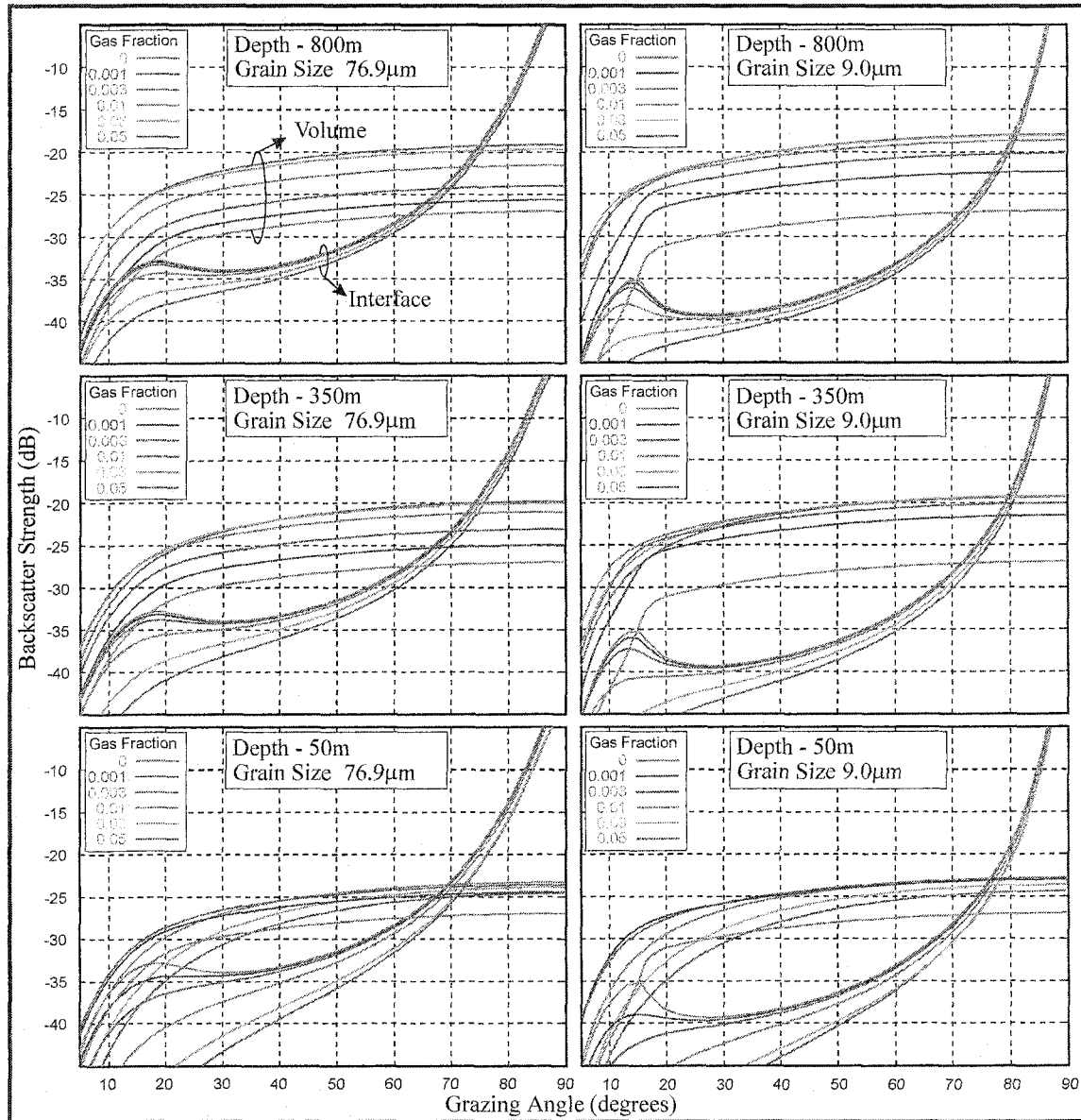
Figure 1.2- Simulation of model results for two different grain-sizes (columns) and three different depths (rows). The model response is calculated for various gas fractions ranging from 0 to 0.05 (5%). Model parameters for grain size 76.9μm are: $v=1.061$, $\rho=1.757$, $\delta=0.0193$, $w_2=0.00136$ cm^4, $\gamma=3.25$, $\sigma_2=0.001$; and for grain size 9.0μm are: $v=1.039$, $\rho=1.664$, $\delta=0.00272$, $w_2=0.00052$ cm^4, $\gamma=3.25$, $\sigma_2=0.001$.

36

1.5 A Test on the Eel River Margin

As a general test of the ideas outlined above we used multibeam sonar and core data collected from the Eel River margin offshore northern California, a region known to be rich in gassy sediments. The offshore Eel River Basin is located on the eastern border of the North American Plate, from Cape Mendocino extending 200km northwards to Cape Sebastian, Oregon (Field et al. 1980). The eastern boundary of the basin is the coastline and the western boundary is the continental slope, which coincides with the crustal plate boundary with the Juan de Fuca Plate.

This margin was the focus of a multi-disciplinary, five-year ONR sponsored study of the processes responsible for generating the preserved stratigraphic record (STRATAFORM; Nittrouer, 1998). In the course of this study, an immense database of marine information has been collected (Mayer et al. 1999), including two different sets of multibeam sonar bottom backscatter collected at 30kHz and 95kHz, and numerous core sampling sites with measurements of sediment physical properties and free gas content (Fig. 1.3).

37
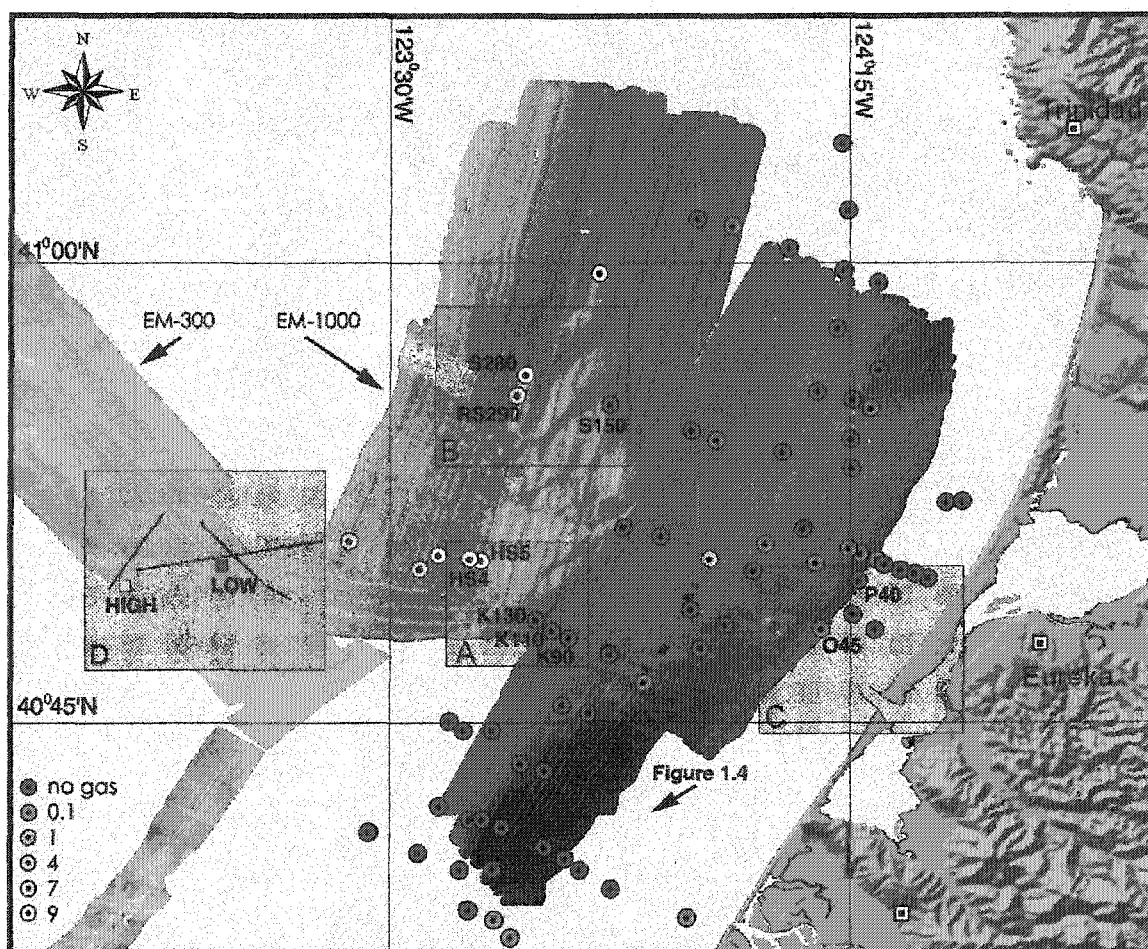
Figure 1.3- Location map showing acoustic backscatter mosaics on the Eel River Margin from two multibeam surveys: EM1000 at 95kHz (the mosaic closer to the coast), and EM300 at 30kHz (the mosaic in deeper waters). High backscatter is displayed in lighter shades of gray; low backscatter in darker tones. The brightness of the symbols is related to the amount of free gas in the sediment, as measured in core samples. The reference boxes demarcate the zoom areas for examples A, B, C and D.

The multibeam sonar data was collected with a Simrad EM1000, 95 kHz. multibeam sonar installed aboard the Humboldt State University research vessel *Pacific Hunter*. The EM1000 forms 60 roll stabilized 3.3°x2.5° beams over a swath width of 150 degrees in water depths up to 200m. In deeper water, 48 beams are produced over a swath width of 120 degrees to about 600m depth and 60 degrees beyond 600m. In addition to the bathymetric data, the EM1000 also provides raw measurements of the bottom backscatter as a function of grazing angle for each of the beams. All acquisition parameters are recorded and thus the raw data can be corrected for the removal of the time-varying gains, such as source level, receiver sensitivity; and angle-varying gains. Given that the detailed bathymetry is known from the multibeam time-of-flight measurements, true grazing angles with respect to a bathymetric model can be calculated as well as corrections for footprint size and residual beam pattern (Fonseca, 2001). Applying these corrections, the EM1000 backscatter data from the Eel River margin was converted to true scattering strength for comparison with the results of the proposed model.

Interpreted much like sidescan sonar imagery (except with angular resolution), the backscatter mosaic of the Eel River margin reveals several interesting spatial patterns (Fig 1.3). A zone of extremely high backscatter (bright areas in Fig 1.3) is found in the middle of the western (deep) edge of the survey area. The high backscatter in this region has

39

been correlated with the outcrop of a large structural feature (a breached anticline) and blocky crusts of authigenic carbonate related to methane expulsion (Orange, 1999b, Yun et al., 1999). The high-backscatter streaks in the middle of the survey area are thought to be associated with grain size changes and the outcrop of indurated sediment (Goff et al, 1999). More intriguing is the general trend of high backscatter in the deep water and low backscatter in shallow water, a relationship which is counter-intuitive when the general trend of grain size (decreasing from shallow water to deep water) is considered. This enigma was noted by Goff et al., 1999 and Borgeld et al., 1999 who suggest several possible mechanisms (increased surface roughness in finer grained sediments, increased penetration and contribution of subsurface layering in finer-grained sediments) for this anomalous relationship. The complex relationship amongst gas content, water depth and grain size described in the model presented here, may offer another possible explanation.

1.5.1 Evidence for Gas in the Shallow Sediments of the Eel River Margin

The Eel River Basin is a tertiary forearc basin with conditions ideal for the generation and movement of both thermogenic and biogenic gas. Deep seated source beds combined with differential sediment loading and a large amount of tectonic activity have resulted in overpressured zones and the migration of gas from deep layers to the surface and near-

40

surface (Yun et al., 1999). In addition to the deep sources of gas, extremely high modern sedimentation rates and large quantities of organic material supplied by numerous floods provide an excellent source of biogenic gas (Sommerfield and Nittrouer, 1999). Numerous lines of evidence support the ubiquitous presence of both thermogenic and biogenic gas in the sediments of the Eel River margin. These include: 1- observation of gas plumes in the water column (Yun et al., 1999); 2- direct measurements on cores (Kvenvolden and Field (1981) and this study (Orange, personal communication); 3- seismic evidence (wipeout zones and other acoustic anomalies), at a range of frequencies from low frequency multichannel seismic to high frequency boomers, chirp sonars and 3.5 kHz profilers (Field and Kvenvolden, 1987,Yun et al., 1999); 4-the presence of authigenic carbonates (Orange, 1999b) and near-surface hydrates (Field and Kvenvolden, 1985); 5-towed electromagnetic surveys (Evans, et al., 1999), 6- surface structures associated with gas (pockmarks and sediment failure features); and; 7- commercial gas fields onshore with expected recovery of over 3.34 km^3 of natural gas (Parker, 1987).

While there is overwhelming evidence for the presence of gas in the sediments of the Eel River margin, the more pertinent question, with respect to testing the model proposed here, is whether there is evidence for gas in the upper few decimeters of the sediment column. Given the 95 kHz frequency of the multibeam sonar used to survey the area, we

41

would expect that penetration into, and interaction with, the subsurface would be limited to the upper few decimeters (to perhaps one meter depending on sediment type and grazing angle). The near-surface distribution of gas is more difficult to quantify. Anderson et al. (1999) in their study of Eckernforde Bay noted that the gas bubbles they were able to measure (those greater than 0.42 mm equivalent spherical radius) were not present in the upper few decimeters of the sediment column due to sulfate reduction. They do, however, report that cores recovered from another bay (Medklenburg Bay) did show small gas bubbles in the upper 2 cm of the sediment column and that frequency dependent reflectivity data from Eckernforde Bay implied the presence of very small bubbles in the upper few cm's of the seafloor.

Several lines of evidence (both indirect and direct) imply that gas may be present in the upper few decimeters of the sediments of the Eel River margin. Unlike Eckernforde Bay which is a semi-enclosed fjord-like bay with bottom waters that often experience hypoxia and occasionally anoxia and whose gas source is strictly biogenic (Richardson and Davis, 1999), the Eel River basin is an open ocean continental margin environment with well mixed water masses and both thermogenic and biogenic sources of gas. High-resolution 3.5 kHz, boomer and chirp sonar data all show regions of "wipeout zones" (acoustic turbidity), some of which extend to the surface and even into the water column (Field and Kvenvolden, 1981, Yun et al, 1999, and Fig 1.4). In addition reduced

42

halos and mats of the sulfate oxidizing bacterium *Beggiatoa sp* have been seen on the seafloor in areas of the Eel River margin (Orange, 1999b) indicating the slow seepage of methane to the seafloor. Further evidence for near-surface gas is provided by Evans et al. (1999) who made resistivity measurements using a towed electromagnetic sensor and interpreted low apparent porosities to indicate the presence of gas in the upper few meters of the sediment column, particularly in the shallow water regions of the Eel River margin, which showed anomalously low backscatter.

Direct evidence of the presence of shallow gas in the Eel River margin comes from the analysis of gas content in shallow cores. Kvenvolden and Field (1981) analyzed 1 to 2 m long gravity cores from a diapiric structure in the deeper waters of the Eel River basin (400 – 500m) and found high concentrations of methane (both biogenic and thermogenic) throughout the cores including samples from depths as shallow as 6 – 14 cm below the seafloor. As part of the STRATAFORM project, hundreds of cores were collected in the Eel River basin with some showing visual evidence of gas (Borgeld et al, 1999); a small number of these cores were analyzed for gas content. A subset of those analyzed, representing multiple samples from areas of differing backscatter, depth, and gas content are used here to test the proposed model. The areas and core-sites selected are shown in Fig. 3.

43
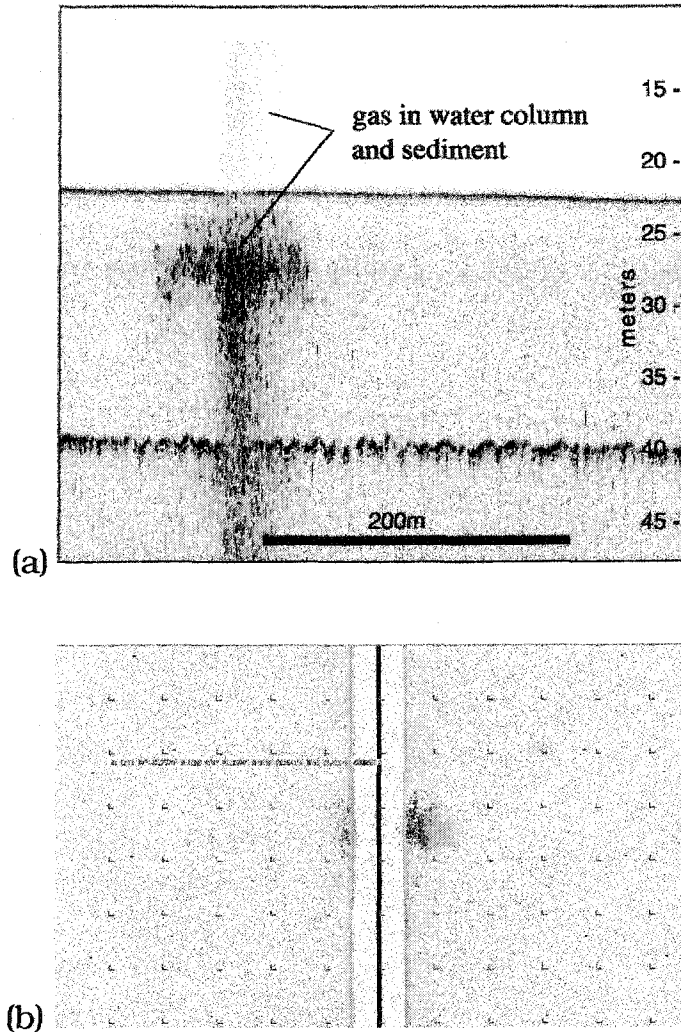
Figure 1.4- Evidences that gas may be present in shallow sediments of the Eel River margin: a) High-resolution 3.5 kHz chirp profile, showing a region of acoustic turbidity, which extends to the surface and into the water column; b) Same area surveyed by a 100kHz sidescan sonar. See Fig. 3 for location. Source: Neal Driscoll.

The core data presented here were collected by Dan Orange on the University of Washington research vessel Thomas Thompson (Cruise TN096) in 1999. During this leg, several types of cores were collected

44

including Vibracores, piston cores and box cores; core lengths ranged from more than 5 m to less than 25 cm. Analysis of gas content followed the procedure of Kvenvolden and Redden (1980) whereby sediment is taken immediately after core recovery from an approximately 10 cm interval of the core (typically about 10 cm above its base). The sediment is extruded from the core liner into a 0.95l can with two septa-covered holes on the top. Sodium azide is added to the sample and the water level adjusted until a 100ml-headspace remains. The samples are then sealed and frozen for later analysis in the lab. In the laboratory, the samples are thawed and shaken for 10 minutes and the headspace sampled by syringe for hydrocarbon gases. Analyses were performed on an HP gas chromatograph with both flame ionization and thermal conductivity detectors.

It must be noted that while these analyses are indicative of the presence, absence and perhaps relative abundance of gas at a sample location, they do not provide an accurate measure of the *in situ* abundance of free gas in the sample, and in particular, in the upper decimeters of the seafloor. Thus, while we report the measured value in Table 1, we will use these values only as indicators of the relative gas content of the seafloor sediments. In addition to the gas content, the mean grain size, sound speed and saturated bulk density of the sediment were also measured on the core samples. These data are presented in Table I and are used as inputs into the model presented above. There

45

are no available measurements for the sediment roughness and compressional wave attenuation for the studied sites. For these values, a parameterization in terms of the bulk grain size was used following the method described in the APL-UW High-Frequency Ocean Environment Acoustic Models Handbook (Anonymous, 1994).

Core	Grain-Size (µm)	Sound Speed (m/s)	Density (kg/m³)	Water Depth (m)	Gas Fraction	Gas Content	Site
HS4	9.0	1552	1786	318	0.0954	V. High	A
HS5	9.0	1553	1809	320	0.0951	V. High	A
K130	9.0	1543	1701	125	0.0	None	A
K110	16.7	1544	1696	114	0.0	None	A
K90	16.7	1545	1690	104	0.0	None	A
S280	9.6	1583	1800	258	0.075	High	B
RS290	9.6	1583	1800	267	0.067	High	B
S150	13.6	1567	1794	151	0.0	None	B
O45	76.9	1575	1796	39	0.01	Low	C
P40	125.0	1560	1784	40	0.0	None	C
High	4.8	1530	1680	607	n.a.	n.a	D
Low	3.9	1522	1651	670	n.a.	n.a	D

TABLE I – Physical properties measured at selected core sites.

While would be better to have the grain full size distribution in order to explain backscattering differences due to physical properties,

46

only the mean grain size was available for the core sites. The parameter σ_2 cannot be directly measured, and one average value (0.01) was used (Anonymous, 1994). This assumption can lead to an overestimate of the effect of gas bubbles, since σ_2 is a measurement of sediment heterogeneities other than gas. Fortunately the effect scattering contribution of gas bubbles is normally many times higher than the contribution of other scatterers, making the use of a constant σ_2 an acceptable assumption. Another factor that would increase the volume contribution is the presence of multiple scattering (Jackson et al, 1998). Table II shows values of physical parameters that are common for all four examples. The model was run for each core site using the parameters presented in Tables I and II; these results as well as comparisons to the measured multibeam sonar backscatter in the area will be discussed in the next section.

1.5.2 Area A (Humboldt Slide) mid-depth range

Area A (Fig. 1.3) encompasses five core locations, which have variable gas fractions and associated backscatter. Cores HS-4 and HS-5 have high gas fractions: 0.0951 and 0.0980 respectively. The average depth for these two cores is 330m. Cores K90, K110 and K130, on the other hand, have no measured gas; their average depth is 114m. Backscatter images from a SIS-1000 deep-towed sidescan sonar reveal a dense distribution of pockmarks through this area (the Humboldt Slide

47

zone), providing evidence for widespread, but focused gas and fluid venting (Gardner et al, 1999). Figure 1.5 shows the backscattering strength measured at these core sites by the EM1000 multibeam sonar. The displayed curves are an average of 50 sonar pings around the core sites, which represents in average a linear distance of 100m. There is a 5dB difference in the backscatter response (average backscatter for grazing angles from 30^0 to 60^0) between sites with and without measured gas. This difference cannot be explained by the differences in physical properties measured at these 5 core sites (Tables I and II).

Seawater density	ρ_w	1022 kg/m^3
Seawater sound speed	c_w	1485 m/s
Gas density	ρ_g	1.24 kg/m^3
Gas ratio of specific heats	γ	1.403
Gas specific heat at constant pressure	s_p	240 cal/kg
Gas thermal conductivity	C_g	5.6x10^{-3} cal/ (m s ^{o}C)
Muddy sediment viscosity	μ	1.0x10^{-3} kg/(m s)
Ambient Hydrostatic Pressure	P_0	(1.0135x10^5+9.80665*ρ_w*depth) N/m^2

TABLE II – Values of common parameters used to evaluate the model at selected core sites.

48

The backscatter angular response can be calculated using sediment properties measured at the core sites (Table I). The parameters used as input for the model are: $v=1.039$, $\rho=1.664$, $\delta=0.00272$, $w_2=0.00052$ cm^4, $\gamma=3.25$, $\sigma_2=0.0010$, with no gas. The result is shown in Fig. 1.6 for the interface backscatter and the total (volume + interface) backscatter. The model was then run a second time, including the very-high gas fraction of 0.098, which changed the following model parameters: $v=0.939$, $\rho=1.571$, $\delta=0.0695$, and generated an equivalent volume contribution of $\sigma_2=0.0068$ (including contributions from gas and other heterogeneities). Note that the model shows about 6dB difference (average backscatter for grazing angles from 30^0 to 60^0) between sites with high gas content and those with no measured gas, which is similar to what is shown in Fig. 1.5. The difference in absolute values between data and model (Fig. 1.5 and Fig. 1.6) is small, which may be explained by calibration problems in multibeam sonar systems. There was a small reduction of interface backscatter due to the low sound speed ratio of the gassy sediment. The volume backscatter of the gassy sediment is considerably higher, which results in a net increase in the backscatter response.
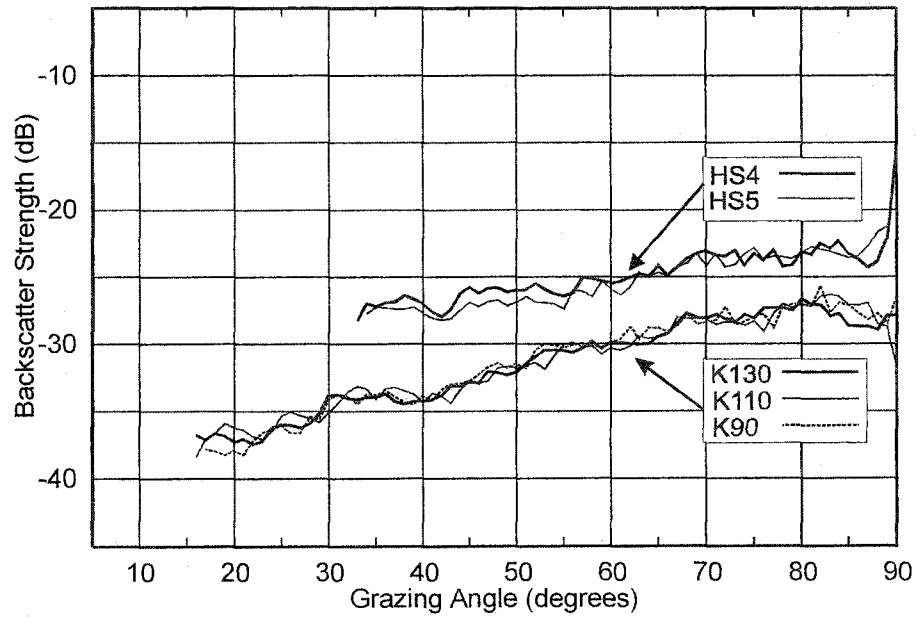
Figure 1.5- Backscattering strength measured by a Simrad EM1000 multibeam sonar (95kHz) around core sites HS4, HS5, K90, K110 and K130.
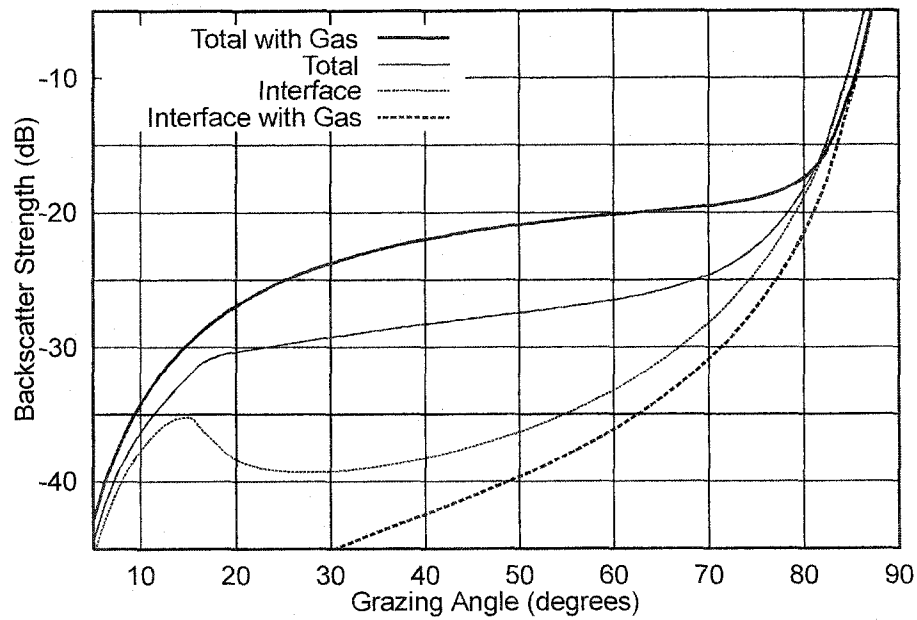

Figure 1.6- Model response using the sediment properties measured at the core sites HS4, HS5, K90, K110 and K130.

50

1.5.3 Area B (mid-depth range)

Area B (Fig. 1.3) contains cores S280 and RS290 which have moderately high gas fractions: 0.075 and 0.067 respectively. These two cores are located at an average depth of 253m. Core S150 at 151m of depth has no measured gas. The existence of near-surface gas in this area is demonstrated by acoustic anomalies on Huntec seismic profiles (Yun et al. 1999). Figure 1.7 shows the backscattering strength measured at these core sites by the EM1000 multibeam sonar. The final response is an average of 50 sonar pings around the core sites. There is an average of 4dB difference in the backscatter response between sites with and without measured gas, although the sites have basically the same sediment properties.

Figure 1.8 shows the model response using the sediment properties measured at the core sites (Table I) and the common values in Table II. The parameters used as input for the model are: $\nu=1.0552$, $\rho=1.755$, $\delta=0.00290$, $w_2=0.00052$ cm^4, $\gamma=3.25$, $\sigma_2=0.001$, with no gas. The model was run a second time including the moderately high gas fraction of 0.075, which changed the following model parameters: $\nu=0.972$, $\rho=1.683$, $\delta=0.0532$, and generated an equivalent volume contribution of $\sigma_2=0.0055$ (including contributions from gas and other heterogeneities). Note that the model predicts a 4dB increase in backscatter strength when gas is included and that this is consistent

51

with the difference seen in the measured backscatter between gassy (RS280 and S280) and non-gassy (S150) sites (Fig. 1.7). At these depths (336m for Area A and 252m for Area B) the presence of gas has the effect of slightly lowering the interface backscattering component and significantly increasing the volume backscattering component.

Figure 1.7- Backscattering strength measured by a Simrad EM1000 multibeam sonar (95kHz) around core sites RS280, S280 and S150.
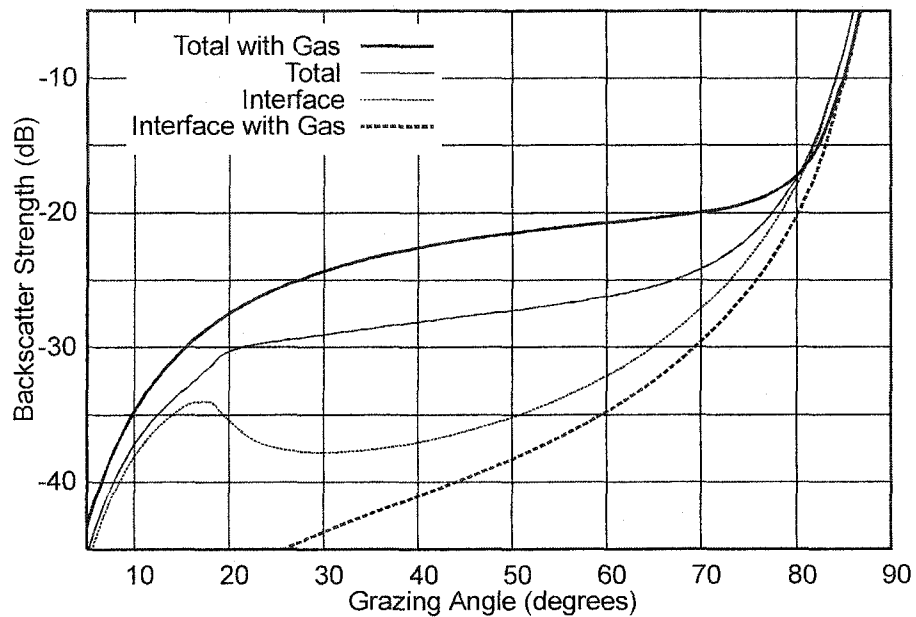
Figure 1.8- Model response using the sediment properties measured at the core sites RS280, S280 and S150.

1.5.4 Area C (shallow water)

Area C (Fig. 1.3) contains two core locations in relatively shallow water (39m). Core O45 had a measured gas fraction of 0.010, while core P40 had no measured gas. These two cores are also inside the zone of acoustic turbidity, interpreted from high-frequency seismic profiles, to be caused by the presence of gas (Yun et al. 1999). Figure 1.9 shows the backscattering strength measured at these two core sites by the Simrad EM1000 multibeam sonar. There is almost no difference at the backscatter strength between the sites.
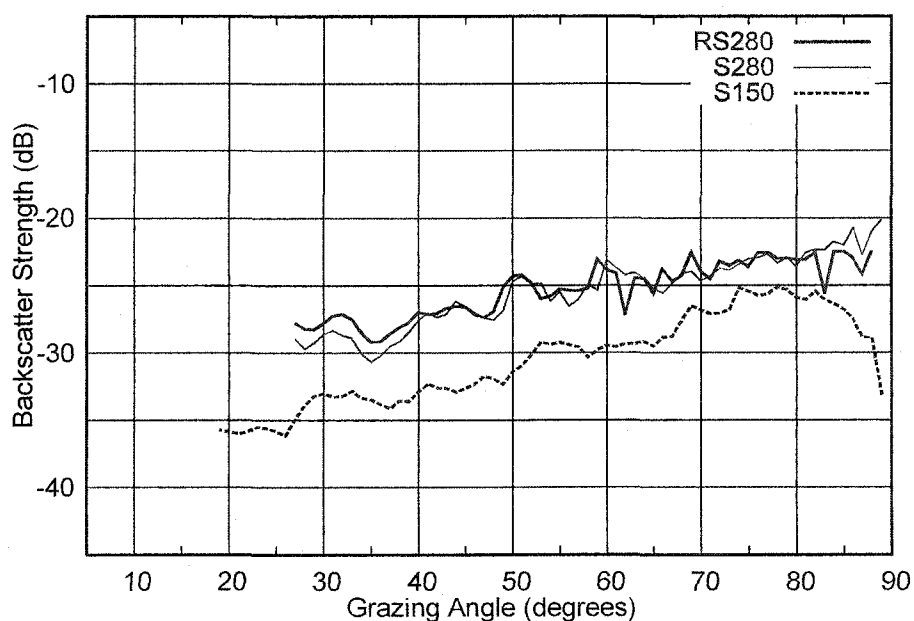
53
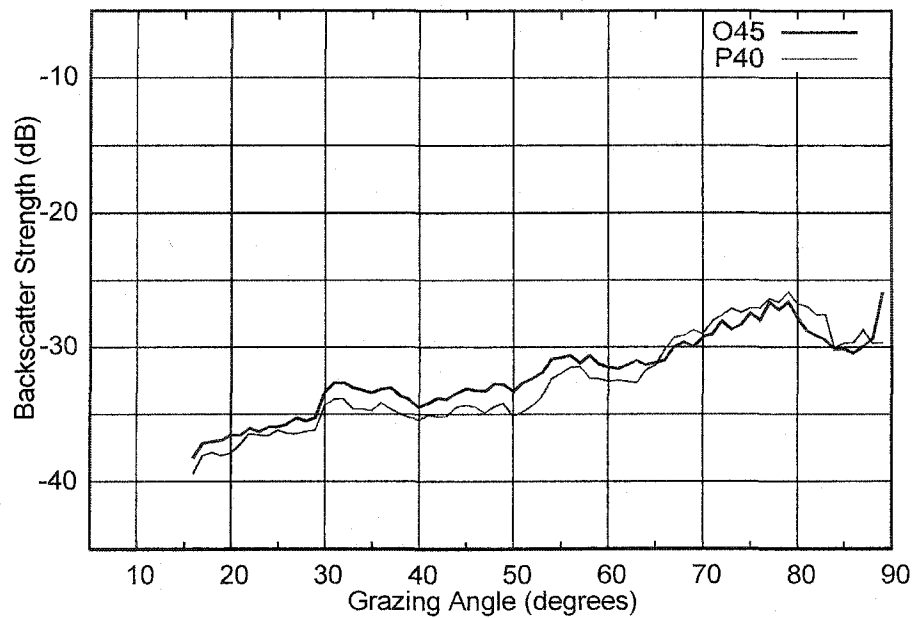
Figure 1.9- Backscattering strength measured by a Simrad EM1000 multibeam sonar (95kHz) around core sites 045 and P40.

The model response is calculated using the sediment properties measured at the core sites and common values of Table II. The parameters used as input for the model are: $\nu=1.061$, $\rho=1.757$, $\delta=0.01972$, $w_2=0.00120$ cm^4, $\gamma=3.25$, $\sigma_2=0.0010$, with no gas. The model was run a second time including the low gas fraction of 0.01, which changed the following model parameters: $\nu=0.891$, $\rho=1.747$, $\delta=0.0768$, and generated an equivalent volume contribution of $\sigma_2=0.0011$ (including contributions from gas and other heterogeneities). When gas is added, the model predicts a very small difference between the two sites (Fig. 1.10). In shallow water (39m) there is a severe reduction of interface backscatter due to the very low sound speed ratio of the gassy sediment.

54

The increase in volume backscatter of the gassy sediment is not high enough to compensate for the interface backscatter reduction. This relatively small volume scatter is a consequence of the higher attenuation of gassy sediment in shallow water. In shallow water, the ambient pressure is lower which increases the attenuation in the gassy sediment, according to Eq. (9).
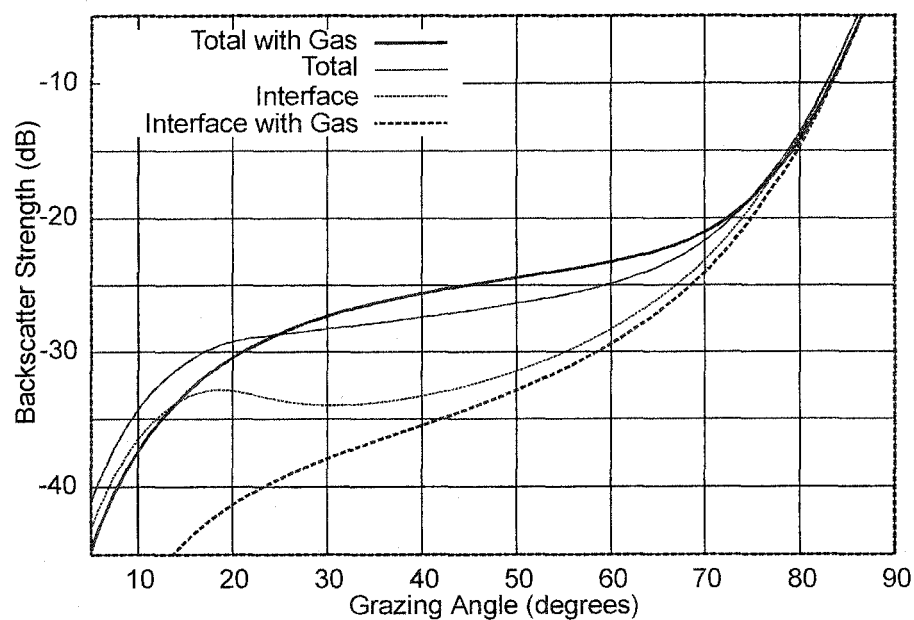
Figure 1.10- Model response using the sediment properties measured at the core sites O45 and P40.

1.5.5 Deep-water high backscattering

Detail D of the location map (Fig. 1.3) shows an area surveyed by both EM1000 (95kHz) and EM300 (30kHz) sonars in relatively deeper water: 785m. The overlaid vectors are navigation tracklines of the

55

EM1000 survey over the backscatter mosaic of the EM300. The two boxes are selected areas of low and high backscattering strength. The high backscatter area was selected near the edges of the Table Bluff anticline, where many acoustic bright spots were observed on low-frequency multichannel seismic profiles (Orange, 1999). Figure 1.11 shows the backscattering strength measured at the two selected areas by both EM1000 and EM300 multibeam sonars. The displayed curves are an average of 50 sonar pings around the selected sites. Comparing the two sites, we observe a 4dB difference at the backscatter strength at 95kHz and a 7dB difference at 30kHz.

Figure 1.11- Backscattering strength measured at the two selected areas by both EM1000 and EM300 multibeam sonars at two selected areas.

Figure 1.12a shows the model response at 95kHz using the sediment properties measured by core analysis near the selected areas. Figure 1.12b shows the model response at 30kH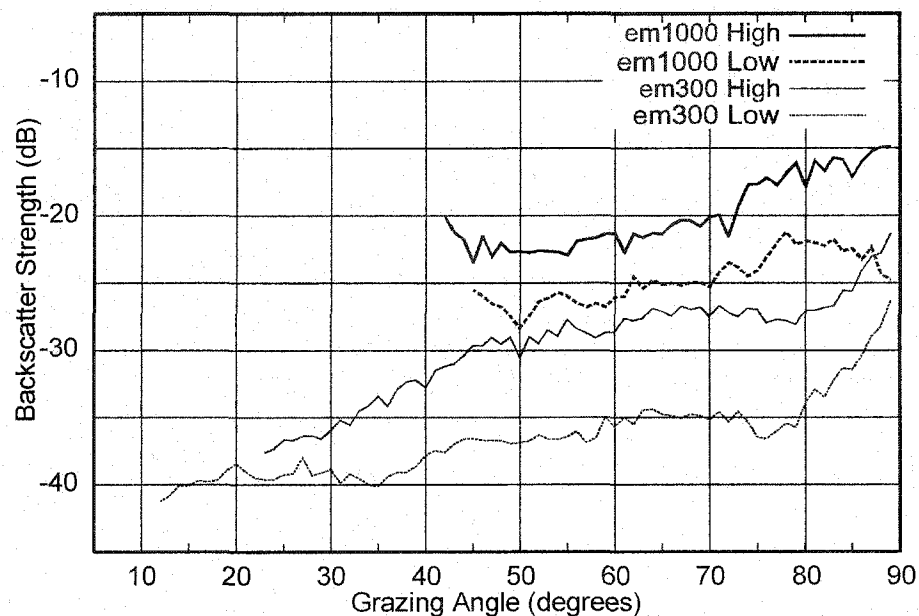z using these same sediment properties. Core sites around the selected areas were not analyzed for the content of free gas. The parameters used as input for the model are: $\nu=1.0303$, $\rho=1.644$, $\delta=0.00183$, $w_2=0.00052$ cm^4, $\gamma=3.25$, $\sigma_2=0.001$. The model was run again at 30kHz and 95kH with a very low gas fraction of 0.001, which changed the following model parameters at 95kHz: $\nu=1.030$, $\rho=1.643$, $\delta=0.0031$ and equivalent $\sigma_2=0.0041$; and at 30kHz: $\nu=1.030$, $\rho=1.644$, $\delta=0.0026$ and equivalent $\sigma_2=0.0051$. This very low gas fraction can explain part of the backscatter difference of Fig. 1.11. Note that in choosing this gas fraction, the model predicts a 4dB difference between the two sites at 95kHz and 5dB difference at 30kHz. The model and data values from Fig. 1.11 (EM1000) and Fig. 1.12a agree for almost all grazing angles, except for near nadir, where the EM1000 multibeam sonar has problems with absolute gain tracking. The model and data values from Fig. 1.11 (EM300) and Fig. 1.12b show large offset, which can be explained by calibration problems during the survey with the EM300 multibeam sonar. In deep water, there is a smaller change in the interface backscatter of the gassy sediment. This is caused by the higher ambient pressure, which reduces the effect of bubbles on the sediment sound speed. On the other hand, a very small gas quantity in deep water produces a very high volume backscatter response. The lower

57

frequency (30kHz) results in a lower interface backscatter and a higher volume scatter, due to a lower value for the attenuation term in Eq. (9).
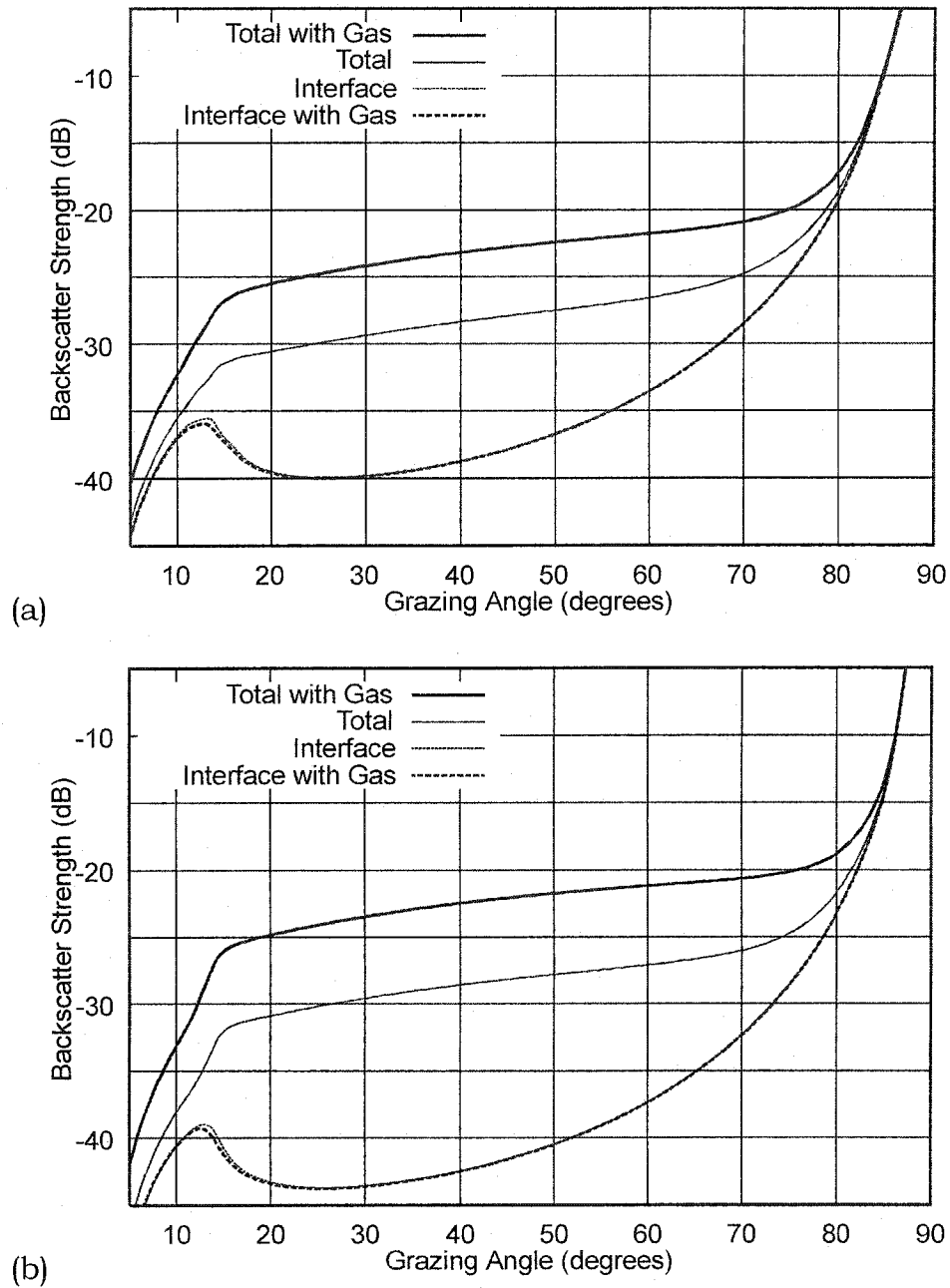

(a)

(b)

Figure 1.12- a) Model response at 95kHz using the sediment properties measured at the selected areas b) Model response at 30kHz using the sediment properties measured at the selected areas.

58

1.6 Conclusions

Gas is an important and common sediment heterogeneity on continental margins which may explain some of the backscatter-response anomalies seen in the sediments on the Eel River Margin. A model has been proposed that shows that gas affects both the interface and volume contribution of the backscatter angular response. Gas normally increases the volume contribution and weakens the interface contribution, but the relationship is complicated by changes in depth and sediment properties. The backscatter response of fine-grained gassy sediments (grain size<10μm) is basically controlled by the volume contribution to backscattering. Coarser sediments (grain size>60μm) present both significant changes in volume and interface backscatter in the presence of gas.

The model was tested by inputting physical properties measured on cores collected in a region also surveyed with a 95 kHz multibeam sonar. The cores selected for input into the model were cores that had also been analyzed for gas content and these values were used to estimate the relative abundance of gas at the core sites. While the head-space analyses used for determining gas content are not necessarily an accurate representation of the *in situ* concentration of free gas in the cores, they are indicative of the presence, absence and, perhaps relative abundance of gas in the upper few meters of the seafloor. Both the gas

measurements and the multibeam backscatter showed a high degree of lateral variability.

Raw time series of the 95 kHz multibeam sonar backscatter as a function of angle of incidence were corrected for source and receiver gain changes, area of insonification, true grazing angle and residual beam patterns resulting in a georeferenced record of true scattering strength. The measured backscatter (averaged over about 100m around each core site) was then compared to the model output for each core site and for a range of gas contents. The measured results were generally in agreement with the model and with the results predicted for the measured gas contents.

Depth plays an important role in the backscatter response of gassy sediments. In deep water (deeper than 400m), the predicted interface backscatter is only slightly affected by the presence of gas, a consequence of the higher bubble stiffness at higher ambient pressure. On the other hand, a small amount of gas yields a very-high predicted volume contribution in deep water. In shallow water (less than 100m), the predicted interface backscatter is severely reduced when the sediment is charged with free gas, due to the decrease of sediment sound speed. The predicted volume contribution in shallow water is lower, due to higher attenuation from the bubbles at lower ambient pressure. In shallow water, the gain in volume contribution is sometimes not enough

to compensate for the loss in interface backscatter, resulting in a net decrease in the total backscatter response.

While the results presented here are encouraging in terms of the potential for using multibeam sonar as a qualitative and quantitative indicator of the gas content of near-surface sediments, much more work needs to be done. In particular, the model needs to be tested under controlled conditions where near-surface sediment samples can be collected and maintained under *in situ* conditions (as described in Anderson et al. 1999). New developments in pressure maintaining core barrels (e.g. Pettigrew, 1992) should greatly aid in this effort. In addition, the models need to be extended to include the effect of multiple scattering, which should provide a more accurate prediction of the total scattering due to gas bubbles.

61

CHAPTER II

ARCVIEW OBJECTS IN THE FLEDERMAUS INTERACTIVE 3-D

VISUALIZATION SYSTEM:

AN EXAMPLE FROM THE STRATAFORM GIS

2.1 Abstract

Over the past twenty years, the production of, and demand for marine geospatial data has increased considerably. This has been the direct result of advances in acoustic remote sensing technology, marine positioning and orientation techniques. These new technologies when used in concert with other traditional sources of marine information generate enormous amounts of data and present great challenges for management, analysis and interpretation. This was the problem faced during the integration of a complex marine database collected off Northern California for the ONR-sponsored STATAFORM project. In the course of this study more than 40 investigators collected a wide range of data aimed at understanding the processes defining continental margin stratigraphy. These data sets were organized into an ARCVIEW database with more than 58 layers and a number of specially developed extensions.

While the ArcView GIS offered an initial approach to the integration of this large marine database, the 2-D map paradigm of a traditional GIS was insufficient for the analysis of the complex relationship amongst the data layers.

We thus extended our analyses through the incorporation of an interactive 3-D visualization system (Fledermaus). A software filter that translates files from the ArcView database to a Fledermaus internal format was developed. The STRATAFORM database was explored in this 3-D visualization system, revealing a number of new insights.

2.2 Introduction

Over the past twenty years, the demand for marine geospatial data has increased considerably. This demand comes as a result of concurrent advances in acoustic remote sensing technology and marine positioning and vessel orientation techniques, which have revolutionized our ability to map the seafloor (Mayer et al., 2000). These data sets go far beyond traditional sparsely spaced bathymetric measurements, often including very dense multibeam sonar coverage, acoustic imagery and many other types of data (sub-bottom profilers, laser airborne depth sounders, laser line scanners, etc.). With these new sources of data it is now feasible to produce much more realistic depictions of the morphology of the seafloor and, as our interpretative and analytical abilities improve, perhaps even thematic information about seafloor

63

character. This technology provides critically needed information for thematic and cartographic mapping applied to natural resource management and exploitation, fisheries habitat studies, environmental monitoring, underwater engineering, geological exploration and safety of navigation. These new sources of seafloor data in concert with more traditional sources of marine information produce enormous amounts of data, presenting tremendous challenges for management, analysis and interpretation. These challenges and the demands associated with them are analogous to those that faced the terrestrial remote sensing community during the 1970's.

Geographical Information Systems (GIS) have become the default solution for the integration of large multivariate data sets in almost all terrestrial spatial applications (Aronoff, 1991). We now have the same challenge in the marine environment where the GIS tool, with some minor adaptations, can provide a means of integrating large amounts of information dispersed in a variety of media and formats. A GIS approach for underwater applications will offer a straightforward path for visualizing, interpreting and analysing vast amounts of data, facilitating numerical and logical queries on the database providing an intuitive means to depict the complex inter-relationships amongst the various data layers.

2.3 The Map Paradigm

By definition, a Geographical Information System is a computer tool used to collect, store, retrieve, transform, and display spatial data (Burrough and McDonnell, 1998). The term geographical refers to a known cartographic position of the data (the latitude and the longitude or projection co-ordinates), and the term information refers to attributes assigned to that cartographic location. Consequently, the elemental organization of the GIS database is highly linked to a two-dimensional (2-D) positioning array, which is suitable for a map representation (Bonham-Carter, 1996). Following this rationale, the majority of GIS's are constrained to two-dimensional data analysis and deal most efficiently with 2-D datasets.

Despite this focus on 2-D datasets, most GIS systems also handle digital elevation models (DEM's), which are representations of continuous surfaces used for topographic, bathymetric, geophysical and any other data sets that can be described by an array of numbers. Most GIS's can present perspective views of the DEM. This is referred to by some authors as $2^{1/2}$-D, as it is more than a flat 2-D representation, but it lacks the formal implementation of a full 3-D setting.

2.4 Marine Applications

Although the GIS environment offers an initial solution to many of the problems of data integration, the marine environment poses some

65

unique problems. First, we need a system that can take full advantage of, and draw useful inferences from the especially dense datasets produced by acoustic surveys. Multibeam sonar in shallow water surveys can easily produce tens of million soundings (depth measurements) per hour. This enormous data rate presents a challenge to data processing, management and quality assurance, and imposes special needs for data visualization (Mayer et al., 2000).

Another specific requirement of the marine environment is the need to depict information in the water column. Parameters such as temperature, salinity, and sound velocity are measured as a function of depth in different locations, presenting an example of a data cube in a 3-D space. Some new multibeam sonars can detect fish schools and other acoustic targets in the water column. This is a typical example of a 3-D object that must be visualized dynamically within a 3-D scene. The ongoing development of Remotely Operated Vehicles (ROV) and Autonomous Underwater Vehicles (AUV) provides a new source of acoustic, photographic, biological, physical and oceanographic measurements that must be referenced to 3-D coordinate frame. These vehicles move freely in the water columns, acquiring data in all directions.

Engineering projects such as offshore platform building, pipeline laying and submarine communication cables need a precise description of the bathymetry, location of natural and man-made obstacles, and a

66

characterization of the seafloor and of the shallow sub-bottom. Engineering decisions will be made based on the complex integration of all the information available in a 3 dimensional model (Paton, 1997). This is a classical case of a network analysis problem that can be addressed in a GIS. The spatial distribution of seafloor relief, terrain derivatives, and estimates of bottom composition are also considered important physical variables governing the distribution of seafloor fish habitats (Martinez, 1999). Spatial modeling of these properties in a 3-D environment is a promising method of identifying suitable bottom habitats. Finally, of particular interest is the real-time three-dimensional visualization of bathymetric data collected for safety of navigation. Real-time visualization can serve as a means of providing tools for quality control as well as the potential of designing 3-D electronic charts that provide an intuitive perspective of the relationship of a vessel to navigation hazards.

2.5 Towards a 3-D GIS

Given the spatial and temporal variability of marine data, the 2-D map concept of the traditional GIS may no longer be suitable for many marine problems. 3-D visualization, on the other hand, permits the very rapid examination and verification of large data sets. During the 3D visualization process, acquisition problems such as data blunders or system artifacts will become evident. In the same way, complex spatial relationships amongst the data components will be more easily perceived

67

(Ware, 1999). Three-dimensional visualization systems improve our capacity for data mining, as the data is presented in a more intuitive way, revealing often hidden relationships amongst the data sets (Kleiner at al., 2000).

Although 3-D visualization can undoubtedly offer tremendous advantages for data analysis, it implementation comes with a high price. Three dimensional graphical rendering and display require considerable amounts of processing which until recently was only available in specialized and expensive graphics workstations (MacCullagh, 1995). In recent years however, the hardware and software required for this processing have advanced considerably. With increases in the computing power of desktop computers combined with advances in graphics technology, 3-D graphics is now quite affordable. In concert with these hardware innovations has been the development of a number of 3-D scientific visualization software packages capable of running on a variety of platforms.

The goal for an underwater data integration system is a software/hardware solution that combines various components of digital mapping, image processing and database management on one machine at an affordable cost. The system must be referenced to a cartographic coordinate system, with all information attached to a chosen ellipsoid or other earth model. The visualization system should also be interactive and fully quantitative, allowing measurements and queries on the

68

displayed database. It should support 3-D topology for spatial analysis and search, and be attached to a database management system that deals with spatial and non-spatial data. For that we need a 3-D geographical information system that is capable of integrating different data types at different scales, from different sources, with different formats, and covering different areas. While many GIS systems are approaching these capabilities none really support them all, particularly for very large data sets. At the same time, there have been rapid advances in 3-D visualization packages but many of these systems lack the careful georeferencing and many of the database interrogative capabilities of a complete GIS system. Here we present an approach that tries to take advantage of the best of both worlds, by offering an integrated path between the ArcView GIS and the Fledermaus interactive 3-D visualization package.

2.6 The STRATAFORM Database and GIS

To demonstrate our approach we will use a complex marine database collected off Northern California during the STRATAFORM project. STRATAFORM (STRATA FORmation on the Margins) is a multi-year, multi-investigator program funded by the U.S. Office of Naval Research with the objective of understanding the geologic processes of the shelf and slope responsible for the formation of the sedimentary record over a continuum of scales (Nittrouer and Kravitz, 1996). One field area for this program is the highly sedimented, tectonically active, Eel

69

River margin off Northern California (Nittrouer, 1999). In the course of the five years of study of the Eel River Margin, an immense data base of marine information including physical oceanographic time series, multichannel seismic data, physical property data from cores, detailed bathymetry, backscatter, bottom photos, and a number of other parameters has been collected. Each of these distinct data sets provides insight into at least one component of the complex system responsible for generating the strata of the continental margin. This database is remarkable not only for its volume, but also for its diversity.

In response to the need to understand the inter-relationships amongst these data sets we sought to find a means to organize and integrate the data into a form that could be easily searched and analyzed. Additionally many investigators needed to independently work on this vast marine database. To allow this we chose to take advantage of GIS technology and create a fully georeferenced data set that can be interactively explored. Our approach was to treat each data set as an individual layer or theme and bring the data into a widely available GIS. Given that each layer is fully georeferenced and all geodetic corrections (projections, datum, etc) are applied, we would then have the ability to interactively select, explore, retrieve and display the data sets in any combinations we desire

2.7 Choosing a GIS for Data Integration

Once we decided that we wanted to bring the STRATAFORM data into a GIS (Mayer et al., 1999), we needed to select the most appropriate GIS for the task. We had a number of criteria including the ability to handle both raster and vector data. Most importantly we wanted to create a database that would be available to the rest of the STRATAFORM community (and others) and thus also wanted a system that was readily available and that allowed the exploration of databases without ownership of the GIS creation software. After evaluating a number of options, we chose ArcView from ESRI. It has an associated programming language that would allow us to customize features to our needs, it supports a number of computer environments (PC, MAC, UNIX), and it provides a freeware viewer (ArcExporer) that can be distributed with the database allowing those who do not own ArcView to still explore the data, though with some limitations.

More than 58 data layers were collected from a number of STRATAFORM and non-STRATAFORM sources. While some sort of geographic information was the common denominator of all the data sets, many of the data sets came in different formats, and were created with different map projections, geodetic datum, etc. In order integrate all of the data sets we resolved and reconciled these to a common projection/datum framework. The majority of these layers can be displayed with the conventional ArcView tools (Fig. 2.1), but certain

71

datasets required display and analysis capabilities beyond those existing in this GIS. To overcome this limitation, a series of Visual Basic programs were developed, which provided extended functionality. These included: 1) a CTD graphic program, which displays water column profiles recording information on temperature, salinity and sound velocity (Fig. 2.2); 2) a Temperature graphic program, which graphs temperature data acquired by current meters deployed for long periods; 3) a Seismic Viewer, which provides high-resolution visualization of seismic images (Fig. 2.3) and; 4) an angular response viewer, which displays the acoustic backscatter as a function of the grazing angle for any selected subset of the survey area.

After the database was assembled and functional, we started the process of data mining and analysis. During this process it became clear that to fully understand the complex interrelationships of this database we would need to explore the data in a 3-D environment (Van Driel, 1995). Most importantly, we wanted our 3-D environment to be fully interactive and able to support all of the multilayer and georeferenced aspects of the GIS. For this we chose the Fledermaus interactive 3-D visualization software package from Interactive Visualization Systems Inc.
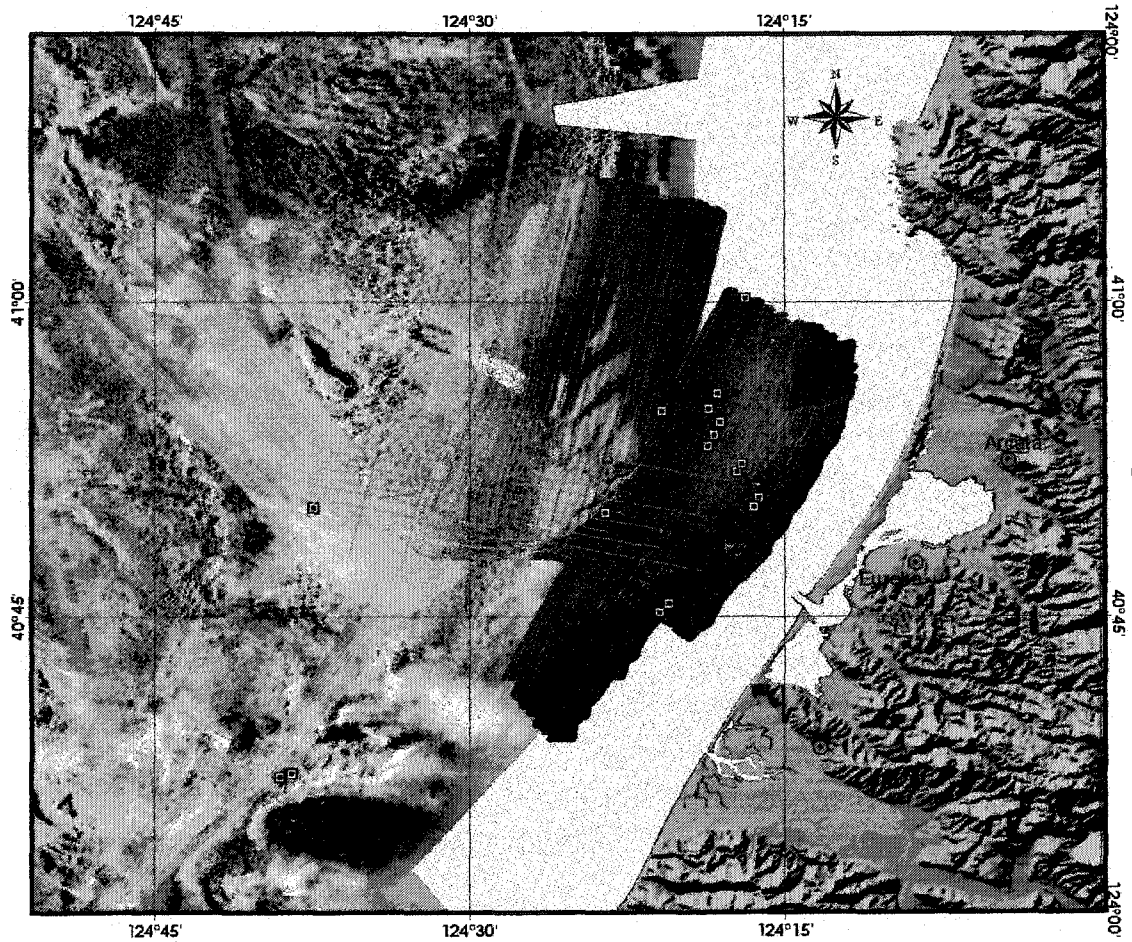
Figure 2.1- Strataform Project in ArcView Showing the following layers:
Background images: 1) Simrad EM1000 multibeam sonar backscatter, 2)
EM300 multibeam sonar backscatter 3) GLORIA sonar backscatter. 4)
Vector layer in red: tracklines from a Huntec high-resolution seismic
reflection profiler. 5) Point data in cyan: CTD water column profiles
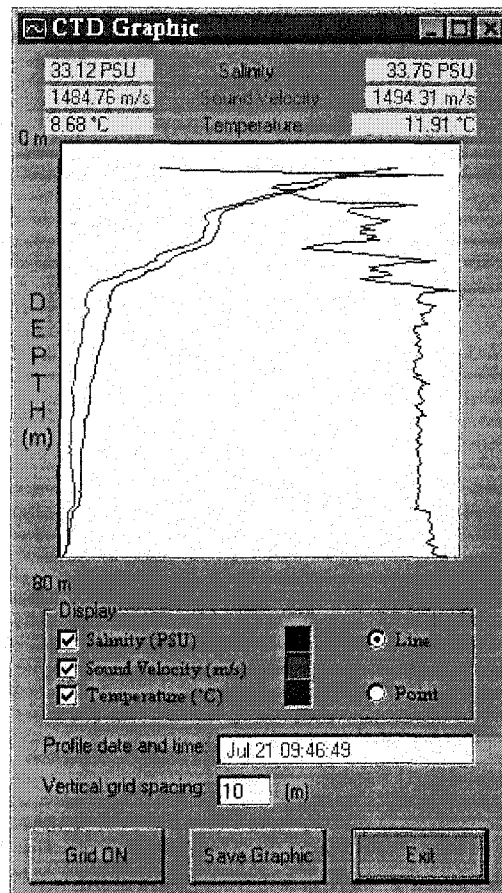recording information on temperature, salinity and sound velocity.

Figure 2.2- Graph showing CTD profiles. The plotting program is connected to the ArcView layer showed in Fig. 2.1 (symbols in cyan). This profile is from the station highlighted in yellow. Each profile can be interactively interrogated.

2.8 Fledermaus

Fledermaus is a sophisticated suite of 3-D visualization tools specifically designed to facilitate the interpretation and analysis of very large (10's to 100's of megabytes), complex, multi-component spatial data sets. The goal is to use the 3-D environment to present complex multidimensional data sets in a natural and intuitive manner that allows

74

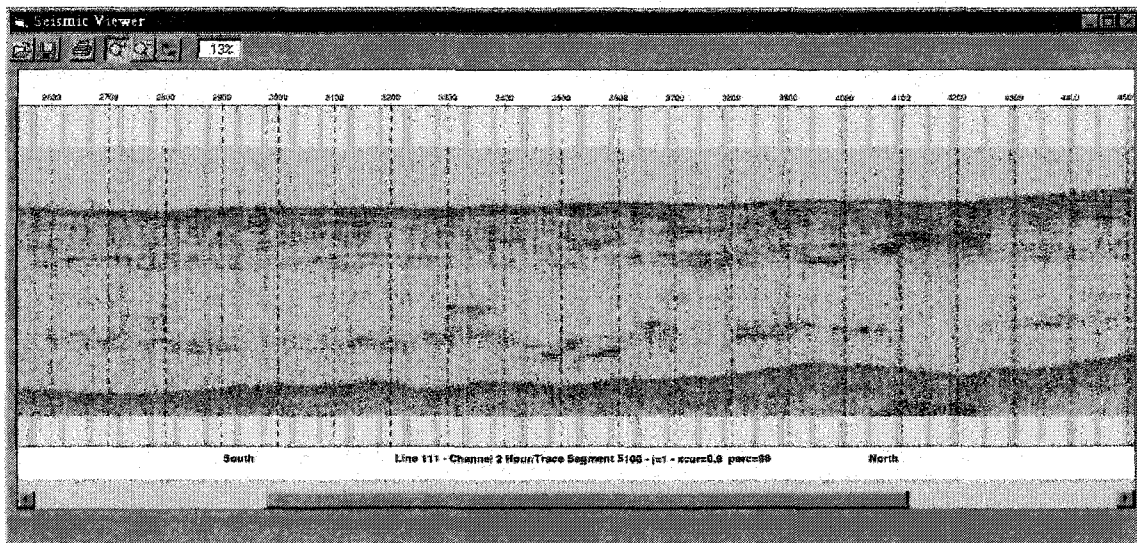the simple integration of multiple components without compromise to the quantitative aspects of the data.

Figure 2.3- Image showing a Huntec high-resolution seismic profile. This displaying program is connected to the ArcView layer showed in Fig. 2.1 (red vectors). This program allows zooming and displaying in different scales, taking advantage of the dynamic range of the data. This seismic profile is from the trackline highlighted in yellow in Fig. 2.1.

The software package allows the import of a variety of data types (either gridded or ungridded) from common mapping packages (GRASS, GMT/NetCDF,ISIS, and with the development of ArcConverter (see below) can directly import ArcView layers, as well ASCII data and/or a range of binary and image file types. For ungridded data, several approaches to gridding can be chosen to create a surface representation of the data. Any data brought into the system is fully geo-referenced in that one can always query the scene to get coordinates and related attributes.

75

Simple tools allow the assignment pre-existing colour maps or the design of specialized ones. Once a colour map is assigned to the data set, a lighting model is chosen including artificial sun-illumination, shading and true shadow calculations. The scene is then rendered to form a 3-D image that is natural looking and easily interpretable, yet fully georeferenced and quantitative. Colour, while used to represent depth in the images above, can also be mapped to other parameters (like backscatter or sediment properties) and draped over the digital terrain model. Numerous default colour maps are provided, as well as the capability to interactively 'draw' a colour sequence using the hue, saturation, and value (HSV) colour space, and instantly see how the resulting colour sequence enhances the data that is being viewed.

An interactive shading tool provides control over various lighting parameters such as the light direction, apparent glossiness of the surface and the amount of ambient (background) illumination. A particular feature of the system is the ability to define soft cast shadows. This dramatically increases the ability to perceive certain types of terrain features such as narrow pinnacles and sand waves. The surface data can be shaded directly or a different data set can be used to map the colour onto the surface. In this manner variables such as multibeam backscatter and sediment type can be instantly draped onto the visualized surface – all fully geo-referenced.

76

The user can interactively "fly" around the data and view it from all angles through the use of a 6-degree of freedom mouse that transforms simple hand motions into a data exploration tool (and thus the derivation of the name of software package – Fledermaus.). With special LCD glasses, the scene can be viewed in true stereo. Data entry is simple and 3-D interaction can take place within a few minutes of the production of a DTM or sonar mosaic. Thus if these products are created on board the vessel, 3-D interaction can be used for quality control, mission planning and in some cases mission execution.

Through the use of object-oriented software architecture, multiple, individual data sets with different levels of resolution can be easily combined, georeferenced, and displayed. Thus land-based DEM's with one level of resolution can be combined with multiple bathymetric data with different levels of resolution without the need to regrid at a common scale. Even more intriguing is the ability to texture map data at any level of resolution on top of lower resolution data. Thus high-resolution backscatter or video imagery can be mapped directly on top of lower resolution bathymetry without the need to degrade the higher resolution data or waste memory by upsampling the lower resolution data. A series of analytical tools is also available that provides for the calculation of gradients, slopes, areas, volumes and differences, all in the 3-D environment.

Interactive sessions with Fledermaus can be recorded and played back as a movie; with the addition of frame by frame video recording equipment full resolution videos of exploration sessions can be recorded or digital format videos easily created. In addition to the exploration of the data contained in the computer's virtual 3D environment, Fledermaus also provides a true 3D stereoscopic display. Normal human stereoscopic vision only works over a limited range. People perceive very little stereoscopic depth at distances greater than 30 meters and optimal stereoscopic viewing is between 50 cm and 2 m. Fledermaus incorporates a stereo viewing algorithm that automatically adjusts the stereo viewing parameters so that stereoscopic depth is obtained even for scenes that are at large (virtual) distances. Fledermaus is unique in that, these parameters are constantly adjusted so that even while 'flying' through a virtual data environment, stereo depth cues are always available. The primary advantage of a stereo display is that the ability to perceive relative object positions and sizes within the 3D scene is greatly enhanced compared to the traditional projection of a 3D scene onto the computer's 2D screen.

2.9 Arc-Converter

The Arc-Converter is a software filter that transfers data layers from one ArcView project directly into a format that can be interpreted by Fledermaus. It was developed in Visual C++ and is fully integrated in the Fledermaus suite. The first step of the conversion is to parse an ArcView

78

project file (extension APR) in order to retrieve a list of layers and the location where the files are stored. The retrieved layer list is organized in three basic categories: raster, vector and grid. The raster category encompasses all images with their geocodification. The vector category includes point, line and polygon data. The grid category groups all digital elevation models supported by ArcView.

After the list is retrieved from the project file, one or more data layer can be automatically transferred to the Fledermaus 3-D environment. For that, the ArcView files corresponding to the chosen layer must be translated to the Tagged Data Representation Format (TDR) of Fledermaus. The TDR format is a framework suitable for storing blocks of information in a file structure. Each TDR file is divided into data blocks, each of which can store a different type of information to be processed. At the beginning of each block there is a tag that uniquely identifies the type and characteristics of the data block (Paton, 1995). Thus, a TDR file can basically store any kind of information, which is extremely convenient in the case of transferring ArcView objects. The following applications will translate ArcView data layers directly into TDR format:

2.9.1 Vector Data

This application will translate ArcView layers with vector data of point, lines and polygons into the TDR format. ArcView vector data is

79

stored in a Shapefile, which is a spatial data format that stores the non-topological geometry and attribute information of spatial features (ESRI 1998). It is actually a set of three different files with the same name but different extensions. The geometry of the features is described in the file with extension SHP. This file has a fixed-size header followed by a variable number of records. Each record describes one geometric entity of variable length, by a sequence of vector coordinates. The second file, with extension SHX, has an index to the feature in the file extension SHP. The attributes of each spatial feature are stored in a third file with extension DBF. This file follows the dBase format, which is a structured table for database applications. The dBase table has one record (line on the table) for each corresponding spatial feature in the file extension SHP. Each record of the table can have any number of fields (column on the table), where each field represents one attribute of the spatial feature. The spatial features and its attributes are transferred to data blocks in a TDR file, where full geometrical and topological structures are preserved. The developed application supports Shapefile records of points, polylines (linear vectors), polygons and null records.

2.9.2 Digital Elevation Models

This application will parse an ArcView floating-point or integer grid file and will build a digital elevation model, which will be transferred to a TDR file. An ArcView grid file is actually a directory file structure typically with 5 or more binary files. The grid data itself is stored in the

80

first file called w001001.adf. This file is organized in data tiles with the aim of optimizing access time and storage. The second file called dblbnd.adf contains the bounds of the grid in projection coordinates. The header file (hdr.adf) contains the number of tiles into which the grid is divided and the total number of tiles. The file sta.adf contains statistical information about the grid, such as minimum value, maximum value, standard deviation etc. The last file (w001001x.adf) is an index to the tiles of the file w001001.adf. Each tile is stored and compressed in a different manner. The actual organization and format of these files and the description of the data tiles is proprietary to ESRI, and at the moment we do not know of any formal documentation concerning this matter. The task of unravelling these file formats was partially done by a community of users (Warmendan, 2000), from which we obtained the information necessary to build our translator. At the moment, the system can handle the following tile types: constant blocks, 1 bit data, 4bit data, 8bit data in sequence, compressed or run-length encoded, 16bit data in sequence, compressed or run-length encoded, 32bit data run length encoded, and float point.

2.9.3 Raster Images

This application will read any type of raster image from one ArcView project with its respective geocodification and transfer it to a TDR file. In ArcView, images are regarded as a matrix, where only a row and a column are sufficient to reference each cell. In order to proceed

81

with the transformation from image coordinates to projection coordinates, it is necessary to have a 4-parameter transformation matrix, since ArcView only handles scale and translation. Any rotation or higher order distortions have to be done prior to bringing the image into ArcView. This is a major limitation, as it restricts the image to one single cartographic projection. The required geocodification parameters for this transformation are the imaged bounds in a cartographic projection and the pixel size. The geocodification can be read directly from the image file, which is the case for GeoTIFF, BSQ, BIL, BIP and ERDAS formats. In other cases, the geocodification can be read from a second ASCII file, called the world file. This file has the same name of the image file with the letter w added to it. In both cases, the image will be translated to TDR format at the proper location, scale and projection.

2.10 Exploring the 3-D STRATAFORM Database

We illustrate both the functionality of the ArcConverter process and the powerful interpretive benefits derived from interactive 3-D visualization by further exploring the STRATAFORM database. First, we show an example of a grid transfer. The bathymetric and topographic data sets from the STRATAFORM project came from different surveys and were gridded at different resolutions (Fig. 2.4). Each of these data sets were ArcView grid files and through ArcConverter are transferred into Fledermaus TDR files, now allowing full interactive exploration and interpretation (Fig. 2.5). Note that the Seabeam grid has some residual

82

artifacts in the direction of the ship track. These artifacts, related to inappropriate corrections for the sound speed profile become clear in the 3D scene.
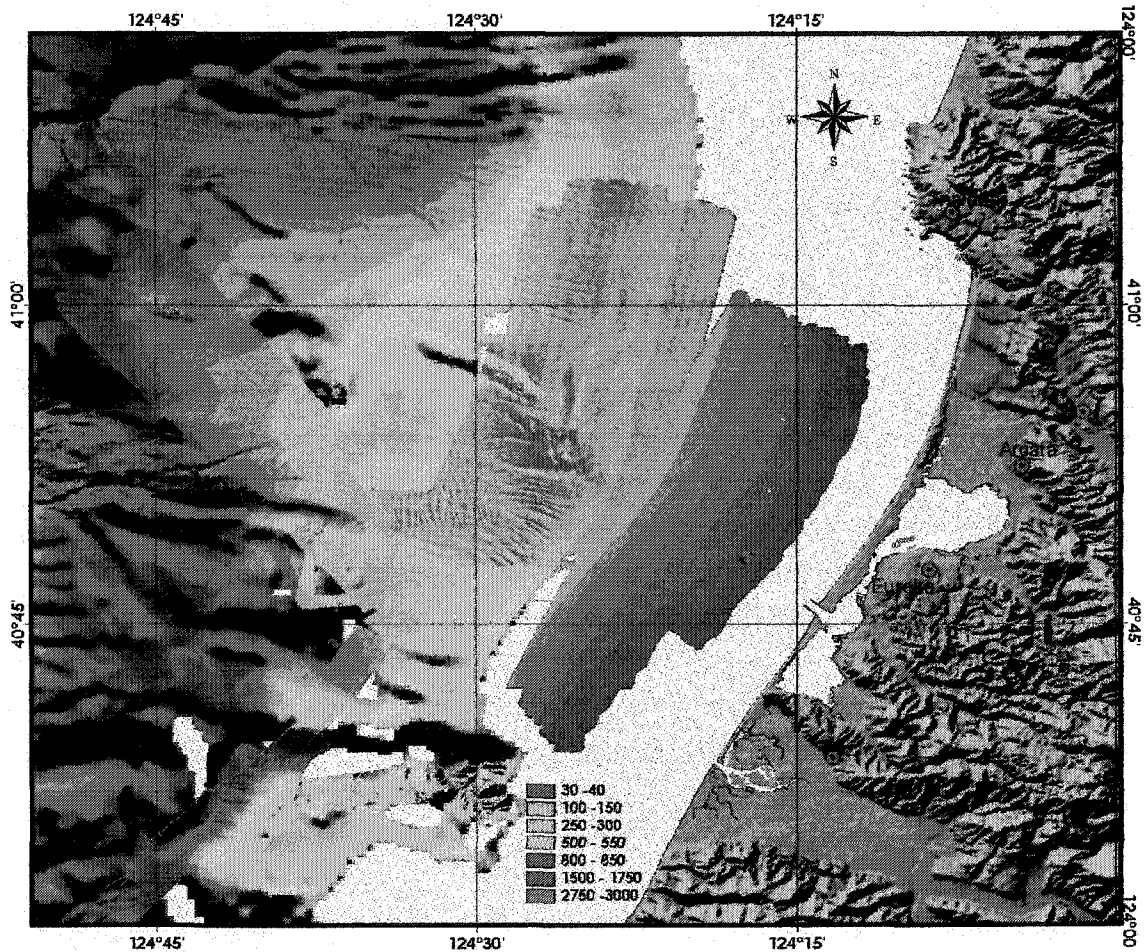

Figure 2.4- STRATAFORM project in Arcview, showing the following layers: 1) SeaBeam 12 kHz Multibeam echo-sounder bathymetry gridded at 6.48" (~180m) resolution. 2) Atlas Hydrosweep multibeam echo sounder bathymetry gridded at 2.16" (~60m) resolution. 3) Simrad EM300 30kHz Multibeam sonar bathymetry gridded at a 0.72" (~20m) resolution. 5) Simrad EM1000 95kHz Multibeam sonar bathymetry

83

gridded at a 0.60" resolution. 6) USG digital elevation model USA in a 1:100 000 scale.
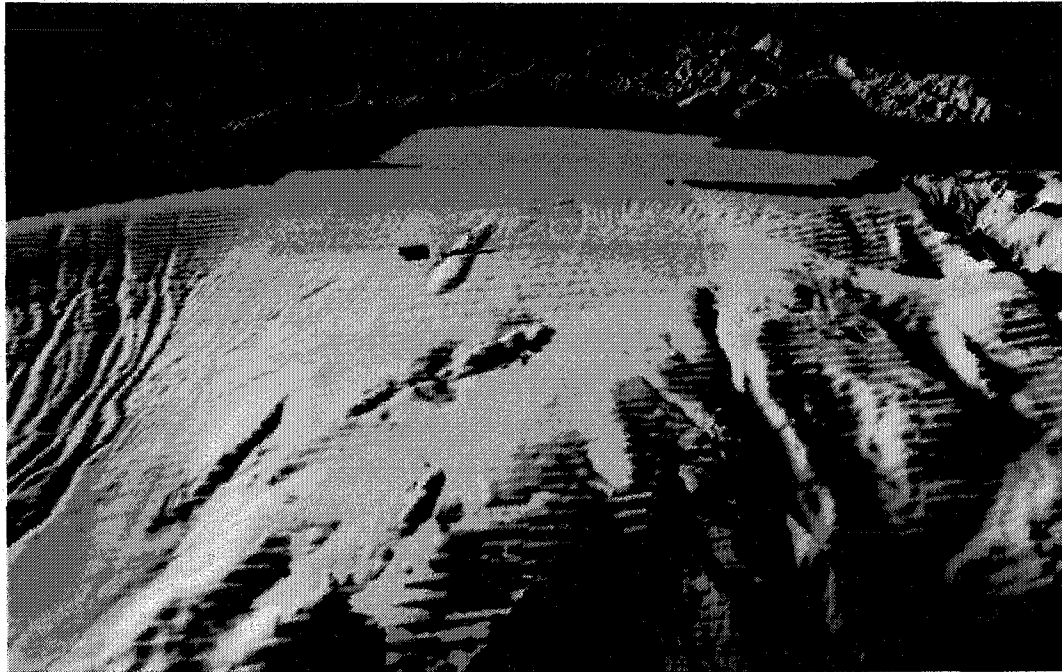

Figure 2.5- The same data layers as shown in Fig. 2.4 converted to Fledermaus format and displayed in Fledermaus.

The raster backscatter mosaics from multibeam and sidescan sonars shown in Fig. 2.1 were directly transferred to Fledermaus though Arc-Converter. These images are mapped as texture over the bathymetric grids shown in Fig. 2.4 and Fig. 2.5. Figure 2.1 also contains vector layers of points (CTD profiles) and of polylines (Seismic tracklines), which were also transferred to the 3D environment. The resulting 3D view is shown in Fig. 2.6. Figure 2.7 shows a detail from Fig. 2.6 where the actual seismic profile and not just its trackline can be seen in the 3D scene.
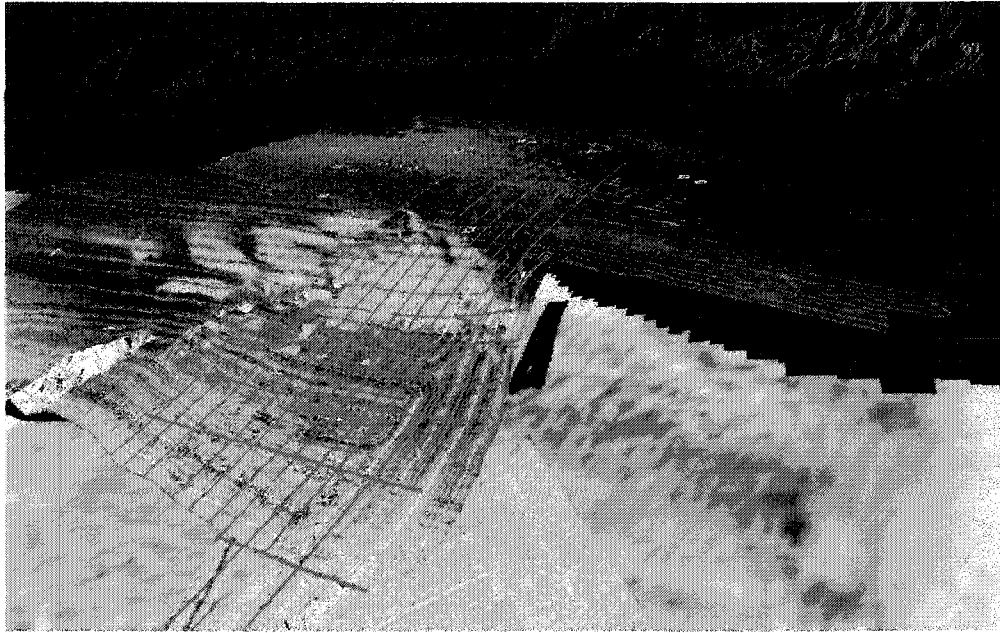
84

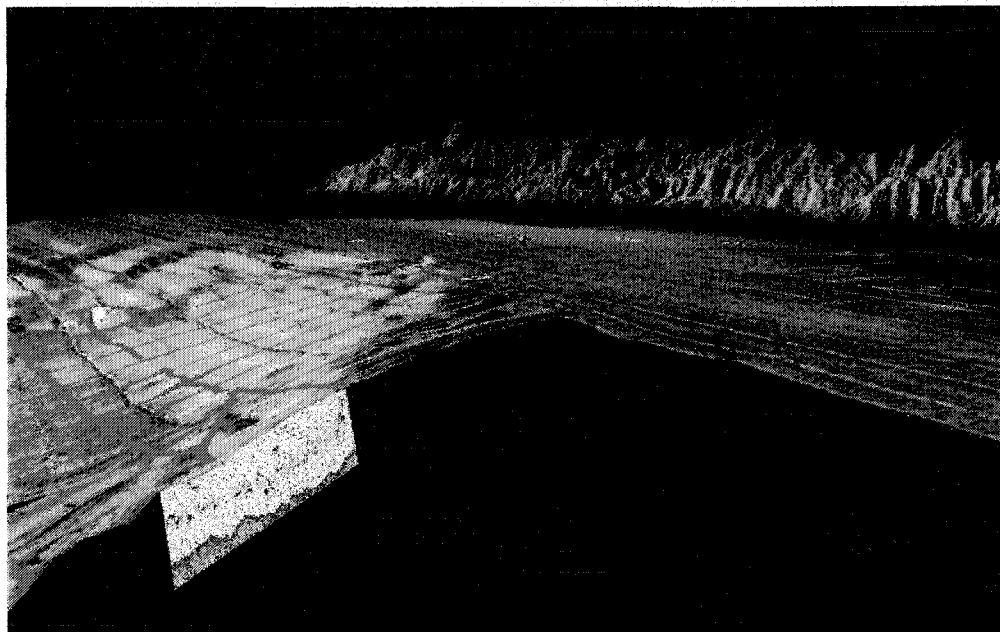Figure 2.6- The same data layers shown in Fig. 2.1 converted to Fledermaus format.

Figure 2.7- Detail from Fig. 2.6, showing the seismic profile. This line is from upper portion of the Humbold slide, showing an undeformed slope stratigraphic sequence and its relation to the regional dip of 3 degrees.

85

The ability to interactively explore, in 3-D the complex relationships between topography, backscatter and the subsurface seismic data have allowed STRATAFORM scientists to a resolve long-standing debate on the origin of a topographic features on the lower slope. The ability to correlate surficial backscatter with subsurface outcrops provided a direct explanation for the origin of both topographic and backscatter targets. Additionally the ability to directly relate subsurface structure with surficial topography led investigators to conclude the structures were the result of a massive sediment slide (Gardner et al., 1999).

An example of a polygon layer is shown in Fig. 2.8, where Thiessen polygons are drawn around sparse measurements of grain size measured from core samples. A symbol highlights the location of every core. The colours of symbols and polygons are related to the grain size. These polygons were converted to Fledermaus format (Fig. 2.9).

While the 2-D display allows us to see the relationship between grain size and backscatter (the underlying layer), we cannot see the relationship of both grain size and backscatter to depth. In the 3-D environment we can easily and intuitively resolve the complex relationships between backscatter, grain-size and depth without the need for further analyses.
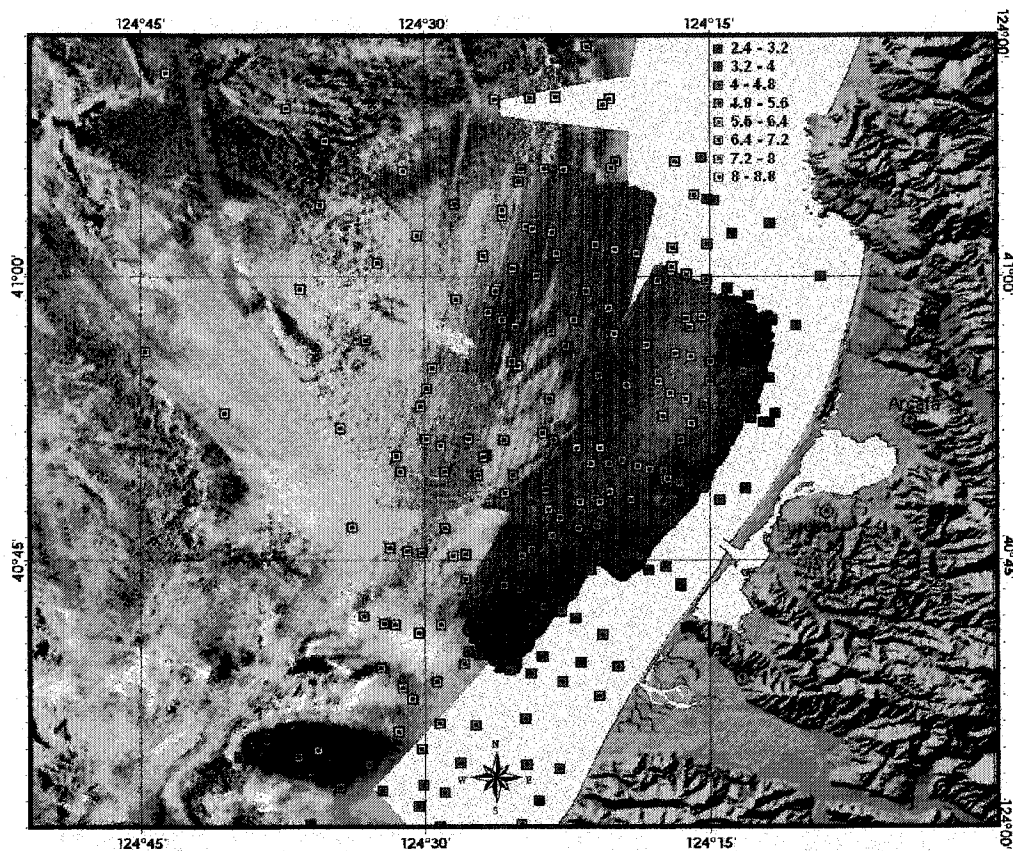
Figure 2.8- Grain size distribution from core data. The colours of symbols

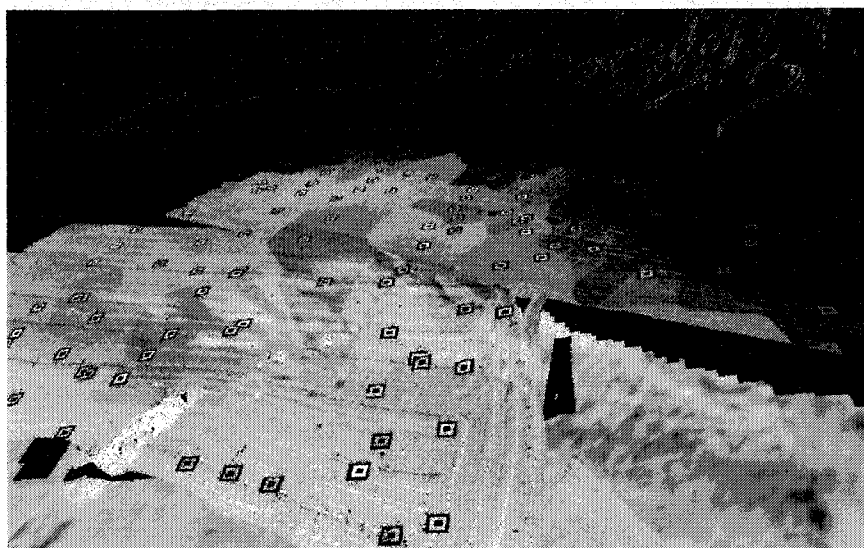and polygons are related to the medium grain size.

Figure 2.9- The same layers shown in Fig. 2.8 converted to Fledermaus

format.

2.11 Conclusions

The huge amount of information produced by modern acoustic remote sensing systems and other marine surveying tools present great challenges to management, analysis and interpretation of marine data. While GIS systems have become the standard for exploring multiparameter, georeferenced data sets, the 2-D map paradigm of the traditional GIS is often insufficient to allow for the full extraction of the complex inter-relationships typical of the marine environment. We have developed an approach that takes full advantage of the well-established capabilities of the ArcView GIS system and extends these capabilities through an interface to a powerful, interactive, fully georeferenced 3-D visualization system (Fledermaus). This approach, when applied to a very large and complex marine database collected off Northern California, greatly improved our ability to explore and analyze a range of geological and geophysical processes in a relatively simple and intuitive manner.

CHAPTER III

MAPPING NEAR-SURFACE GAS WITH ACOUSTIC REMOTE SENSING

METHODS

3.1 Abstract

The location and distribution of near-surface gas in continental margins is of particular interest for oil exploration and development programs. The presence of gas seepages can be evidence of the possible existence of subsurface hydrocarbon reservoirs. Gas is also a potential hazard for offshore facilities, as it decreases the strength of unconsolidated sediments increasing the risk of seafloor failures and slumps.

Acoustic remote sensing systems such as multibeam and sidescan sonars can be used for mapping and detection of near-surface gas in marine sediments. These systems can provide a realistic depiction of the seafloor by means of the simultaneous acquisition of co-registered high-resolution bathymetry and calibrated seafloor backscatter. An acoustical backscattering model for gassy sediments is used to recognize gas signature in multibeam sonar records. Additionally, analysis of backscatter images and detailed bathymetry reveals anomalous seafloor

features, which are associated with gas expulsion. These processed acoustic remote sensing data can be interpreted in conjunction with other geological, geophysical and geochemical data from an exploration area, to help explain the distribution and origin of near-surface gas. Such analysis is done in a GIS environment with 3D visualization capability.

3.2 Introduction

The location and distribution of near-surface gas in continental margins is of particular interest for offshore oil exploration and development programs. Gas seepages can be the result of upward migration from deep-seated reservoirs and thus a potential indicator of hydrocarbons (Mello et al., 1990). The identification of near-surface gas accumulations by acoustic remote sensing techniques could thus provide a first evaluation of the hydrocarbon potential of an offshore area and reduce considerably the exploration risk. Gas is also a potential hazard for offshore engineering facilities, as it reduces the strength of unconsolidated sediments, increasing the possibility of seafloor failures and slumps. Gassy unconsolidated sediments combined with steep bathymetric slopes are normally associated with areas of highly unstable seabed. In this case, the rapid identification of the presence of near-surface gas by acoustic remote sensing techniques could be invaluable for assessing geohazard potential. Herein, we describe an approach for

90

using multibeam sonar data to evaluate the presence and relative abundance of gas in near-surface sediments. This approach is applied to an area of known gas production off the coast of Northern California.

Multibeam sonar systems map the seabed through a wide range of grazing angles, producing detailed bathymetry and revealing subtle differences in the backscatter response for different materials on the seafloor (de Moustier and Alexandrou, 1991). Gas bubbles, even in very small quantities, can dominate and change the geoacoustic characteristics of seafloor sediment and have a significant effect on the propagation of acoustic waves (Lyons et al., 1996). If gas bubbles are trapped in the sediment structure, their scattering contribution will be relatively stronger and will control the total backscattering response. A model has been developed that predicts the backscatter response of marine sediments as a function of sediment and seafloor properties, water depth and gas content (Fonseca and Mayer, 2001). When applied to multibeam sonar data, this model can be used to predict and recognize distinctive backscatter signatures caused by the presence of gas.

In addition to backscatter response, multibeam sonar data may contain other features that are associated with gas expulsion. These include pockmarks, authigenic carbonate precipitations and chemosynthetic shellfish communities. Pockmarks, which are circular

91

depressions developed in soft bottom sediments caused by gas or fluid expulsion from the seabed (Hovland & Judd, 1989), are easily recognizable in multibeam sonar bathymetry. Authigenic carbonate precipitations are caused by the oxidation of the seeping fluids by bacterial communities (Kulm and Suess, 1990). This deposited mineral has high acoustic impedance that can be identified in sonar backscatter records. Communities of shellfish often form in the vicinity of seepages. These communities form a food chain based on the chemosynthesis of the seeping hydrocarbons, and their hard shells can imprint a characteristic return in sonar backscatter records (Orange et al, 1999).

The Eel River Basin offshore Northern California will be used to assess the applicability of acoustic remote sensing methods for the location of near-surface gas accumulations. The Eel River Basin was extensively investigated as part of the *STRATAFORM* (STRATA FORmation on the Margins) project, a multi-year, multi-investigator program funded by the U.S. Office of Naval Research (Nittrouer, 1998). During this project, an immense database of marine information was collected (Mayer et al., 1999), including acoustic remote sensing data collected at 95kHz (multibeam sonar) and at 100kHz (sidescan sonar). The acoustic remote sensing data will be analyzed in conjunction with other layers of information available in the exploration region, including a core database, structural maps, location of wells, geochemical data and geophysical data. This analysis will attempt to link anomalous acoustic

92

backscatter on the seafloor to sub-surface structures, a necessary step toward the understanding of the stratigraphic or tectonic control of seafloor seepages. New visualization techniques, which take advantage of 3D tools and GIS integration, are used to help analyze and understand these complex relationships in a natural and intuitive manner.

3.3 Geologic Setting

The Eel River Basin is located north of the Mendocino triple junction, where three major tectonic plates intersect: the North American, Gorda and Pacific plates (Field, 1980). The Basin extends 200km northwards from Cape Mendocino, California until Cape Sebastian, Oregon (Fig. 3.1). The eastern boundary of the basin is the coastline and the western boundary is the continental slope, which coincides with the eastern boundary of the Gorda Plate. The south portion of the basin extends 50 km inland in Humbold Bay, exposing Tertiary deposits.

The Eel River margin is structurally complex and is located in a tectonically active area. Its major morphologic features were developed during late Tertiary and Quaternary in response to tectonics forces (Clarke, 1987). The subduction of the Gorda plate beneath the North America plate produced a fore-arc trough, where the Eel River Basin sediment deposits accumulated. This normal subduction in conjunction with the northward migration of the Mendocino triple junction have

93

produced a system of north-northwest-trending faults and compressional fold axes throughout the basin. A major feature crossing the study area is the Little Salmon Fault (Fig. 3.14), which has a total throw of 2000m (Wagner, 1980). Many exposed anticlines and diapiric structures outcrop on the seafloor, suggesting active plate coupling. This area has a history of seafloor instability, showing some major slide features (Fig. 3.13). One of them, the Humbold slide, contains evidence of abundant pockmarks (Gardner et. al, 1999). Offshore of the self and slope abundant Quaternary deposits were developed (Carver, 1987). The Eel River is the primary source of terriginous sediments for the basin. Another source is the Mad River, which contributes only about 10% of the total sediment discharge.

The northern California continental margin reveals evidence of abundant subsurface gas and numerous seafloor expulsion features (Yun et al., 1999). Seismic-reflection profiles confirm the presence of subsurface gas throughout the Eel River basin. Differential sediment loading and tectonic activity have caused overpressure on the gas generated in deep layers. This overpressured gas migrates to the seafloor through permeable pathways, creating anomalous geologic and biologic features, such as pockmarks and chemosynthetic communities (Hovland & Judd, 1989).
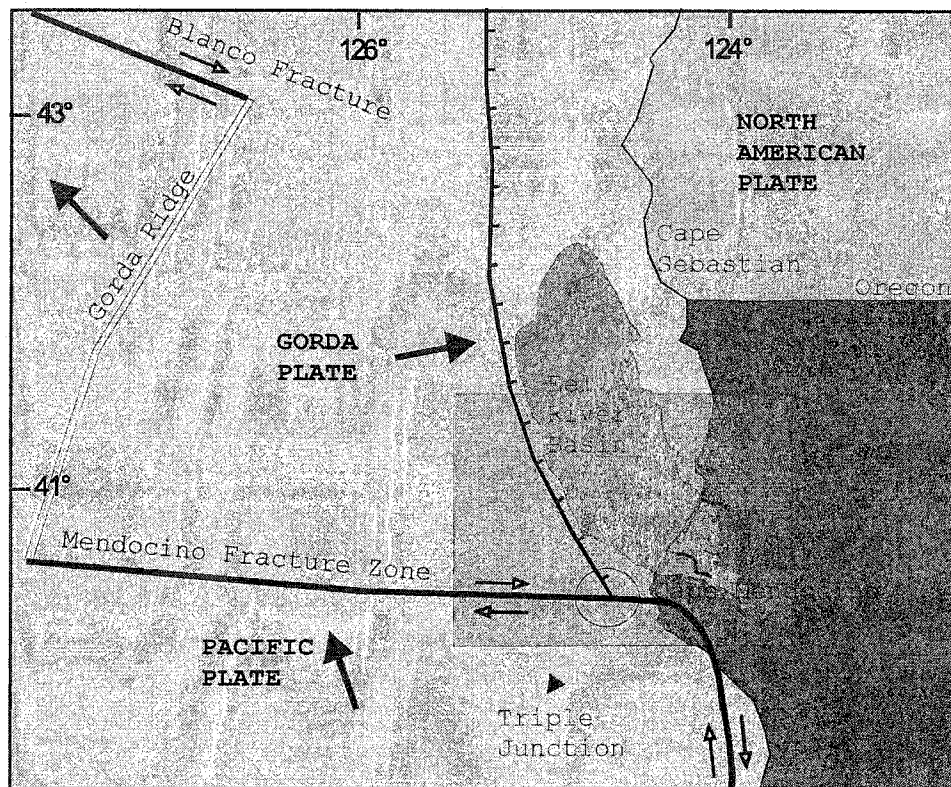
94

Figure 3.1- Eel River Basin with major plate boundaries (Clarke, 1987).
The study area is show in the highlighted box.

There is evidence that the gas seepages and related features observed offshore have both biogenic and thermogenic origins. Analyses of cores have shown thermally produced hydrocarbons in sediments samples recovered from offshore California (Kvenvolden and Field, 1981). This thermogenic gas has been reported to rise to the seafloor from generating rocks though tectonic feature and on the border of anticlines. Near to the Eel River and Mad River mouths, there is also evidence of biogenic gases derived from bacterial alteration of organic matter (Yun, 2000).

95

3.4 EM1000 Multibeam data

Multibeam sonar bathymetry and backscatter data were collected in the Eel River Basin in 1995 (Goff et al., 1999). The system used during the survey was a Simrad EM1000 multibeam sonar. This equipment is a precision seafloor mapping systems designed for shallow to medium water depths, with an operating frequency of 95kHz. The raw datagrams recorded during the survey have a depth value and a backscatter time series for each beam (Anonymous, 2000). Figure 3.2 shows a mosaic of the acoustic backscatter collected during the survey and the location of core sampling sites, collected during the course of the STRATAFORM program. The analysis of core samples at various locations provides local measurements of sediment physical properties. Some core sites also have measurements of free gas content in the sediment.

The raw backscatter datagrams recorded during the survey were processed and radiometrically corrected for further analysis. The processing consists of recovering the datagram structure and locating each beam in a cartographic projection. Radiometric corrections include the removal of the time varying and angle varying gains applied during acquisition, calculation of the true grazing angle with respect to a bathymetric model, and correction for footprint size. The bathymetric

96

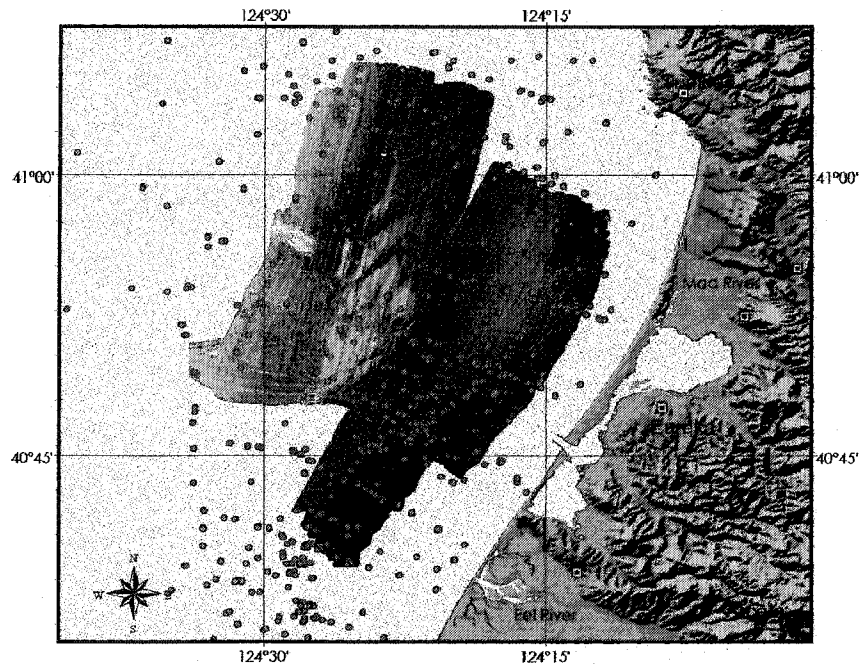model is obtained by gridding the refraction- and motion-corrected depth solutions available for each beam.

Figure 3.2– Multibeam sonar survey area showing acoustic backscatter response (High backscatter in white, low backscatter in black). The red dots are core-sampling sites.

The map shown in Figure 3.3 is a corrected backscatter mosaic for the survey area. Only beams with grazing angles between 30° and 60° were used for the mosaic, in order to avoid the strong specular component of the backscatter near nadir and the effects of the critical angle at small grazing angles. The angular sector between 30° and 60° is also the most sensitive to volume backscatter, as in the near nadir region the backscatter is dominated by seafloor roughness and impedance

97

contrasts. Furthermore, beyond the critical angle only a small fraction of the acoustic energy penetrates the seafloor, which makes volume scatter a secondary contribution. The beams for the selected angular sector were averaged over 20 consecutive sonar pings. The mean backscatter value, averaged over grazing angles from 30° to 60°, was assigned to the centre of the seafloor patch ensonified by these beams. This represents a footprint size of between 50m to 200m depending on the water depth.
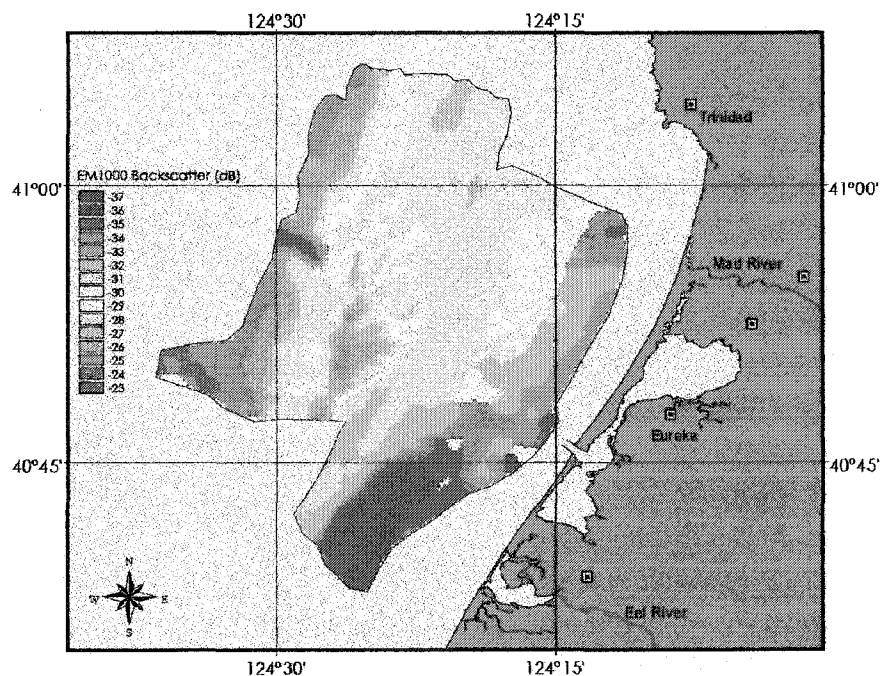

Figure 3.3 – Corrected backscatter response.

3.5 Backscatter Response Simulation

Fonseca and Mayer (2001) describe a model for the high-frequency backscatter angular response that estimates the backscattering strength

98

for a particular seafloor type as a function of frequency and grazing angle. This model is an extension of the model developed by Jackson et al. (1986) and is based on seven parameters that reflect sediment physical properties and seafloor roughness (Equation 1): a) one parameter for gas fraction in the sediment structure (ξ); b) two parameters for impedance, sound velocity ratio (v) and density ratio (ρ); c) one parameter for attenuation: loss tangent (δ); d) two parameters for roughness, the spectral strength (ω_2) and the spectral exponent of bottom relief (λ), and; e) one parameter for volume contribution ($\sigma2$). The acoustic frequency (f), the depth (d) and the grazing angle (θ) of the wave front with the seafloor are treated as given parameters. Using this model, we can estimate the backscattering cross section of a seafloor patch provided that we can measure the model parameters at this location. This process is known as backscatter response simulation.

$$\sigma_t(\theta, f, d) = F(\theta, f, d; \quad \xi, \rho, v, \delta, \omega_2, \lambda, \sigma_2) \tag{1}$$

σ_t - Total backscattering cross-section per unit solid angle per unit area.

The backscatter response simulation will be done on a sub-area of the Eel River Basin where we have sufficient knowledge of the model parameters. The model parameters are obtained from available cores in the survey area (Fig. 3.2). Almost all the cores have measurement of grain size, sound speed and bulk density. There are no available

99

measurements of the roughness parameters and very few measurements of attenuation for the studied sites. In these situations, a parameterization in terms of the bulk grain size was used (Anonymous, 1994). Figure 3.4 shows Thiessen polygons drawn around measurements of grain size obtained from core samples. The colours of the polygons are proportional to the grain size. Similarly, Fig. 3.5 shows Thiessen polygons drawn around measurements of acoustic impedance (sound speed x bulk density).

The distribution of sediment properties shown in Fig. 3.4 and Fig. 3.5 are used as inputs for the backscattering model. Initially, it is assumed that there is no gas in the sediments. Figure 3.6 shows the simulated backscatter image. The model predicts a higher backscatter in shallow water, where coarser high-impedance sediments are present. In deeper waters, the model predicts lower backscatter, due to the low acoustic impedance and finer grain sizes. Note that the simulated backscattering response is quite different from corrected backscatter measured by the multibeam sonar (Fig. 3.3). The simulated response based on measured physical properties shows high backscatter in shallow water and low backscatter in deep water while the corrected measured backscatter shows the opposite trend.
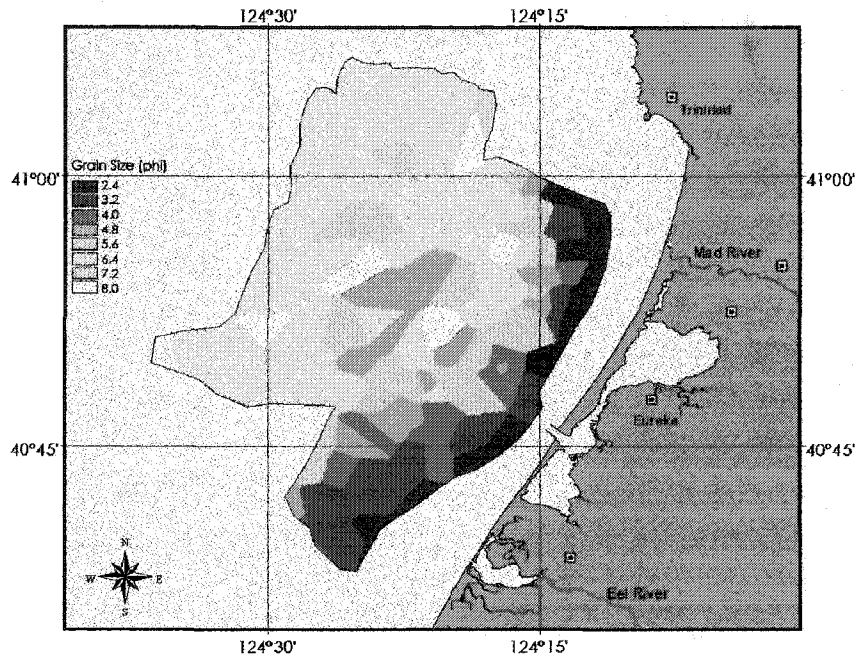
100

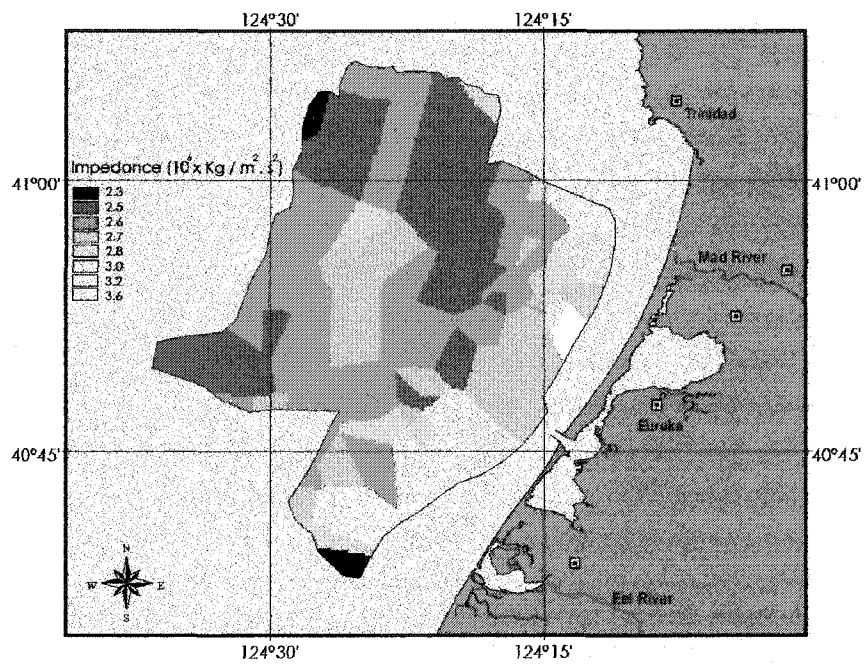Figure 3.4 – Thiessen polygons of grain size.

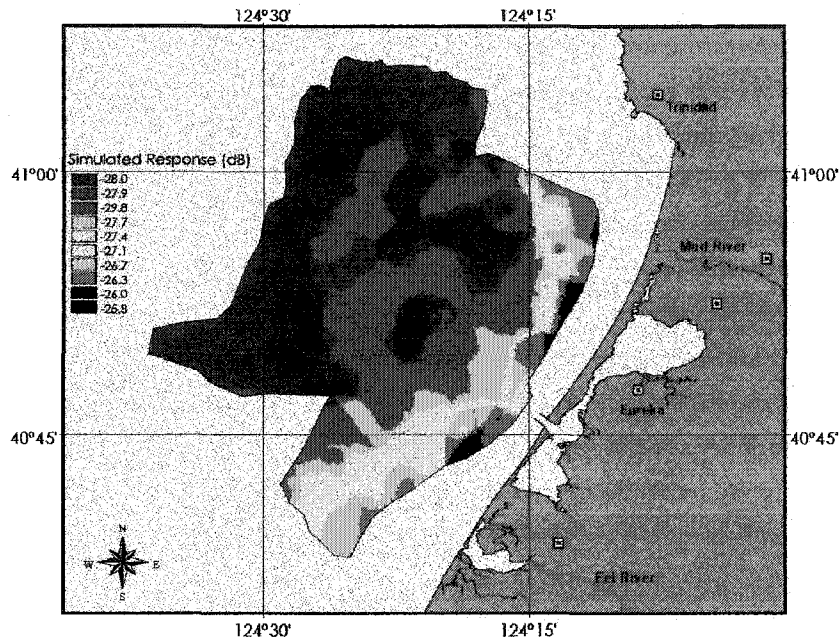Figure 3.5 – Thiessen polygons of impedance.

101

Figure 3.6 – Backscatter response simulation.

3.6 Integrated GIS Analysis of Backscatter Anomalies

The total backscatter anomaly can be calculated as the difference between the measured and the expected backscatter. The measured backscatter is the corrected backscatter response showed in Fig. 3.3. The expected backscatter is the result of the response simulation of Fig. 3.6. The calculated backscatter anomaly is shown in Fig. 3.7.

Several factors may explain the backscatter anomaly, including changes in seafloor roughness that were not accounted for in our parameterization from grain size data, or the effect of gas. Figure 3.8 makes clear that depth is highly correlated to the backscatter anomaly

102

and, as will be discussed further, supports an association with the presence of near-surface gas.
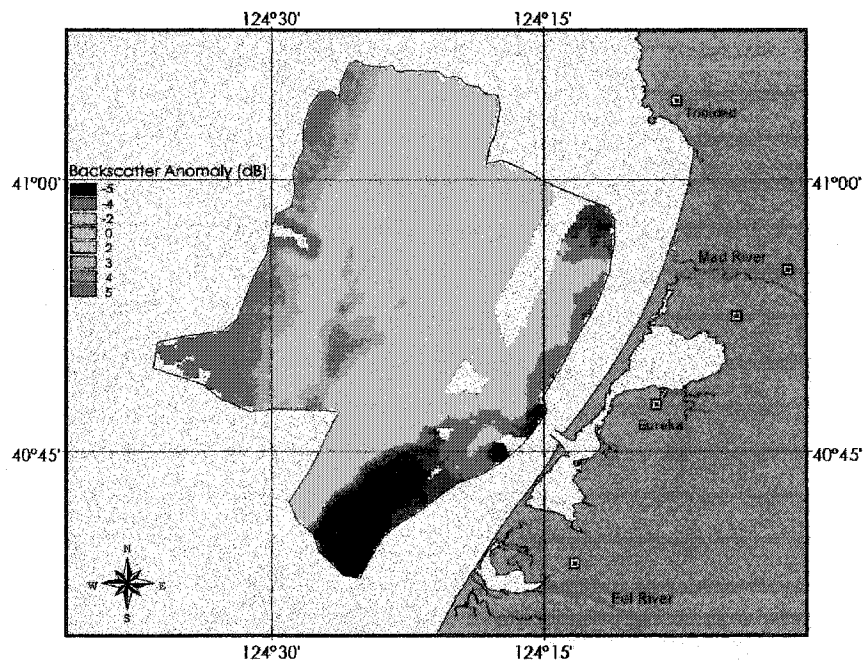

Figure 3.7 – Backscatter anomaly.

The acoustic backscatter model presented in Fonseca and Mayer (2001) shows that depth plays an important role in the backscatter response of gassy sediments. In deep water a small amount of gas can result in a very high backscatter, a consequence of the higher bubble stiffness at high ambient pressure. In shallow water (less than 100m), the interface backscatter is severely reduced when the sediment is charged with free gas, due to decrease of sediment sound speed. Additionally, the volume contribution in shallow water is lower, due to higher attenuation of the bubbles in lower ambient pressure. This

103

combination of factors often results in a net decrease in the total backscatter response in shallow water, relative to a gas-free sediment with the same physical properties.
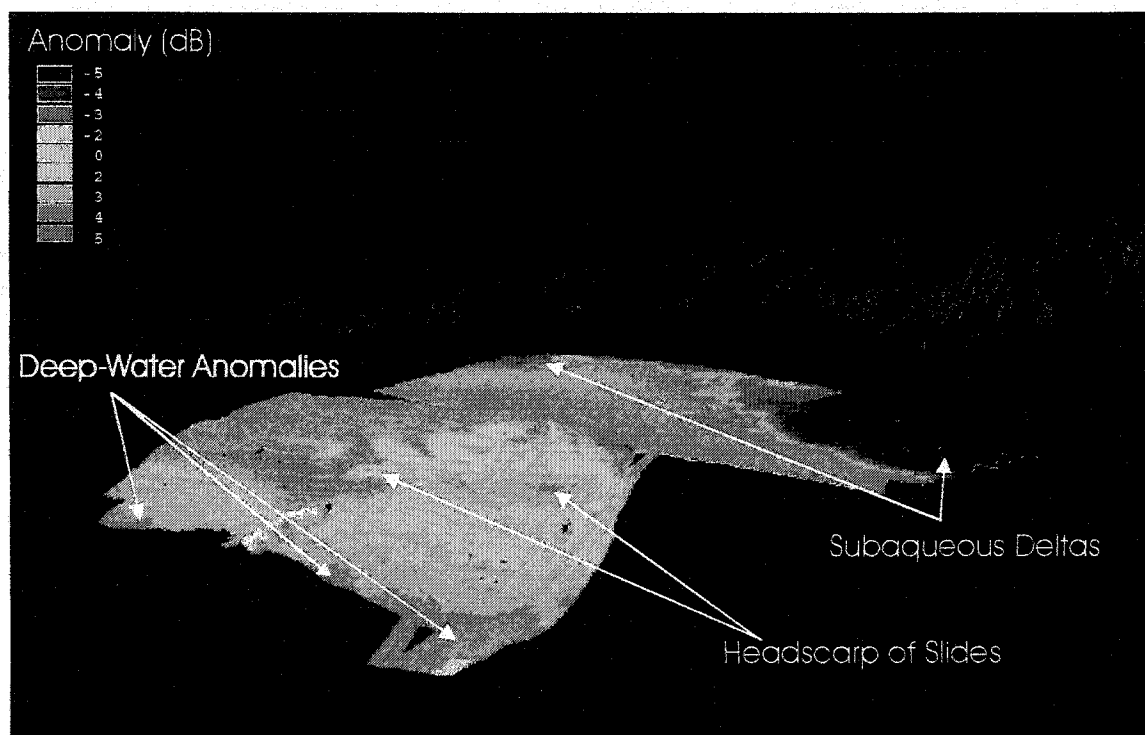
Figure 3.8 – Backscatter anomaly – 3D view

3.6.1 Near-Shore Negative Anomalies

There are two prominent negative backscatter anomalies (zones where the measured backscatter is less than the predicted for the measured physical properties) on the Eel and Mad River subaqueous deltas (Fig. 3.8). These two anomalies are located in shallow water (45m) and are associated to near-shore sand deposits delivered by the rivers. They represent the coarsest sediments in the survey area. Based on the

104

backscatter model, high backscatter is expected from these coarse sediments, the opposite of what is seen in the measurements. The measured negative anomaly cannot be explained by means of seafloor roughness. Even if we assume a very smooth seafloor, with the lowest possible roughness parameters, the expected backscatter would still be 5dB higher than measured.

Gas was reported in this area based on measured geochemical anomalies. Gas bubbles that rise though the water column are detected and measured at sea using a towed gas chromatograph (hydrocarbon sniffer) (Fig. 3.9). The measured hydrocarbons are predominately methane, suggesting a microbial origin for the gas, which is expected in the organic rich sediments of river subaqueous deltas (Yun, 2000). Additionally, a towed electromagnetic survey conducted over the area revealed a distinctive resistivity profile across the Eel River delta that could be due to a small gas fraction within the sediment structure (Evan et al, 1999).

A small amount of free gas on the sediment structure can explain the prominent negative backscatter anomaly on the Eel River subaqueous delta. The high concentration of hydrocarbons measured in the water column suggests the presence of free gas in the sediment structure, from where the hydrocarbons are seeping. The backscatter angular response for the coarse sands of the Eel River delta can be

105

calculated using sediment properties measured at the core sites. The parameters used as input for the model are: grain size 0.117mm, density 1994 kg/m^3 and sound speed 1677m/s. The model was then run a second time, including a gas fraction of 0.03 and the depth (45m). The result is shown in Fig. 3.10 for the total backscatter strength with and without gas. Note that the model predicts as much as 10dB backscatter reduction due to the presence of gas.
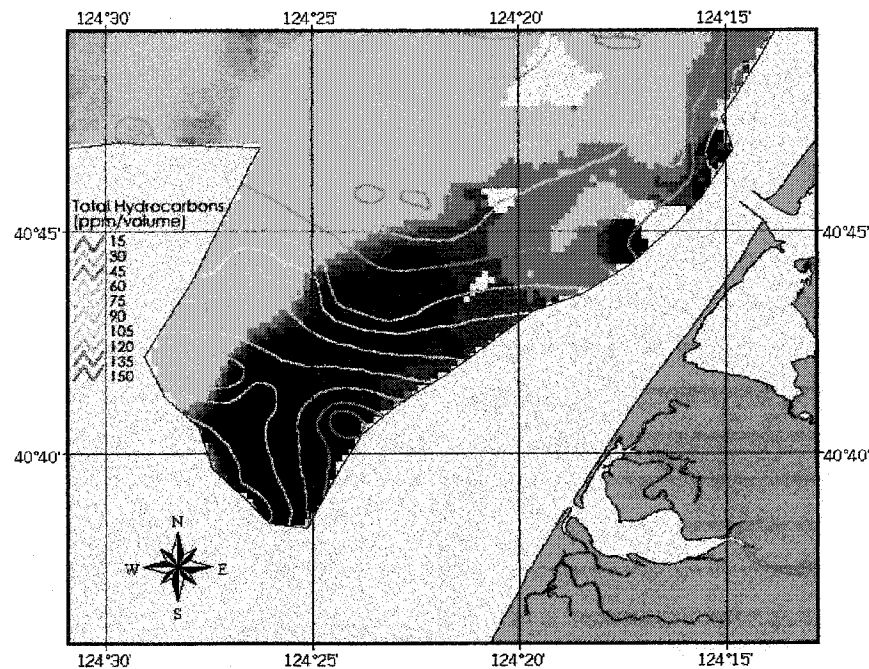

Figure 3.9 – Contour lines of concentration of hydrocarbons in the water column, measured at sea using gas chromatographic methods (from Yun, 2000). The background image is the backscatter anomaly of Fig 3.7.
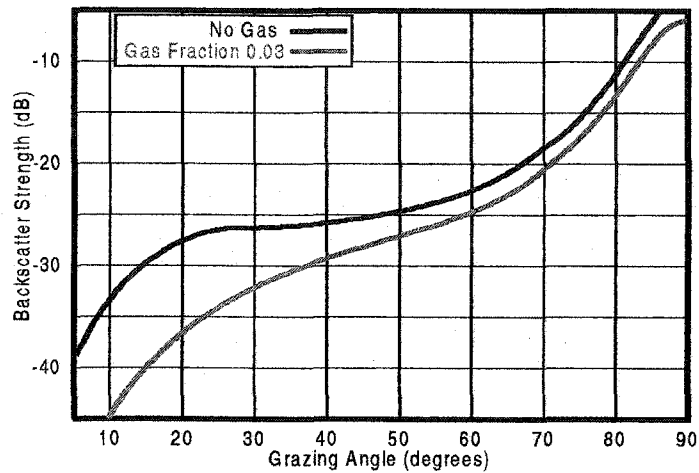
Figure 3.10 -Model response at 95kHz using the sediment properties measured at the Eel River Subaqueous delta.

3.6.2 Deep-Water Positive Anomalies

Figure 3.8 shows an extended positive backscatter anomaly in water depths beyond 400m. The location of this positive anomaly coincides with a high occurrence of pockmarks on the seafloor (Fig. 3.11). The density of seafloor pockmarks was interpreted on the records from deep-towed sidescan sonar (100KHz Datasonics SIS-1000). These sidescan sonar records showed nearly 4,000 pockmarks from 10m to 25m of diameter (Yun et al., 1999).
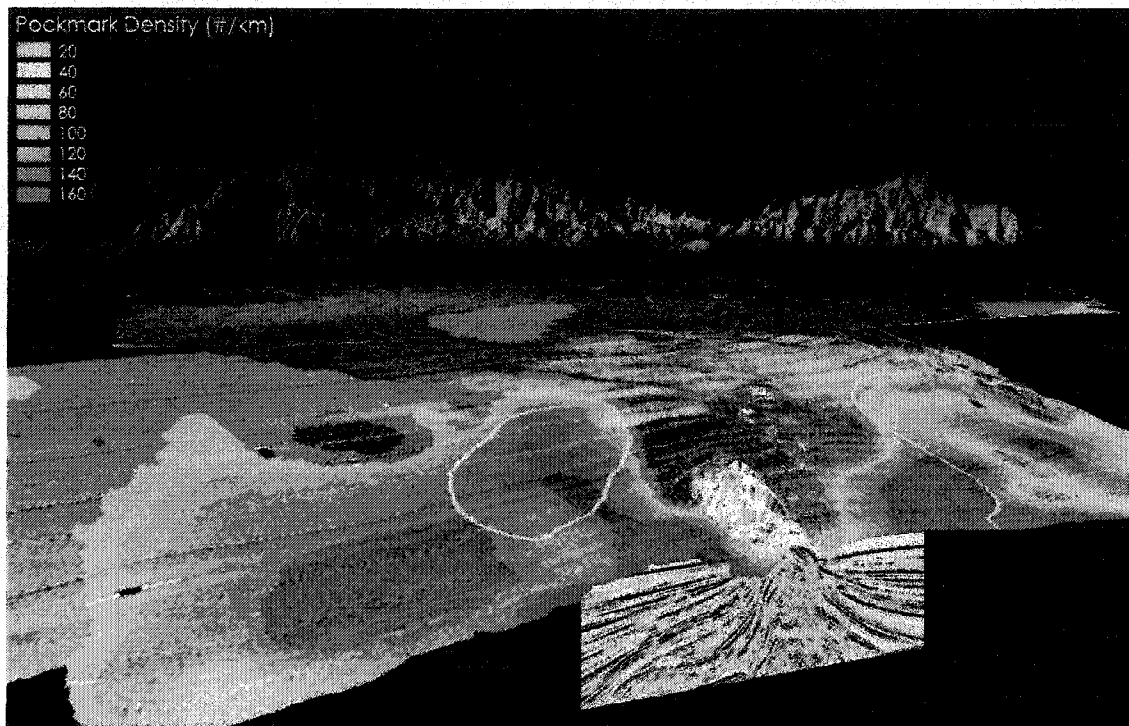
Figure 3.11 – Density of pockmarks determined from deep-towed sidescan sonar (Yun et al., 1999), with areas of landslide (yellow polygons).

The high concentration of pockmarks is normally associated to widespread of authigenic carbonates that precipitate on the seafloor. Authigenic carbonates associated with the pockmarks were reported during remotely operated vehicle (ROV) dives in the area (Orange, 1999). These carbonate deposits increase the seafloor roughness with possible augmentation of the backscatter response. However, results of core analysis at this water depth reported very fine grain sediments (0.004mm). The backscatter response of these fine-grain muddy sediments is predominantly controlled by volume scatter, being less

108

susceptible to changes in seafloor roughness. Therefore, roughness can account for only a small part of the backscatter anomaly.

The positive backscatter anomaly associated to the high concentration of pockmarks in water depths beyond 400m suggests the presence of active seeping gas in this part of the survey area. The gas probably comes from the dissociation of hydrates, which were indicated in these areas by the presence of bottom-simulating reflections in high-resolution seismic lines (Yun, 1999).

A very small amount of free gas in the sediment can explain the positive anomaly in deep-water. The backscatter angular response for the muddy sediments of this area can be calculated using sediment properties measured at the core sites. The parameters used as input for the model are: grain size 0.004mm, density 1994 kg/m^3 and sound speed 1526m/s. The model was then run a second time, including a gas fraction of 0.005 and the depth (450m). The result is shown in Fig. 3.12 for the total backscatter strength with and without gas. Note that the model predicts a positive backscatter anomaly of as much as 7dB due to the presence of gas.
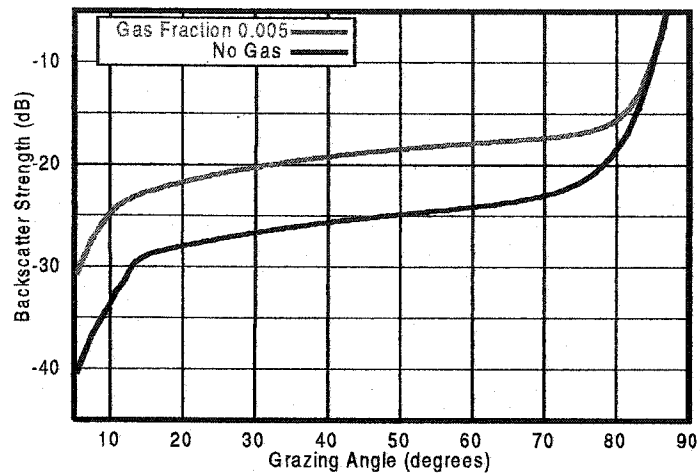
Figure 3.12 - Model response at 95kHz using the sediment properties measured at the deep-water backscatter anomaly.
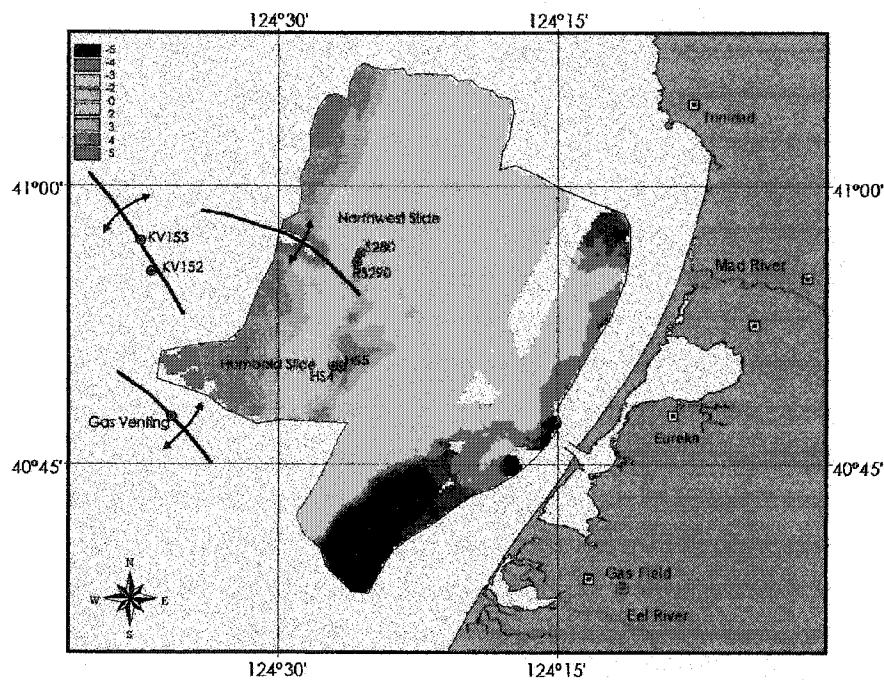
Figure 3.13 – Backscatter Anomaly with location of anticlines, gas seepages and slide areas.

110
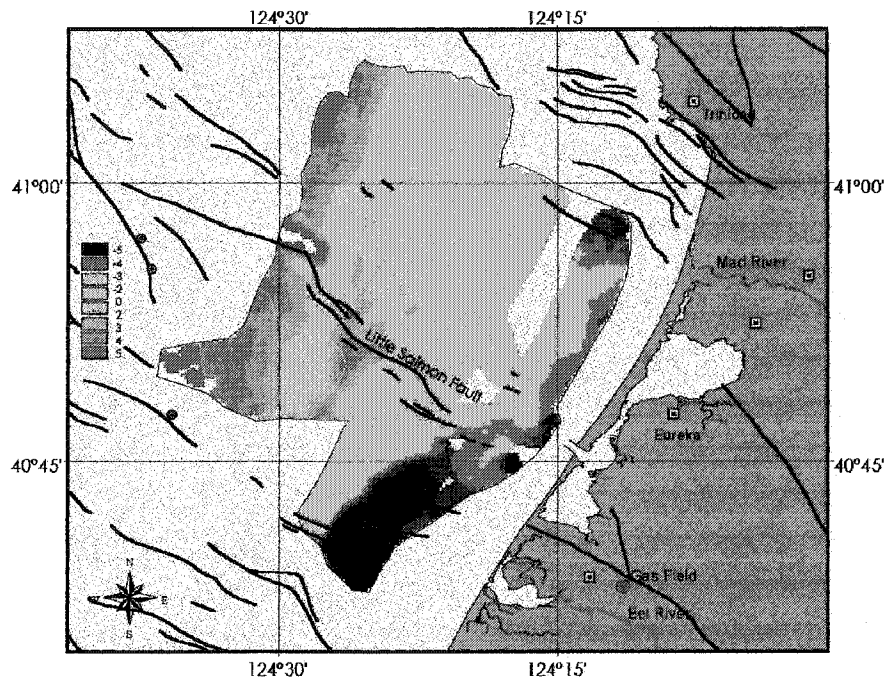
Figure 3.14 – Backscatter anomaly with distribution of faults.

3.6.3 Positive anomalies at the headscarp of Humbold and Northwest Slides

At the headscarp of Humbold and Northwest slides (Fig. 3.8), there are strong positive backscatter anomalies that can be related to subsurface gas accumulation. Results of core analysis at the head of the slides reveal high concentration of free gas in the sediment structure. Cores HS4, HS5, S280 and RS290 present a fraction of free gas greater than 0.07 (Fig. 3.13).

A gas fraction of 0.07 can explain the high backscatter anomaly at the headscarp of the slides. The backscatter angular response for sediments of this area is calculated using average sediment properties of

111

the 4 core sites. The parameters used as input for the model are: grain size 0.0093mm, density 1795 kg/m^3 and sound speed 1560m/s. The model was then run a second time, including a gas fraction of 0.07 and the depth (300m). The result is shown in Fig. 3.15 for the total backscatter strength with and without gas. Note that the model predicts a positive backscatter anomaly due to the presence of gas.
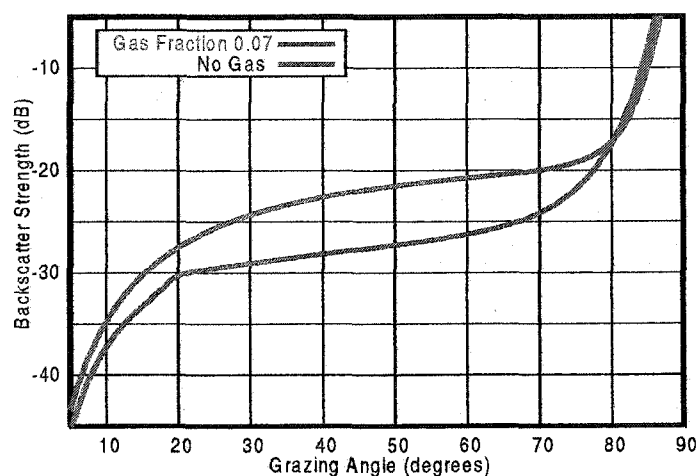
Figure 3.15 - Model response at 95kHz using average sediment properties measured at the headscarp of the slides.

There is evidence that the near-surface gas on the headscarps of Humbold and Northwest slides may come from deep reservoir sources. Multichannel seismic reflection profiles (16-40Hz) were collected in the study area in 1987. The distribution of subsurface gas was inferred in these seismic profiles based upon the presence of bright spots (abundant gas), and wipeout zones, which are acoustically impenetrable areas (Yun, 2000). The resulting echo character map based on this interpretation is

112

shown in Fig. 3.16. Note that the positive backscatter anomalies of the headscarp of Humbold and Northwest slides are inside a gas wipeout zone inferred from the seismic profiles (Fig. 3.13 and Fig. 3.16).

More evidence for the subsurface source of seeping gas in the area of the slide headscarps is the proximity of an anticline with a noticeable seafloor expression. Figure 3.13 shows the location of two gravity core samples KV152 and KV153 that were collected near the crest of an anticline. The result of isotopic analysis of hydrocarbon from these cores revealed the presence of thermogenic gas in the sediment (Kvenvolden and Field, 1981). These hydrocarbon seepages originated from a deep stratigraphic layer in the basin and migrated to the surface through permeable pathways. Figure 3.13 also shows the location of a gas-venting site that was reported during a ROV dive next to another anticline (Orange, 1999).

A seismic profile crossing the anticline adjacent to the Little Salmon Fault is shown in Fig. 3.11. The presence of enhanced reflectors next to the crest of the anticline is probably related to the presence of gas (Yun, 1999). The proximity of the Little Salmon Fault can facilitate the gas migration from the reservoir to the crest of the anticline. In fact, the extension of this fault zone inland crosses a productive gas field (Fig. 3.14). Gas probably accumulates at the impermeable crest of this anticline until it seeps to the surface through fractures at the base of the

113

folded structure. This seeping gas can explain the positive backscatter anomalies around the folded structure (Fig. 3.13).
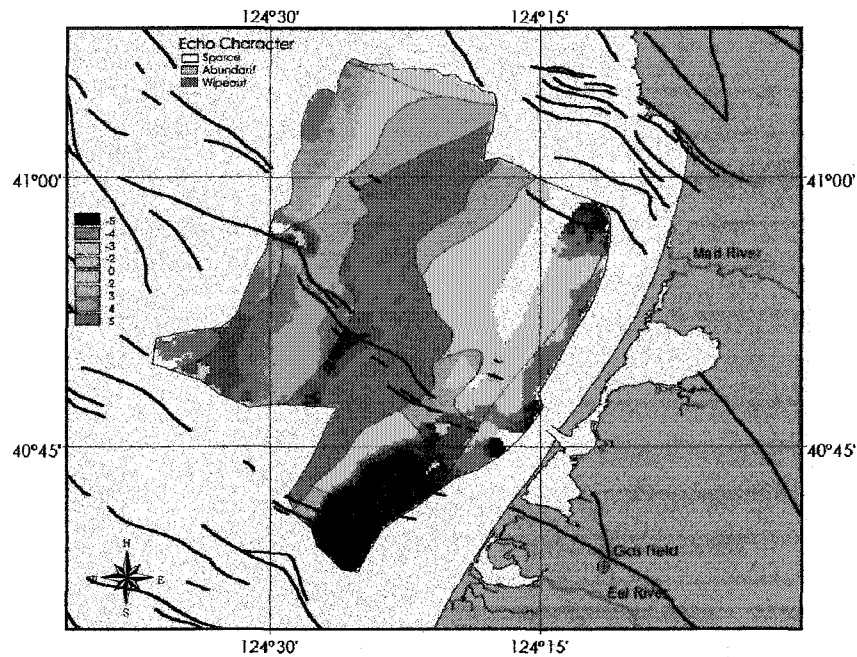
Figure 3.16 – Backscatter anomaly with seismic Echo Character and faults.

3.7 Conclusions

Acoustic remote sensing methods can be used successfully to locate accumulations of near-surface gas. With the aid of an acoustical backscattering model for gassy sediments, backscatter anomalies measured by multibeam sonars can be related to near-surface gas accumulation. If gas is present in the sediment, depth will be highly correlated to backscatter anomalies. In a general case, gas in shallow water reduces the backscatter, while gas in deep water yields high

114

positive anomalies. The presence of near-surface gas, when analysed in conjunction with other geological data, can be related to possible existence of subsurface hydrocarbon reservoir. New visualization techniques, which take advantage of 3D tools and GIS integration, are an essential tool to make the connection between multiparameter surface and sub-surface data. The detection of near-surface gas accumulations by means of acoustic remote sensing techniques can provide a fast and inexpensive evaluation of the hydrocarbon potential of offshore areas, reducing considerably the exploration risk. These techniques can also be used to assess a potential hazard for offshore engineering facilities, by means of mapping areas of potentially unstable seabed.

APPENDIX

JACKSON'S MODEL FOR ANGULAR BACKSCATTER

The parameter modeled by Jackson et al. (1986) is the total backscattering cross-section $\sigma_t(\theta)$ per unit solid angle, per unit area. This dimensionless quantity is given by the expression:

$$\sigma_t(\theta) = r^2 10^{0.2\alpha_w r} \frac{I_s}{I_0 A} \ ,$$ (1)

Where:

θ - Grazing angle

r - Slant range

α_w - Attenuation coefficient of the water in dB/m

I_s - Backscattered intensity at the receiver

I_0 - Incident intensity

A - Ensonified area.
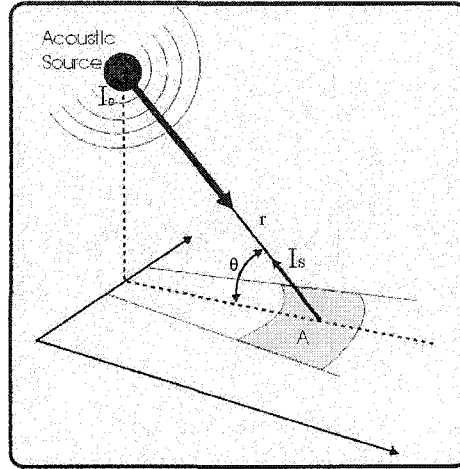
Figure A.1 - Backscatter cross section geometry.

The total backscatter cross-section σ$_t$ is modeled as a sum of two different processes: interface scattering and volume scattering (Fig. A.2). For that, the seafloor is considered inhomogeneous semi-infinite propagation media delimited by a rough surface. The interface scattering occurs at the water-sediment interface, where the seafloor acts as a reflector and scatterer of the incident acoustic energy. A portion of the incident acoustic energy will be transmitted into the seafloor. This transmitted energy will be scattered by heterogeneities in the sediment structure, which are the source of the volume scatter.

$$\sigma_t(\theta) = \sigma_r(\theta) + \sigma_v(\theta),$$ (2)

Where:

$\sigma_r(\theta)$ - interface backscattering cross section.

$\sigma_v(\theta)$ - the volume backscattering cross section.

117
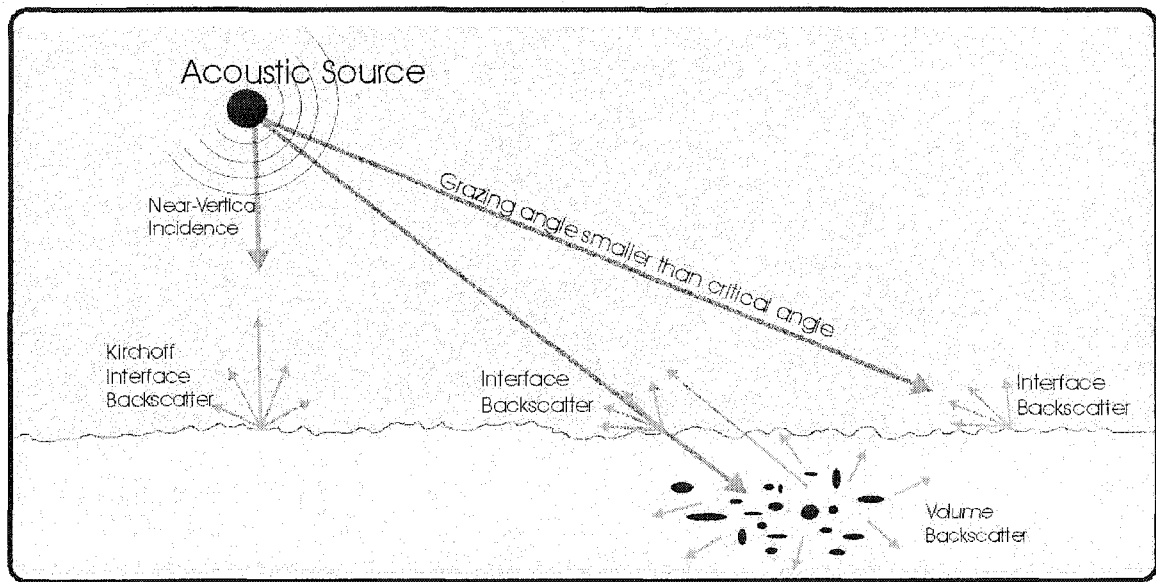
Figure A.2 – Two different contributions: Volume and interface scattering.

Composite Roughness Model

The composite roughness model developed by Jackson et al. (1986) estimates the interface backscattering cross section (σ_r) for a particular seafloor type as a function of frequency and grazing angle. This model defines the seafloor type based on five parameters that reflect sediment physical properties and seafloor roughness (Eq. (1)): a) two parameters for impedance, sound velocity ratio (v) and density ratio (ρ); b) one parameter for attenuation: loss tangent (δ), and; c) two parameters for roughness, the spectral strength (ω_2) and the spectral exponent of bottom relief (λ). The acoustic frequency (f) and the grazing angle (θ) of the wave front with the seafloor are treated as given parameters.

118

$$\sigma_r(\theta, f) = F(\theta, f; \quad \rho, v, \delta, \omega_2, \lambda)$$

(3)

σ_r - Interface backscattering cross-section per unit solid angle per unit area.

θ - Grazing angle.

f - Frequency.

ρ - Ratio of sediment mass density to water mass density.

v - Ratio of sediment sound speed to water sound speed.

δ - Loss parameter

ω_2 - Spectral strength at wavenumber 1 rad/m

λ - Spectral exponent

The loss tangent parameter is defined as the ratio of the imaginary wavenumber to the real wavenumber for the sediment. It is related to the attenuation coefficient, the frequency and the sound-speed in the sediment.

$$\delta = \left(\frac{\alpha}{f}\right) \frac{vc_w \ln(10)}{40\pi}$$

(4)

Where,

119

α - Attenuation coefficient in dB/m

c_w - Sound speed in water.

f - Acoustic frequency

A two-dimensional power spectral density function (Fig. A.3) is the used to describe the roughness distribution at the water-sediment interface:

$$W(k) = w_2 k^{-\lambda} \tag{5}$$
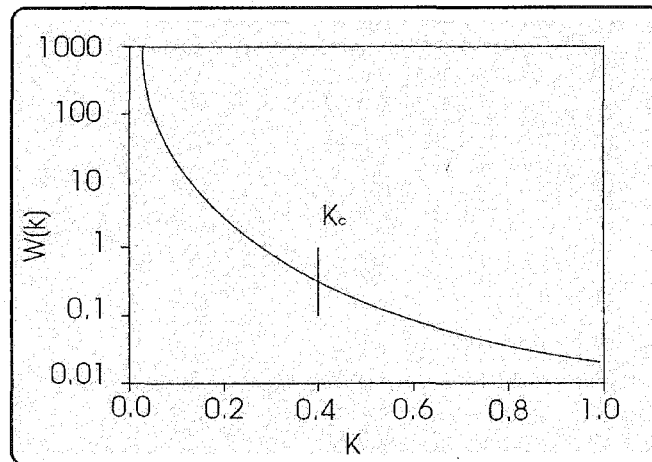
Where,

k = wave number.

Figure A.3 - Typical two-dimensional power spectral density function

In this formulation, the bottom roughness is assumed to be isotropic and described by a random variable *h(r)*. The difference *h(r+r₀)-*

120

h(r) is considered a stationary random process that is related to the power spectral *W(k)* by the structural function D(r):

$$D(r) = E\left\{ \left[h(r + r_o) - h(r) \right]^2 \right\} = C_h^2 r^{2\alpha} \tag{6}$$

Where,

$$\alpha = (\lambda/2) - 1$$

$$C_h^2 = \frac{2\pi w_2 \Gamma(2 - \alpha) 2^{-2\alpha}}{\alpha(1 - \alpha)\Gamma(1 + \alpha)}$$

The fundamental assumption of the composite roughness model is that the backscatter cross section can be calculate based on the small-scale roughness with local grazing angle dependent on the large scale slope (Fig. A.4). The boundary between large-scale and small-scale roughness is delimited by the acoustic wavelength. The backscatter cross-section σ_{rr} from a small patch of the seafloor is modeled based on the Rayleigh-Rice theory for small perturbations (Kuo, 1964). The modification proposed by Mourad and Jackson (1990) takes into account the acoustic attenuation in the sediment, including the effects of the critical angle.

$$\sigma_{rr}(\theta) = 4k^4 \sin^4(\theta) |Y(\theta)|^2 W(K_\theta) \tag{7}$$

Where,

k – Acoustic wavenumber

$$Y(\theta) = \frac{(\rho - 1)^2 \cos^2(\theta) + \rho^2 - \kappa^2}{[\rho \sin(\theta) + P(\theta)]^2}$$

$$P(\theta) = \sqrt{\kappa^2 - \cos^2(\theta)}$$

$$\kappa = \frac{1}{\nu}(1 + i\delta))$$

$$K_\theta = \left[4k^2 \cos^2(\theta) + \left(\frac{k}{10}\right)^2 \right]^{\frac{1}{2}}$$
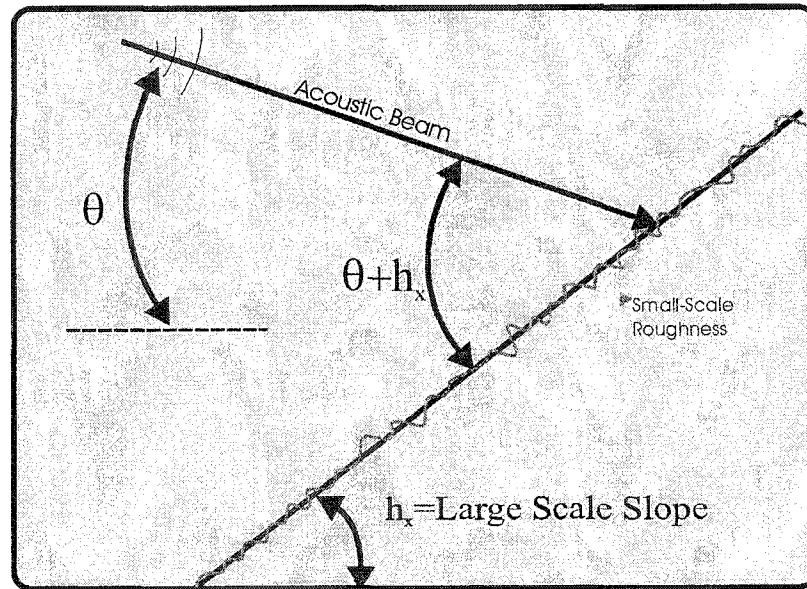
Figure A.4 – Local grazing Angle corrected for large-scale roughness slope.

122

The composite backscatter solution for small grazing angles is obtained by averaging the small roughness perturbations over the bottom slope:

$$\sigma_{cr}(\theta) = \frac{S(\theta,s)}{\pi^{\frac{1}{2}}s} \int_{-\theta}^{\infty} \sigma_{rr}(\theta + h_x) \exp\left(-\frac{h_x^2}{s^2}\right) dh_x \qquad (8)$$

where,

$S(\theta,s)$ - Shadowing function.

s - rms slope of the large-scale surface

h_x - local large-scale slope

The function $S(\theta,s)$ accounts for the shadowing of the large-scale surface.

$$S(\theta,s) = \frac{1 - e^{-2Q}}{2Q} \qquad (9)$$

Where,

$$Q = \frac{\pi^{-\frac{1}{2}} e^{-t^2} - t\left[1 - erf(t)\right]}{4t}$$

$$t = \frac{\tan(\theta)}{s}$$

The rms slope of the large-scale surface *(s)* can be derived from the structure function *D(r)*:

$$s^2 = \frac{(2\pi w_2)^{\frac{1}{2}}}{2(1-\alpha)} \left(\frac{k^2}{\alpha} \right)^{\frac{1-\alpha}{\alpha}}$$

(10)

Kirchhoff Solution for Large Grazing Angle

For large grazing angle, Jackson replaces the Composite Roughness model by the Kirchhoff approximation. The Kirchhoff solution is a function of the roughness and impedance contrasts at the water-sediment.

$$\sigma_{kr}(\theta) = \frac{|R(90^o)|^2}{8\pi \sin^2(\theta)\cos^2(\theta)} \int_0^\infty \exp(-qu^{2\alpha}) J_0(u) u \, du$$

(11)

where,

J₀(u) - Bessel function of the first kind and zero order

$$q = \sin^2(\theta)\cos^{-2\alpha}(\theta) C_h^2 2^{1-2\alpha} K^{2(1-\alpha)}$$

$$R(\theta) = \frac{\rho \sin(\theta) - P(\theta)}{\rho \sin(\theta) + P(\theta)}$$

Γ(α) - Gamma function

124

The expression for σ$_r$ is calculated as an interpolation between the Kirchhoff approximation and the composite roughness solution.

$$\sigma_r(\theta) = f(x)\sigma_{cr}(\theta) + [1 - f(x)]\sigma_{kr}(\theta) \qquad (12)$$

Where,

$\sigma_{cr}(\theta)$ - Composite backscattering cross-section

$\sigma_{kr}(\theta)$ - Kirchhoff backscattering cross-section

$f(x) = (1 + e^x)^{-1}$ - Interpolation function

$x = 80(\cos(\theta) - \cos(\theta_{15db}))$

θ_{15db} = Angle at which the Kirchoff backscatter is 15db bellow its maximum.

Volume Backscatter

In his approach for determining volume backscatter, Jackson considers the sediment a statistically inhomogeneous semi-infinite propagation media delimited by a rough surface. With this simplification he defines a volume backscattering cross section equivalent to the interface, using a similar solution to the one proposed by Stockhausen (1963). The total volume contribution is dependent on a free parameter

125

σ_2, which is calculated based on the ratio of the sediment volume scattering cross section to sediment attenuation coefficient.

$$\sigma_{pv}(\theta) = \frac{5\delta\sigma_2 c\left[1 - R^2(\theta)\right]^2 \sin^2(\theta)}{\nu \ln(10)|P(\theta)|^2 \text{Im}|P(\theta)|}$$

(13)

In analogy to what was done with the interface backscatter, the volume backscatter cross-section is averaged over the bottom slope:

$$\sigma_v(\theta) = \frac{S(\theta,s)}{\pi^{\frac{1}{2}}s} \int_{-\theta}^{\infty} \sigma_{pv}(\theta + h_x)\exp\left(-\frac{h_x^2}{s^2}\right)dh_x$$

(14)

126

BIBLIOGRAPHY

Anderson, A., Abegg F., Hawkins, J. A., Duncan, M. E., Lyons, A. P. (**1998**), "Bubble populations and acoustic interaction with the gassy floor of Echernförde Bay," Continental Shelf Research **18**, 1807-1838.

Anderson, A., and Hampton, L. D. (**1980a**), "Acoustics of gas-bearing sediments I. Background," The Journal of the Acoustical Society of America **67 (6)**, 1865-1889.

Anderson, A., and Hampton, L. D. (**1980b**), "Acoustics of gas-bearing sediments II. Measurements and models," The Journal of the Acoustical Society of America **67 (6)**, 1890-1903.

Anonymous (**2000**), "Kongsberg Simrad Operator Manual: EM Series Datagram Formats".

Anonymous (**1994**), "High-Frequency Ocean Environmental Acoustic Models Handbook," Applied Physics Laboratory Technical Report APL-UW TR **9407**, University of Washington, Seattle, WA, Chapter 4.

Aranof S. (**1991**), "Geographic Information Systems: A Management Perspective," WDL Publication, Ottawa, Canada.

Berry, J. L and Prost, G. L. (1999), "Hydrocarbon exploration," In: Rencs, A., Remote Sensing for the earth sciences: Manual of Remote Sensing, edited by Andrew Rencz, pp 449-508, John Wiley & Sons, Inc., Toronto.

Bonham-Carter, G. F. (1996), "Geographic Information Systems for Geoscientists: Modelling with GIS," Series Computer Methods in the Geosciences Vol. 13, Pegamon Publishers, Ontario, Canada.

Borgeld, J.C., J.E. Hughes Clarke, J.A. Goff, L.A. Mayer, and J.A. Curtis, (1999), "Acoustic backscatter of the 1995 flood deposit on the Eel shelf, Marine Geology, 194, 183-196.

Boyle, F. A. and Chotiros, N. P. (1995), "A model for high-frequency acoustic backscatter from gas bubbles in sandy sediments at shallow grazing angles," The Journal of the Acoustical Society of America 98 (1), 531-541.

Burrough P. A. and MacDonnell, R. A. (1998), "Principles of Geographical Information Systems: Spatial Information Systems and Geostatistics," Oxford University Press, New York.

Carver, G.A. (1987), "Late Cenozoic tectonics of the Eel River basin region, coastal northern California". In: H. Schymiczek and R. Suchsland (Eds.), Tectonics, sedimentation, and evolution of the Eel River basin and other coastal basins of Northern California, San Joaquin Geological Society Misc. Publication, 37, 61-72.

Chavez, P. S., Gardner, J. V., (**1994**), "Extraction of spatial information from remotely sensed image data – An example: Gloria sidescan sonar images," Canadian Journal of Remote Sensing, **20** (**4**), 443-453.

Clarke, S. H. Jr. (**1987**), "Geology of the California continental margin north of Cape Mendocino." In: Scholl, D. W., Grantz, A., and Veddr, J. G. (Eds.). Geology and resource potential of the continental margin of western North America and adjacent ocean basins – Beaufort Sea to Baja California, Circum-Pacific Council for Energy and Mineral Resources Earth Science Series 6, 337-351.

Davis E. E., Currie, R. G., Sawyer, B. S. and Kosalos, J. G. (**1986**), "The use of swath bathymetry and acoustic image mapping tools in marine geosciences". Marine Technology Society, **20** (**4**), 17- 27.

de Moustier C., (**1988**), "State of the Art in Swat Bathymetry Survey Systems," International Hydrographic Review, **LXV** (**2**), 25-54.

de Moustier, C. and Alexandrou, D. (**1991**), "Angular dependence of 12kHz Seafloor Acoustic Backscatter," The Journal of the Acoustical Society of America **90** (**1**), 522-531.

Djikstra, S. J. (**1990**). "Software tools developed for seafloor classification". PhD thesis, University of New Brunswick, NB, Canada.

ESRI Library (**1998**), "ESRI Shapefile Technical Description, an ESRI White paper," www.esri.com/library/whitepapers/pdfs/shapefile.pdf, July 1998.

Evans, R. L., Law, L. K., St-Louis, B., Cheesman, S., Sananikone, K. (**1999**), "The shallow porosity structure of the Eel shelf, northern California: results of a towed electromagnetic survey," Marine Geology **154**, 211-226.

Farmer, D. M. and Vagle, S. (**1989**), "Waveguide propagation of ambient sound in the ocean-surface bubble layer," The Journal of the Acoustical Society of America **86**, 1897-1908.

Field, M.S., and K.A. Kvenvolden, (**1985**), "Gas hydrates on the northern California continental margin," Geology, **13**, 517-520.

Field, M.S., and K.A. Kvenvolden, (**1987**), "Preliminary report on gaseous hydrocarbons in sediments and seeps offshore Eel River basin, Califormia, In: Schymiczek, H., R. Suchsland, (Eds.)., Tectonics, Sedimentation and Evolution of the Eel River Basin and Other Coastal Basins of Northern California," San Joaquin Geol. Soc. Misc. Publ., **37**, 55 – 60.

Field, M, S., Clarke H., and White, M. E. (**1980**), "Geology and geologic hazards of offshore Eel River Basin, Northern California Continental Margin," USGS Open-file report 80-1080.

Fonseca, L and Mayer, L. (2001), "The high-frequency backscattering angular response of gassy sediments: Model/data comparison from the Eel River Margin, California," The Journal of the Acoustical Society of America, Accepted for publication 2001.

Gardner, J. V., Prior, D. B. and Field, M. E. (**1999**), "Humbold Slide – a large shear-dominated retrogressive slope failure," Marine Geology **154**, 323-338.

Goff, J. A., Orange, D. L., Mayer, L. A. and Clarke, J. H. (**1999**), "Detailed investigation of continental shelf morphology using a high-resolution swath sonar survey: the Eel margin, northern California", Marine Geology **154**, 255-269.

Groome, M., Gutmacher, C. E. and Stevenson, A. J. (1997), "Atlas of GLORIA Sidescan-Sonar Imagery of the Exclusive Economic Zone of the United States: EEZ-View," USGS CD-ROM Open-File Report, 97-540.

Hovland, M. and Judd A. G. (**1989**). "Seabed pockmarks and seepages: Impact on geology, biology and the marine environment," Graham & Trotman, Norwell, MA.

Hughes-Clarke, J., Danforth, B. W. and Valentine, P. (1997), "Areal seabed classification using backscatter angular response at 95kHz," SACLANTCEN Conference Proceeding CP-45, Italy,

Ivakin, A. N. (**1998**), "A unified approach to volume and roughness scattering," The Journal of the Acoustical Society of America **103 (2)**, 827-837.

Jackson, D. R. and Briggs, K. B. (**1992**), "High-frequency bottom backscattering: Roughness versus sediment volume scattering," The Journal of the Acoustical Society of America **92 (2)**, 962-977.

Jackson, D. R. and Ivakin A. N. (**1998**), "Scattering from elastic sea beds: First-order theory," The Journal of the Acoustical Society of America **103**, 336-345.

Jackson, D. R., Winebrenner, D. P. and Ishimaru, A. (**1986**), "Application of the composite roughness model to high-frequency bottom backscattering," The Journal of the Acoustical Society of America **79 (5)**, 1410-1422.

Joseph, K. and Desa, E. (**1997**). "Acoustic Remote Sensing of Ocean Flows," In: Singal, S. (Ed.), Acoustic Remote Sensing Applications, Springer-Verlag, New York, 409-448.

Kleiner, A., Gee, L. and Anderson, B. (**2000**), "Synergistic Combination of Technologies," Sea Technology, June 2000.

Kolouch, D. (**1984**), "Interferometric side-scan sonar: A topographic sea-floor mapping system," International Hydrographic Review, **LXI** (**2**), 35-49.

Kulm, L. D. and Suess, E. (**1990**), "Relationship of carbonate deposits and fluid venting: Oregon accretionary prism," Journal of Geophysical Research **95**, 8899-8916.

Kuo, E. Y. (**1964**). "Wave scattering and transmission at irregular surfaces," The Journal of the Acoustical Society of America **36**,. 2135-2142.

Kvenvolden, K.A., and G.D. Redden, (**1980**), "Hydrocarbon gas in sediment from the shelf, slope and basin of the Bering Sea," Geochimica et Cosmochimica Acta, **44**, 1145-1150.

Kvenvolden, K., and Field, M. (**1981**). "Thermogenic Hydrocarbons in unconsolidated sediment of Eel River Basin, Offshore Northern California," AAPG Bull. **65**, 1642-1646.

Laughton, A. S. (**1981**). "The first decade of GLORIA." Journal of Geophysical Research, **85** (**12**), 511-534.

Link, W. K. (**1952**), "Significance of oil and gas seeps in world oil exploration," AAPG Bulletin **36**, 1506-1514.

Lyons, A. P., Duncan, M. E., Anderson, A. L. and Hawkins, J. A. (**1996**). "Predictions of the acoustic scattering response of free-methane bubbles in muddy sediments." The Journal of the Acoustical Society of America **99 (1)**, 163-172.

MacCullagh, J. M. (**1995**), "Power to the People! PC &Workstations Mapping and Database Systems. In: Van Driel, J. N. and J.C. Davis, Digital Geologic and Geographic Information Systems. American Geophysical Union, Washington, USA.

Martínez, J. V. (**1991**), "Analysis of Multibeam Sonar Data for the Characterization of Seafloor Habitats," Master Thesis. University of New Brunswick, Department of Geodesy and Geomatics Engineering.

Mayer, L. A., Paton, M., Gee, L., Gardner, J. V. and Ware, C. (**2000**), "Interactive 3-D Visualization: A Tool for Seafloor Navigation, Exploration and Engineering". TBP.

Mayer, L., Fonseca, L., Pacheco, M., Galway, S., Martinez, J. V. and Hou, T. (**1999**), "The STRATAFORM GIS CD," U.S. Office of Naval Research distribution.

Mayer, L., Dijkstra, S., Clarke, J. H., Paton, M. and Ware, C. (**1997**), "Interactive tools for the Exploration and Analysis of Multibeam and other Seafloor Acoustic Data,". SACLANTCEN Conference Proceeding CP-45, Italy, 355-362.

Mello, M. R., Babinski, N. A., Gonçalvels F. T., and Miranda. F. P. (**1996**) "Hydrocarbon Prospecting in Amazon Rain Forest: Application of surface geochemical, microbiological, and remote sensing methods". In: Schumacher and Abrams (Eds.), Hydrocarbon Migration and its near-surface expression, AAPG Memoir **66**, 401-411.

Miranda, F. P., Fonseca, L., Carr, J., Taranik, J. (**1996**). "Analysis of JERS-1 (Fuyo-1) SAR data for vegetation discrimination in northwestern Brazil using the semivariogram textural classifier (STC)." International Journal of Remote Sensing, **17**, 3523-3529.

Mourad, P. D., and Jackson, D. R. (**1989**), "High frequency sonar equation models for bottom backscatter and forward loss," Proceedings of OCEANS'89 (IEEE, New York), 1168-1175.

Nittrouer, C. A. (**1999**), "STRATAFORM: Overview of its design and synthesis of its results." Marine Geology **154**, 3-12.

Nittrouer, C. A. and Kravitz, J. H. (**1996**), "STRATAFORM: A program to study the creation and interpretation of sedimentary strata on continental margins," Oceanography, **9** (**3**), 146 – 152.

Novarini, J. C. and Caruthers, J. W. (**1998**), "A simplified approach to backscattering from a rough seafloor with sediment inhomogeneities," The Journal of Oceanic Engineering **23** (**3**), 157-166.

Oliveira, W. J. and A. P. Crósta (1996), "Detection of hydrocarbon seepage in the São Francisco Basin, Brazil, though Landsat TM, soil geochemistry and airborne field spectrometry data integration," Proceedings of the 11th thematic conference on geologic remote sensing, 155-165. Las Vegas, NV.

Orange, D. L., Angell, M.M. and Lapp, D. (1999), "Using seafloor mapping (bathymetry and backscatter) and high-resolution sub-bottom for both exploration and production: detecting seeps, mapping geohazards, and managing data overload with GIS", Proceedings 30th OTC, Houston, Texas.

Orange, D. L. (1999), "Tectonics, sedimentation, and erosion in northern California: submarine geomorphology and sediment preservation potential as a result of three competing process", Marine Geology 154, 368-382.

Paton, M. A, Mayer, L. A., Ware, C. (1997), "Interactive 3-D Tools for Pipeline Route Planning," Proceedings of the IEEE- Oceans 97 2,1261-1222.

Paton, M. A. (1995), "An Object Oriented Framework for Interactive 3-D Scientific Visualization," Master Thesis, University of New Brunswick, NB, Canada.

Parker, J.D., (**1987**), "Geology of the Tompkins Hill gas field, Humboldt County, California, In: Schymiczek, H., R. Suchsland, (Eds.)., Tectonics, Sedimentation and Evolution of the Eel River Basin and Other Coastal Basins of Northern California," San Joaquin Geol. Soc. Misc. Publ., **37**, 83-88.

Pettigrew, T.,L., (**1992**), "The design and operation of a wireline pressure core sampler (PCS)." ODP Tech.Note, **17**

Rice, G. K. (**1985**), "Near-surface hydrocarbon gas measurement of vertical migration," In: Davidson, M. J., "Unconventional Methods in Exploration for Petroleum and Natural Gas, IV: A Symposium", Southern Methodist University Press, 183-189.

Richardson, M. D. and Davis, A. M. (**1998**), "Modeling methane-rich sediments of Eckernförde Bay," Continental Shelf Research **18 (14-15)**, 1671-1688.

Ryan, W. B. F. (**1986**), "Side-Looking Sonar Backscatter response at dual frequencies." Marine Geophysical Researches.

Silberman, E. (**1957**), "Sound velocity and attenuation in bubbly mixtures measured in standing wave tubes". Journal of acoustical society of America **29**, 925-953.

Stockhausen, J. H. (**1963**), "Scattering from the Volume of an Inhomogeneous Half-Space," Naval Research Establishment, Canada, Report **63/9**.

Summerfield, C.K and C.A. Nittrouer, (**1999**), "Modern accumulation rates and a sediment budget for the Eel shelf: a flood dominated depositional environment", Marine Geology **154**, 227-242.

Wilkens, R.H, and M.D. Richardson, (**1998**), "The influence of gas bubbles on sediment acoustic properties: *in situ*, laboratory, and theoretical results from Eckernforde Bay, Baltic Sea," Cont. Shelf Research, **18**, 1859-1892.

Tyce, R. C. (**1986**), "Deep Seafloor Mapping Systems – A Review". MTS Journal, **20**, 4-16.

Van Driel, J. N. (**1995**), "Three-Dimensional Display of Geological Data," In: Van Van Driel, J. N. and Davis, J. C. (Eds), Digital Geologic and Geographic Information Systems. American Geophysical Union, Washington, USA.

Ware, Colin (**1999**), "Information Visualization: Perception for Design", Morgan kaufmann Publisher, New York, USA.

Warmerdam, F. and collaborators (**2000**), "Arc/Info Binary Grid Format," http://gdal.velocet.ca/projects/aigrid/aigrid_format.html

Yun, W. J. (**2000**), "Fuild flow and deformation at an active continental margin – The Eel River Basin, CA", PhD Thesis in Earth Sciences, University of California Santa Cruz.

Yun, W. J., Orange, D. L., Field, M. E. (**1999**), "Subsurface Gas Offshore Northern California and its Link to Submarine Geomorphology", Marine Geology **154**, 357-368.